Chapter 6
Aerodynamics of Non-lifting Bodies

Abstract This chapter presents the sources of drag that are encountered by a nonlifting body that is moving at transonic Mach numbers. In inviscid conditions drag can be produced if the integrated pressure over a body has a component in the opposite direction to the flow (pressure drag). First, the reader is introduced to the relation between the geometry of a body and the pressure distribution over the body. Subsequently, a method for the calculation of the pressure drag over axisymmetric bodies is presented based on the linear potential flow equation. It is shown how the pressure drag is a function of the cross-sectional area distribution of the body. The concept of *area ruling* is presented and examples are shown of practical implementations of the area rule. If the flow is assumed viscous, other drag sources arise: friction drag and drag due to boundary-layer separation. A qualitative characterization of laminar and turbulent boundary layers is presented along with the concepts of transition and separation. Also, the interaction between shock and boundary layer (both weak and strong) is further detailed and it is shown how this influences drag divergence in transonic conditions. In addition, calculation methods are presented to estimate the boundary-layer properties of laminar and turbulent boundary layers along with their transition region for bodies subjected to an external pressure and velocity distribution. This chapter contains 8 examples and concludes with 29 practice problems.

6.1 Introduction

There exist two types of drag: friction drag and pressure drag. Friction drag is mostly caused by the boundary layer between the body and the outer flow and is a function of the viscosity of the fluid. A nonlifting body in transonic flow can experience pressure drag through two mechanisms. One is due to a wake that is formed when the flow streamlines separate from the body surface (drag due to flow stagnation and separated flow). The second cause is through the formation of shock waves (wave drag). Wave drag is an aerodynamic phenomenon which is unique to supersonic flow. This type of drag is associated with the energy which is radiated away from the vehicle in the form of pressure waves. In the present chapter we focus on these three causes for drag. The aim of the chapter is to explain to the reader how a nonlifting body produces drag and what parameters are of influence.

R. Vos and S. Farokhi, *Introduction to Transonic Aerodynamics*,
Fluid Mechanics and Its Applications 110, DOI 10.1007/978-94-017-9747-4_6

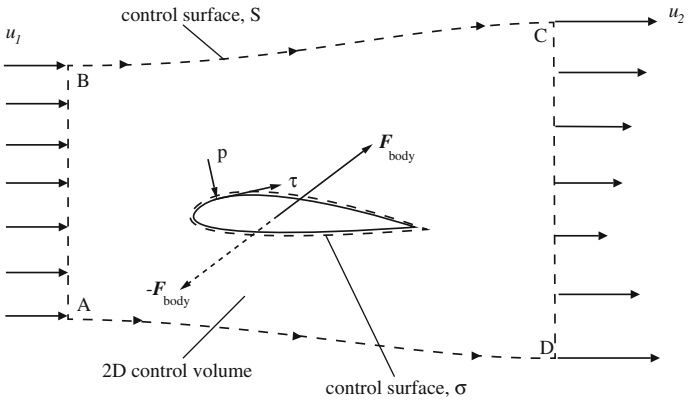

Fig. 6.1 Body force generated by pressure and shear stresses on the body and their relation to the velocity deficit in the wake

In Fig. 6.1 a body is shown in a control volume. It is assumed that the upper and lower boundary of the volume are formed by streamlines of the flow. The pressure and shear forces that act on the body result in a total body force, $\boldsymbol{F}_{\text{body}}$. By Newton's third law, the body exerts an equal and opposite force on the fluid, $-\boldsymbol{F}_{\text{body}}$. Let us investigate the effect of this body force on the momentum in the flow. We start from Newton's second law:

$$\boldsymbol{F} = \frac{\mathrm{d}}{\mathrm{d}t}(m\boldsymbol{V}) \tag{2.114}$$

Remember that the right-hand side (RHS) of (2.114) physically represents the time rate of change in momentum that is moving through the control volume. Its representation has been given in the LHS of (2.121):

$$\boldsymbol{F} = \frac{\partial}{\partial t}\iiint_{\mathscr{V}} \rho \boldsymbol{V}\,\mathrm{d}\mathscr{V} + \oiint_{S+\sigma} (\rho \boldsymbol{V}\cdot\mathbf{d}\boldsymbol{S})\boldsymbol{V} \tag{6.1}$$

The integral over the second control surface, σ is always zero (regardless of control volume shape) due to the fact that the inner product of velocity and surface area vanishes on the body surface. If we neglect the small body forces on the fluid ($\boldsymbol{f} = 0$), the external force $\boldsymbol{F}$ can be broken down into two parts: the reaction force from the body, $-\boldsymbol{F}_{\text{body}}$, and the force exerted across the outer boundary:

$$\boldsymbol{F} = -\iint_S p\mathbf{d}\boldsymbol{S} - \boldsymbol{F}_{\text{body}} \tag{6.2}$$

If we assume steady conditions ($\partial/\partial t = 0$) we can rewrite (6.1) according to:

$$F_{\text{body}} = -\iint_S (\rho \boldsymbol{V}\cdot\mathbf{d}\boldsymbol{S})\boldsymbol{V} - \iint_S p\mathbf{d}\boldsymbol{S} \tag{6.3}$$

In (6.3), the force exerted on the body is coupled to properties of the flow inside the control volume. We would like to determine the x-component of the body force from the parallel velocity components at the beginning of the control volume, u_1, and at the end of the control volume, u_2. We write the x-component of (6.3) as follows:

$$F_{\text{body}_x} = -\iint_S (\rho \boldsymbol{V} \cdot \mathbf{d}\boldsymbol{S})u - \iint_S p\mathbf{d}\boldsymbol{S}_x \tag{6.4}$$

First we notice that when the boundaries of the control volume are chosen at an infinite distance from the body the pressure, p, should be constant on this boundary. For a constant pressure, the integral yields:

$$\iint_S p\mathbf{d}\boldsymbol{S}_x = 0 \tag{6.5}$$

Since the upper and lower surface of the control volume are streamlines of the flow, the velocity vector and the control surface are locally aligned. This means that the inner produce $\boldsymbol{V} \cdot \mathbf{d}\boldsymbol{S} = 0$ along those boundaries. Therefore, we can write for F_{body_x}:

$$F_{\text{body}_x} = \int_A^B \rho_1 u_1^2 \mathrm{d}y - \int_D^C \rho_2 u_2^2 \mathrm{d}y \tag{6.6}$$

By employing the continuity equation in integral form (2.109) over the entrance and exit of this control volume and subsequent substitution yields the following expression:

$$F_{\text{body}_x} = \int_D^C \rho_2 u_2 (u_1 - u_2) \mathrm{d}y \tag{6.7}$$

This substitution is left as a homework problem (Problem 6.1).

The body force in x-direction is of course the drag force that a body experiences whenever exposed to a fluid. What is demonstrated by (6.7) is that the drag of a body is directly related to a momentum decrement in the wake of the flow. It shows that whenever a drag force is present, it is being accompanied by a momentum decrement in the wake. Vice versa, the measurement of the total momentum deficit in the wake is a direct measure for the amount of drag that a body experiences. It can be shown that the momentum deficit, in turn, is related to total pressure deficit in the wake (see Problem 6.2). In Fig. 6.2 the total pressure deficit is shown at an outboard wing section of a modern high-subsonic wing. Even though this experimental result does not pertain to a nonlifting body, it is still a useful example. It can clearly be seen how the shock wave and the boundary layer both contribute to the total pressure loss (drag) in the wake. Note that in this example the contribution of the wave drag is much less than the friction drag.

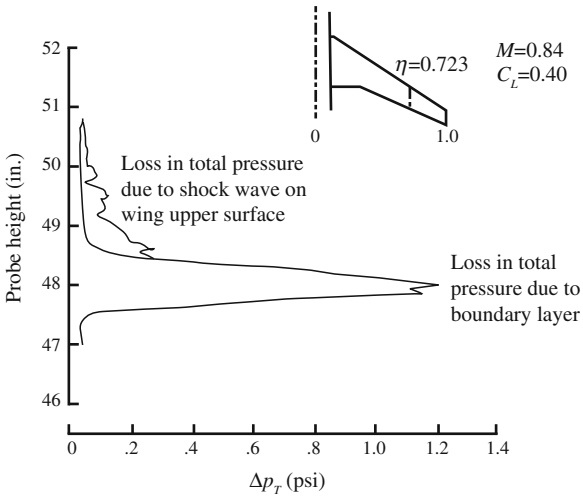

Fig. 6.2 Drag is related to the total pressure loss in the wake (after Ref. [14])

If we subdivide the outer geometry of a typical high-subsonic transport aircraft into different components, we can make a distinction between components that are primarily designed to produce aerodynamic forces, and components that are designed not to produce any aerodynamic forces. Examples of the latter are the fuselage (including cockpit and tail cone), the pylons, the engine nacelles, and the vertical tail in cruise conditions. The aerodynamic design of such components should be such that the overall drag is minimized. In transonic conditions, the production of wave drag on these components should be reduced to a minimum. A general design rule for these components is that local supervelocities should be minimized. Why supervelocities should be minimized is evident when this chapter is studied.

Even though this statement seems simple enough, in practice it is often not as easy to do this due to conflicting requirements on the geometry. Cockpit design, for example, must satisfy strict visibility constraints that ensure that the pilot has a good view on the runway when the aircraft is at high pitch angles before the landing. Window design should ensure that this constraint is satisfied, although this might lead to sharp corners and high curvatures that lead to high supervelocities and possible wave drag in high speed flight. We will present more examples where functional and aerodynamic requirements are conflicting. How do we design these nonlifting components on aircraft such that the wave drag that they produce in high-subsonic conditions is minimized?

The present chapter presents the relation between geometry and supervelocities, via the pressure coefficient, C_p. Subsequently, the pressure drag in supersonic conditions is treated with a focus on the sonic area rule. The foundations of boundary layer flow and friction drag is discussed in the Sect. 6.3 of this chapter. Typical transonic characteristics such as shock-boundary-layer interaction are introduced as well as the effect of Mach and Reynolds number on friction drag and transition. The chapter closes with a qualitative section on the relation between external shape of intersecting components and their interference drag.

6.2 Pressure Distribution Over Nonlifting Bodies

In this section we investigate the effect of the geometry and Mach number on the supervelocities over a nonlifting body. In high subsonic conditions the flow over curved surfaces can surpass the speed of sound creating expansion waves or shock waves. The effect of shock waves is wave drag and possible separation of the boundary layer. It is therefore instrumental to know how the geometric shape of a body affects the increase in local Mach number.

6.2.1 Subsonic Inviscid Flow

This section partially follows the introduction to pressure fields and fluid acceleration as presented by Shapiro [51]. In Chap. 2 we derived the Euler equations in Cartesian coordinates. Along a streamline we can reduce the system of equations according to:

$$\mathrm{d}p = -\rho V \mathrm{d}V \tag{6.8}$$

We can derive a relation between the local pressure in the fluid and the local velocity. We can integrate both sides of (6.8) between two arbitrary points along the streamline. If we assume that the flow is incompressible (i.e. $\rho_1 = \rho_2 = \rho$) we obtain Bernoulli's equation (see Problem 6.3):

$$p_1 + \frac{1}{2}\rho V_1^2 = p_2 + \frac{1}{2}\rho V_2^2 \tag{6.9}$$

For incompressible flow we can therefore conclude that:

$$p_t \hat{=} p + \frac{1}{2}\rho V^2 = \text{constant along a streamline} \tag{6.10}$$

The second term in (6.10) is the dynamic pressure, often denoted with q. Similar to the static pressure, p, the dynamic pressure is a scalar. Bernoulli's equation literally states that the local velocity is inversely proportional to the square root of the local pressure.

The pressure coefficient may be written as

$$C_p \hat{=} \frac{p - p_\infty}{q_\infty} \tag{3.11}$$

Note that the subscript ∞ implies that we are dealing with a point in the flow at an infinite distance from the measuring point. This is referred to as the freestream condition. Substituting (6.10) and assuming incompressible conditions yields the following expression for the pressure coefficient:

$$C_p = 1 - \left(\frac{V}{V_\infty}\right)^2 \tag{6.11}$$

This relation directly ties the pressure coefficient to the local velocity. We can approximate this equation by assuming that the local velocity is a relatively small deviation from the freestream velocity: $V = V_\infty + \Delta V$ and $\Delta V / V_\infty \lll 1$. In that case, (3.11) reduces to:

$$C_p = -2\frac{\Delta V}{V_\infty} \tag{6.12}$$

We now have a very simple linear relationship between the supervelocity, ΔV, and the pressure coefficient, C_p. Next, we have to correlate the pressure coefficient to the local curvature of the streamlines.

Perpendicular to the streamline we can derive a relation between the pressure on a fluid particle and its velocity along a curved streamline. A schematic drawing of such a streamline is shown in Fig. 6.3. We define the direction perpendicular to the streamline as n, and along the streamline with s. The free-body diagram (FBD) shows the pressure forces that are acting on this fluid particle in the n-direction, in inviscid, irrotational flow, while the kinetic diagram (KD) shows its centripetal acceleration. If we assume the dimensions of the fluid particle to be Δs in length and Δr in width, then Newton's second law reduces to:

$$\frac{mV^2}{r} = (p + \Delta p - p)\Delta s \tag{6.13}$$

We know that $\Delta p = (\mathrm{d}p/\mathrm{d}r)\Delta r$ and that $m = \rho \Delta s \Delta r$. Combining this with (6.13) yields the following relation:

$$\frac{\rho V^2}{r} = \frac{\mathrm{d}p}{\mathrm{d}r} \tag{6.14}$$

This relation shows that the pressure always increases outward from the center of curvature.

We find curved streamlines over curved bodies in subsonic, transonic and supersonic flows. These bodies can be concave or convex (see Fig. 6.4). If the body is convex the normal vector to the body wall, n is defined in the same direction as r in Fig. 6.3 and the pressure gradient, $\mathrm{d}p/\mathrm{d}n$ is therefore positive. In other words, the pressure is increasing with the distance from the wall. Because we know that

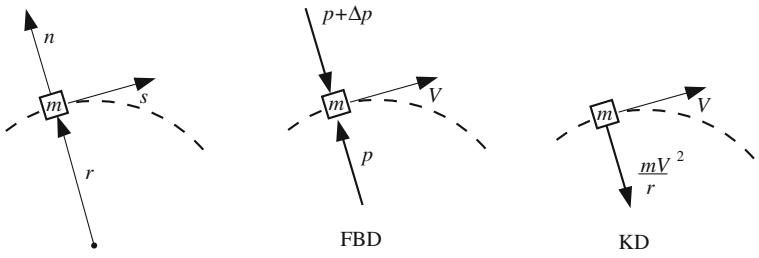

Fig. 6.3 Forces and accelerations on a fluid particle perpendicular to a curved streamline

the pressure at an infinite distance normal to the body should equal the freestream pressure, p_∞, we can deduce that the pressure at the wall, p, should be lower than p_∞. In other words, a convex shape leads to a reduction in pressure and consequently a negative pressure coefficient, C_p. A similar argument can be made for the concave shape. However, in this case the direction normal to the body wall, is in opposite direction to the radius vector, r. Therefore, the pressure gradient in this direction is negative and the pressure continuously decreases when we move further away from the wall. Consequently, we can deduce that the pressure at the wall should therefore be higher than the pressure infinity: $p > p_\infty$. The pressure coefficient at the body for a concave shape is therefore positive.

We have now qualitatively determined that streamlines along convex curves have decrease C_p and streamlines along concave curves increase C_p. In addition, we can see from (6.14) that the there is an inverse relation between the radius of curvature, r, and the pressure gradient, $\mathrm{d}p/\mathrm{d}n$. From this relation we can deduce that when $r \to 0$, the pressure gradient must tend to infinity, i.e. $\mathrm{d}p/\mathrm{d}n \to \infty$. We also see that when $\lim_{r\to\infty} \mathrm{d}p/\mathrm{d}n \to 0$ and that $V \to V_\infty$. The effect of the radius of curvature of the body, $r = R$, can be evaluated on a qualitative basis. We can plot the pressure coefficient C_p as a function of the distance from the center of curvature r, using the aforementioned relations at the respective boundaries at $r = 0$ and $r \to \infty$. This is shown in Fig. 6.5. We can observe that the position of the wall has an effect on the local pressure, p, at $r = R$. Whenever the wall is positioned close to the center of

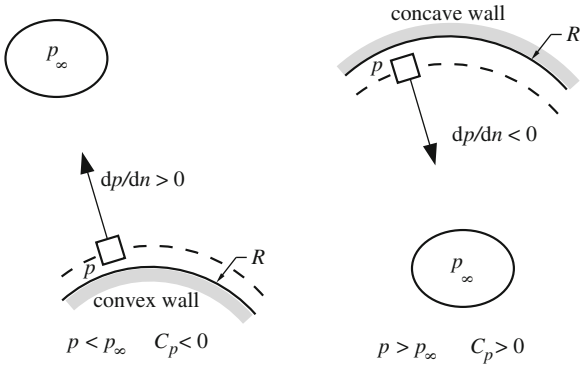

Fig. 6.4 Relation between body curvature and pressure coefficient

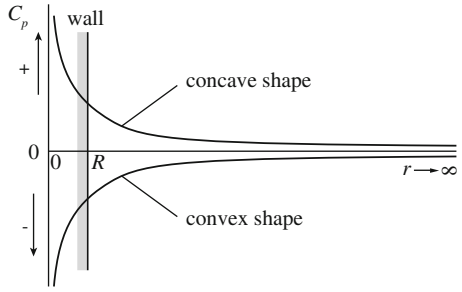

Fig. 6.5 Qualitative relation between pressure and radius of curvature

curvature (i.e. it has a large curvature itself) the pressure difference between $p_r = R$ and p_∞ is large and we have a high C_p. Conversely, when R is large (i.e. the wall has little curvature) the pressure difference is much smaller and C_p tends to zero. Hence, on a purely qualitative basis we can state that the radius of curvature of the body is negatively related to the pressure coefficient. In other words, the larger the curvature, the higher the absolute value of the pressure coefficient.

We can combine the relation between curvature and C_p and between C_p and ΔV in a straightforward manner. We know that when a geometry displays a convex curvature the pressure coefficient, $C_p < 0$. Consequently, employing (6.12) we note that the supervelocity, $\Delta V > 0$. A convex curvature, therefore, leads to local speeds that surpass the freestream velocity. Similarly, when the geometry has a concave curvature, the pressure coefficient is positive and $\Delta V < 0$. Concave shapes therefore reduce the speed of the fluid near the body. Finally, we can state that the absolute curvature (whether convex or concave) has a magnification effect on ΔV. A body with sharp corners, for example, yields a large speed fluctuations at these corners, while a body with little curvature only induces mild speed variations.

Now that we have established the effect of local curvature on the pressure coefficient, we take a look at the distribution of the pressure coefficient over a body. The value of the pressure coefficient at various locations on the body is often termed the pressure distribution. Strictly speaking this is incorrect. However, we have used the term "pressure distribution" in relation to the C_p distribution and we will continue to do so in this chapter. In subsonic flow, the pressure at any point A has an effect on the pressure at an arbitrary point B (point B is in point A's "region of influence"). Every change in pressure coefficient due to the presence of curvature at point A therefore also affects the pressure coefficient at any other arbitrary point B on that body. This makes the intuitive prediction of the pressure coefficient somewhat more difficult. However, we can still relate the geometric features of a given body to its pressure distribution by relating the *change* in C_p to the local curvature. For example, if the flow encounters a convex shape with a small radius of curvature we expect a sharp increase in local suction. Conversely, if the flow encounters a concave shape with a large radius of curvature, we expect a gradual increase in local pressure.

This is shown in Fig. 6.6 where two axis-symmetric bodies of identical thickness-to-length ratio are placed in an axial flow field. The ellipsoid has a blunt leading edge, which leads to a high local curvature. The C_p therefore increases rapidly. Because the curvature over the ellipsoid is low over the center section of the body, the pressure coefficient shows little variance. The absence of the blunt leading edge on the paraboloid makes for a more gradual increase of the pressure coefficient. However, due to the higher curvature in the center section, the pressure coefficient reaches a higher peak.

In Fig. 6.7 we show the pressure distribution over an important part of the fuselage: the cockpit. In this case, the aircraft in question has been modified with the addition of a large nose fairing (radome) to house a radar. The radome has a significant impact on the pressure distribution over cockpit. The pressure distribution over the top of the fuselage shows the most erratic behavior. Initially the flow is accelerated from near stagnation pressure ($C_p = 1$) at the nose towards a minimum of about

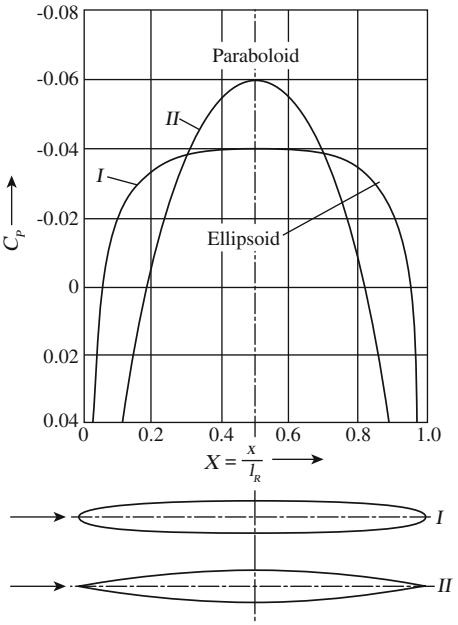

Fig. 6.6 Pressure distribution over an *ellipsoid* and *paraboloid* of identical maximum thickness and length at incompressible axial flow (after Ref. [49])

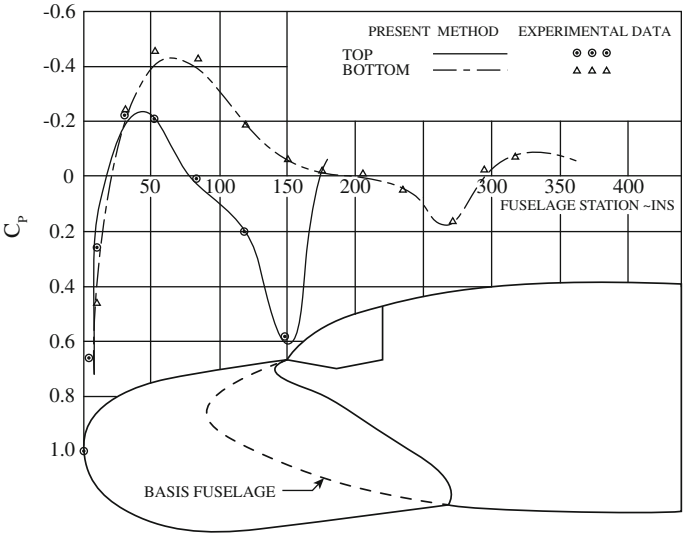

Fig. 6.7 Pressure distributions on a C-135 fuselage with a large radome at zero angle of attack (after Ref. [6])

$C_p = -0.24$. Then, the flow decelerates once more to a value close to stagnation at the kink between the radome and the cockpit window. Due to the high convex curvature over the window, the flow accelerates rapidly beyond the kink. At the bottom curve we also see the presence of the concave kink between fuselage and radome in the pressure distribution. Before the kink the velocity on the uncurved part of the radome is close to its freestream value ($C_p \approx 0$). At the kink the flow decelerates ($C_p > 0$) after which it accelerates once more over the convex part of the lower fuselage.

Example 6.1 Below an axis-symmetric body is shown. Assuming inviscid, incompressible flow, sketch the notional pressure distribution about this body.

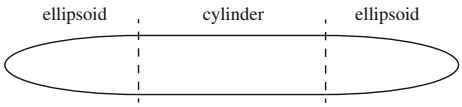

Solution:

We first identify some of the key characteristics of the body under consideration. Since we consider inviscid conditions we have a stagnation point at the leading edge and at the trailing edge where the pressure coefficient is 1. This body has a blunt nose, so we expect a sharp increase in suction over the first few percent of the body. Then the curvature decreases, and so does the flow velocity. Hence the slope $\mathrm{d}C_p/\mathrm{d}x$ reduces. Once the flow reaches the cylinder it does not see any change in curvature. Therefore, the flow decelerates towards freestream velocity. The C_p will therefore increase to a value close to 0. Even further downstream a convex shape is present again which accelerates the flow and creates a second suction peak. Finally, the flow decelerates to stagnation over the last few percent of the body. Due to the symmetric shape of the body we also expect a symmetric shape in pressure distribution. Applying this line of reasoning results in the notional pressure distribution drawn in Fig. 6.8.

6.2.2 *Effect of Subcritical Compressibility*

In high-subsonic flow, the effect of compressibility on the pressure coefficient has been discussed in Chap. 3. Using the Prandtl-Glauert compressibility correction, the

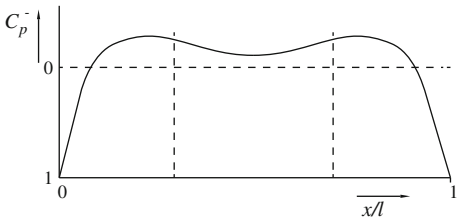

Fig. 6.8 Figure belonging to Example 6.1 (after Ref. [69])

compressible pressure coefficient, $(C_p)_{M_\infty}$ is related to the incompressible pressure coefficient according to:

$$(C_p)_{M_\infty} = \frac{(C_p)_{M_\infty=0}}{\sqrt{1-M_\infty^2}} \tag{6.15}$$

In other words, the pressure coefficient increases with the freestream Mach number up to infinity at $M_\infty = 1$. We know from practice that in reality this theoretical value is not reached. However, it does show qualitatively that the pressure coefficient and thus the supervelocities over a given body in high-subsonic flow are affected by the compressibility of the air.

Let us clarify this qualitative statement through the relationship between the pressure coefficient and Mach number in steady isentropic flow. If we employ the relation between Mach number and static temperature in isentropic conditions (2.147) and the relation between pressure and temperature (2.103), we have:

$$p_t = p\left(1+\frac{\gamma-1}{2}M^2\right)^{\frac{\gamma}{\gamma-1}} = p_\infty\left(1+\frac{\gamma-1}{2}M_\infty^2\right)^{\frac{\gamma}{\gamma-1}} \tag{6.16}$$

This relation shows that under the assumption of isentropic compression there is a relation between the local Mach number, M, and the Mach number at infinity, M_∞, via the static pressure. We use the following definition of the pressure coefficient:

$$C_p = \frac{2}{\gamma M_\infty^2}\left(\frac{p}{p_\infty}-1\right) \tag{3.11}$$

Combining (6.16) and (3.11) results in the following relation between pressure coefficient, local Mach number, and freestream Mach number:

$$M^2 = \frac{2}{\gamma-1}\left[\frac{1+\frac{\gamma-1}{2}M_\infty^2}{\left(1+\frac{1}{2}\gamma M_\infty^2 C_p\right)^{\frac{\gamma-1}{\gamma}}}-1\right] \tag{6.17}$$

For air flow about curved bodies this equation can be used up to a local Mach number of 1.58. This is the (theoretical) maximum supersonic speed that can be achieved over a body in subsonic flow. It will be derived in Sect. 7.5. A graphical overview relating the local Mach number to the pressure coefficient is shown in Fig. 6.9. It can be seen from this graph that high negative pressure coefficients (suction) in combination with moderate to high subsonic Mach numbers lead to a local Mach number well beyond 1.

If we define the increase in local Mach number as $\Delta M = M - M_\infty$ then we can also plot the relative increase in Mach number $\Delta M/M_\infty$. This is shown in Fig. 6.10. If we take this graph and we compare the relative increase in Mach number for $C_p = -1$ then we can see that for $M_\infty = 0.1$ the increase is around 42 %, while for $M_\infty = 0.8$ the increase is around 62 %. In other words, there is a progressive increase in local Mach number with increasing freestream Mach number.

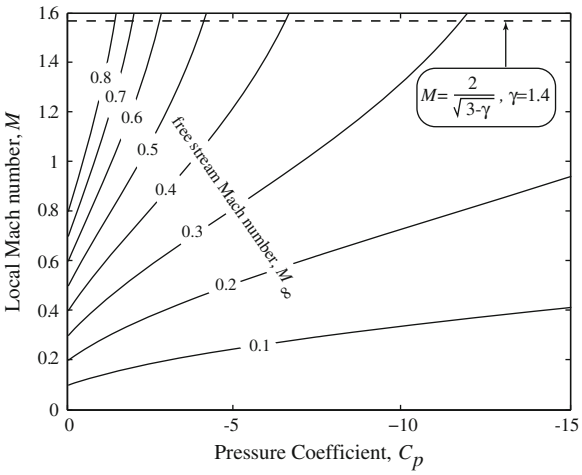

Fig. 6.9 Relation between local Mach number and pressure coefficient for various values of M_∞

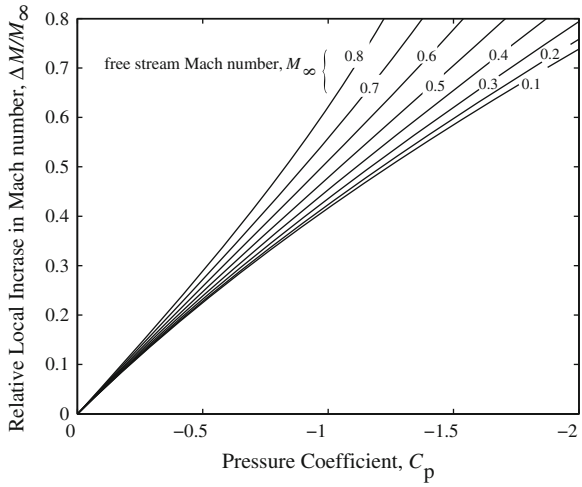

Fig. 6.10 Relation between relative local Mach number and pressure coefficient in regions with supervelocity for various values of M_∞

We have now established that the curvature in a body is directly responsible for the supervelocities about that body and the related pressure coefficient. In addition, we have shown that the local Mach number is strongly affected by the pressure coefficient and value of the freestream Mach number. This should give the reader some indication about the relation between the geometry of the body, the freestream Mach number and the expected pressure coefficient. In addition to the effect close to the body, the body has a larger effect on the streamlines further away from the body when the Mach number approaches 1. As can be seen in Fig. 6.11, at a Mach number of 0.8, region of influence is much larger that at a Mach number that is well-below 1. This is a second effect of compressibility that is important for transonic aircraft.

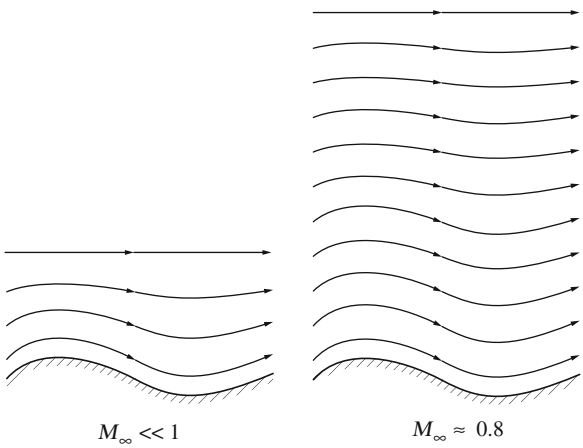

Fig. 6.11 Streamlines over a wavy wall (after Ref. [3])

As was established in Chap. 3, this effect plays an important role when wind tunnel tests are carried out to predict the aerodynamic coefficients of the airplane.

The displacement effect caused by the body on the streamlines far away from it continues to grow with Mach number. In supersonic conditions, the linearized potential theory shows that the streamlines even at an infinite distance from the body are affected. In fact, they follow exactly the same path as the wall itself. In supersonic conditions, it is the slope of the surface with respect to the freestream velocity vector that determines the local pressure coefficient [see (3.69)].

6.3 Wave Drag

The aerodynamic shape of high-subsonic aircraft is to be designed such that the Mach-dependent drag penalty in its cruise configuration is minimized. One instrument to do this is by creating a favorable cross-sectional area distribution of the airplane. In 1951 it was Adolf Büsemann who first described that a streamtube of air at near-sonic speeds no longer varied in diameter with speed but remained constant. Conversely, when a streamtube of air would flow over a curved surface, the velocity inside the tube would increase but its diameter would stay the same.

Let us investigate this claim by looking at the steady inviscid flow equations for a one-dimensional streamtube with a variable cross section A. The continuity equation (2.110) states that the mass flow entering a section of the streamtube equals the mass flow that exits the streamtube. In other words:

$$\rho u A = \text{constant} \tag{6.18}$$

The change in mass flow is therefore:

$$\mathrm{d}(\rho u A) = 0 \tag{6.19}$$

We can elaborate (6.19) by using logarithmic differentiation[1]:

$$\frac{\mathrm{d}\rho}{\rho} + \frac{\mathrm{d}u}{u} + \frac{\mathrm{d}A}{A} = 0 \tag{6.20}$$

The momentum equation (2.183) in steady one-dimensional flow reduces to:

$$\mathrm{d}p = -\rho u \mathrm{d}u \tag{6.21}$$

Furthermore, we have already seen that the speed of sound can be written as:

$$a = \sqrt{\left(\frac{\mathrm{d}p}{\mathrm{d}\rho}\right)} \tag{2.106}$$

If we combine (6.19), (6.21), and (2.106), we can show that (see Problem 6.8):

$$\frac{\mathrm{d}A}{A} = \left(M^2 - 1\right)\frac{\mathrm{d}u}{u} \tag{6.22}$$

We observe that when $M = 1$, $\mathrm{d}A/A = 0$ even though a finite $\mathrm{d}u$ exists. This shows that Büsemann's claim is indeed true for flows near the speed of sound. It also corresponds to our earlier observation that the region of influence in transonic conditions is much larger than in subsonic conditions. Streamtubes around a body (or wavy wall, as in Fig. 6.11) are simply displaced rather than reduced in area. At $M = 1$ this effect extends, in theory, to infinity.

Richard Whitcomb realized that the individual streamtubes over a wing-body combination would interfere with each other due to dramatic increases in cross-sectional area where the wing joined the fuselage. Rather than looking at the shape of the wing and fuselage separately he postulated that one needed to look at the cross-sectional area of the entire airplane configuration and keep it as smooth a curve as possible as it increased and decreased around the fuselage, wing, and empennage. This design rule to minimize wave drag was termed the Whitcomb transonic area rule [63]. The area rule states that the wave drag of an airplane configuration depends primarily on the longitudinal distribution of the total cross-sectional area. This tells us that a simple body of revolution that has the same distribution of cross sectional area as a complex airplane produces the same wave drag. To evaluate the wave drag of such a complex aircraft we can therefore reduce the complexity of the problem by evaluating its equivalent axis-symmetric body. The equivalent body can be constructed by measuring the cross-sectional area of a fuselage station perpendicular to the longitudinal axis of the airplane (see Fig. 6.12).

To demonstrate the applicability and limitations of the area rule, Fig. 6.13 shows a comparison study carried out in the wind tunnel by Chan [8, 9]. Four different wind tunnel models are subjected to a Mach number ranging from 0.8 to 1.1. We see a

[1] See a text book on calculus such as Ref. [2] for details on logarithmic differentiation.

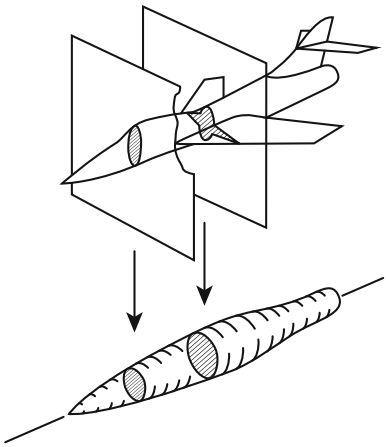

Fig. 6.12 Procedure for obtaining the axis-symmetric equivalent body of a complex airplane (after Ref. [68])

swept-wing configuration with its equivalent body (1) and a delta-wing configuration with its equivalent body (2). The equivalent bodies are axisymmetric and have the same cross-sectional area distribution as the swept-wing configuration and delta-wing configuration, respectively. The graph shows us the variation in zero-lift drag coefficient of the four wind tunnel models over the Mach range. We see that when the Mach number is increased beyond $M = 0.9$ all models show a significant increase in drag. This drag is attributed to the formation of shock waves and is therefore

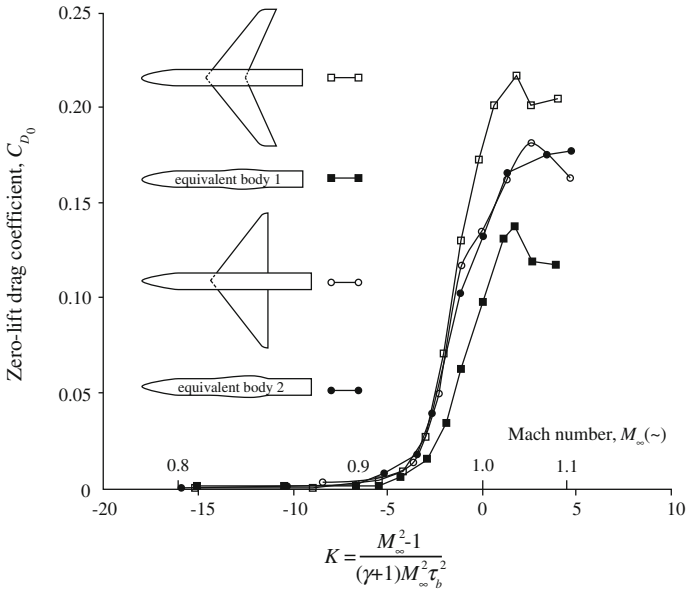

Fig. 6.13 Zero-lift drag coefficient of wing-body combinations and their equivalent axisymmetric bodies (data from Refs. [8, 9])

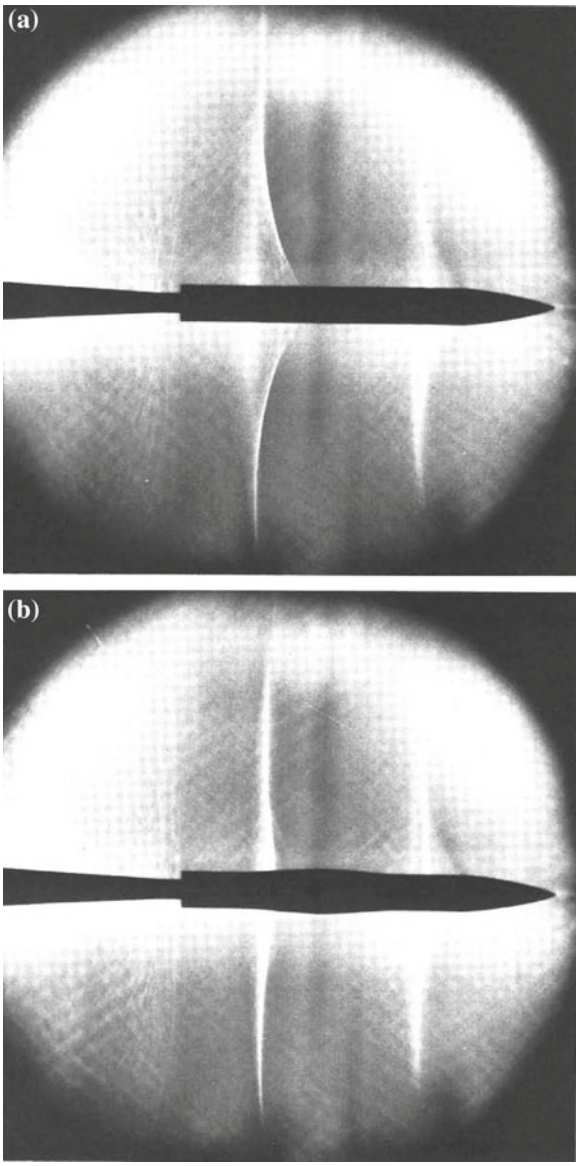

Fig. 6.14 Schlieren visualization for swept-wing configuration and equivalent body at zero angle of attack and $M = 0.98$ (from Ref. [9]). **a** Swept wing configuration. **b** Equivalent body

termed *wave drag*. This wave drag can be quantified by the momentum deficiency over the shock wave as we have seen in Sect. 6.4.3. If we compare the curves for the delta-wing configuration and its equivalent body, we see that their wave drag in the transonic domain is very similar. This is in line with Whitcomb's area rule. However, when we look at the comparison between the swept-wing configuration and its equivalent body, we notice that there is a significant difference between the wave drag of the two bodies.

Let us investigate why there is such a strong difference between the swept-wing configuration and its equivalent body. It is expected that the formation of shock waves is an important reason for discrepancy. Since pressure waves, such as shock waves or Mach waves, induce density gradients in the flow, schlieren optics is an often used tool to visualize these waves and the flow field. Schlieren (German, meaning "streaks") optics captures density gradients in compressible flows. The physical principle behind such visualization techniques as schlieren or shadowgraph is based on light beam deflection as it propagates through a medium with density gradients. For details of these flow visualization techniques, their distinguishing features, limitations and applications, the reader may refer to classical gas dynamic books such as Shapiro [50], Liepmann and Roshko [37], Ferri [20] or books on wind tunnel testing principles. Figure 6.14 shows schlieren images of the two wind tunnel models at $M = 0.98$. We see that both models show shock waves in the same longitudinal position. However, the shock wave over the wing of the swept-wing model is much stronger than the corresponding shock wave over the equivalent model. The shock wave over the swept-wing model causes boundary-layer separation at the outer portion of the wing which causes additional drag with respect to the equivalent body. This explains the larger drag over the swept-wing configuration compared to its equivalent body.

Based on the observations above, we conclude that the area rule works well for delta-wing aircraft of low aspect ratio but works less well for swept-back wing-bodies with moderate aspect ratio. The area rule is therefore limited to low-aspect-ratio thin-wing body combinations. Viscous effects, such as shock-wave-boundary-layer interaction, prevent a correct application of the area rule to wing-body combinations with higher aspect ratio or thicker wings.

6.3.1 Calculation of Pressure Drag by Use of Momentum Theory

There is a large body of literature that supports the concept of the transonic area rule in order to minimize the wave drag of a nonlifting body in transonic conditions, e.g. Ref. [65]. We would like to know what cross-sectional area distribution would give us the lowest wave drag. In the analysis that develops in this section we follow the classic text of Ashley and Landahl for the computation of wave drag in inviscid flow [4].

We start the derivation of wave drag in supersonic flow by looking at the axis-symmetric body in uniform flow conditions. A two-dimensional representation of such a body is presented in Fig. 6.1. The force acting on this body is governed by (6.3). We introduce unit normal vector, $\boldsymbol{n}$, such that we can bring both terms on the RHS of (6.3) within a single integral:

$$\boldsymbol{F}_{\text{body}} = -\iint_S [\rho \boldsymbol{V}(\boldsymbol{V}\cdot\boldsymbol{n}) + p\boldsymbol{n}]\mathrm{d}S \tag{6.23}$$

In this equation $\boldsymbol{n}\mathrm{d}S = \mathbf{d}\boldsymbol{S}$. Under the same assumptions, the continuity equation in integral form (2.110) can be written as follows:

$$\iint_S \rho(\boldsymbol{V}\cdot\boldsymbol{n})\mathrm{d}S = 0 \tag{6.24}$$

At this point we introduce a normalized disturbance velocity vector $\boldsymbol{v}$, which is defined as follows:

$$\boldsymbol{v} = \frac{\nabla\phi}{V_\infty} = \frac{\boldsymbol{V}}{V_\infty} - \boldsymbol{i} \tag{6.25}$$

Here V_∞ is the freestream velocity in the x-direction and $\boldsymbol{i}$ is the unit vector parallel to the x-axis. Note that this perturbation function $\boldsymbol{v}$ represents the normalized perturbation to the velocity field in x, y, and z direction, assuming that the freestream is aligned with the x-axis. Substituting (6.25) into (6.23) we obtain the following expression:

$$\mathbf{F}_{\text{body}} = -\iint_S p\boldsymbol{n} + \rho V_\infty^2\,(\boldsymbol{v}+\boldsymbol{i})\,(\boldsymbol{v}\cdot\boldsymbol{n}+\boldsymbol{i}\cdot\boldsymbol{n})\,\mathrm{d}S \tag{6.26}$$

Similarly, the continuity (6.24) can be written as:

$$\iint_S \rho\,(\boldsymbol{v}+\boldsymbol{i})\cdot\boldsymbol{n}\mathrm{d}S = 0 \tag{6.27}$$

We can employ the continuity (6.27) to show that (6.26) can be simplified. If we assume that S is an enclosed surface we can introduce the freestream static pressure, p_∞, and reduce the momentum equation to (see Problem 6.9):

$$\mathbf{F}_{\text{body}} = -\iint_S (p-p_\infty)\,\boldsymbol{n} + \rho V_\infty^2\boldsymbol{v}\,(\boldsymbol{v}\cdot\boldsymbol{n}+\boldsymbol{i}\cdot\boldsymbol{n})\mathrm{d}S \tag{6.28}$$

Equation (6.28) is a compact equation that relates the total body force to the properties of the freestream flow (p_∞, V_∞) and the local perturbation velocities ($\boldsymbol{v}$), density (ρ) and pressure p under the assumption of an inviscid and steady state flow.

We are interested in calculating the wave drag of a three-dimensional body in supersonic flow. An example of such a body in its cylindrical control volume is shown in Fig. 6.15. The surface area, S of the control volume is divided into three parts marked S_1–S_3. Let us first extract the drag force, D, from (6.28):

$$D = F_{\text{body}_x} = -\iint_S (p-p_\infty)\,\boldsymbol{i} + \rho V_\infty^2 u\,(\boldsymbol{v}\cdot\boldsymbol{n}+\boldsymbol{i}\cdot\boldsymbol{n})\,\mathrm{d}S \tag{6.29}$$

We write the normalized perturbation velocity in terms of the perturbation velocity potential in cylindrical coordinates according to:

$$\boldsymbol{v} = \frac{1}{V_\infty}\begin{pmatrix}\phi_x\\ \phi_r\end{pmatrix} = \begin{pmatrix}\hat{\phi}_x\\ \hat{\phi}_r\end{pmatrix} \tag{6.30}$$

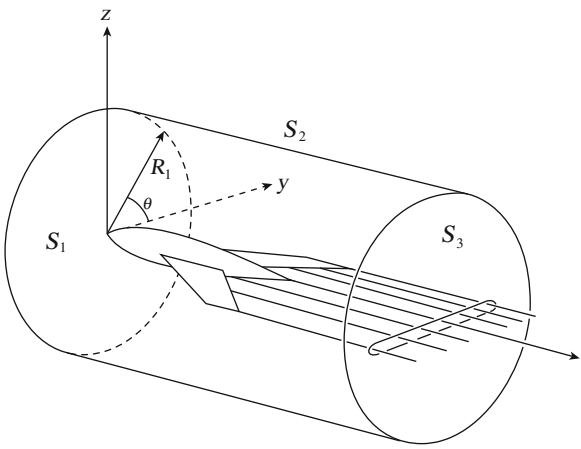

Fig. 6.15 Momentum control surface around a body in supersonic flow (modified from Ref. [4])

Furthermore, we note that in cylindrical coordinates:

$$\boldsymbol{n}\mathrm{d}S_1 = \begin{pmatrix} \mathrm{d}S_1 \\ 0 \end{pmatrix} \quad \boldsymbol{n}\mathrm{d}S_2 = \begin{pmatrix} 0 \\ \mathrm{d}S_2 \end{pmatrix} \quad \boldsymbol{n}\mathrm{d}S_3 = \begin{pmatrix} \mathrm{d}S_3 \\ 0 \end{pmatrix} \tag{6.31}$$

We can now rewrite (6.29) as follows:

$$\begin{aligned} D = &- \iint_{S_1} (p - p_\infty)\mathrm{d}S_1 - \iint_{S_1} \rho V_\infty^2 \hat{\phi}_x(\hat{\phi}_x + 1)\mathrm{d}S_1 - \iint_{S_2} \rho V_\infty^2 \hat{\phi}_x \hat{\phi}_r \mathrm{d}S_2 \\ &- \iint_{S_3} (p - p_\infty)\mathrm{d}S_3 - \iint_{S_3} \rho V_\infty^2 \hat{\phi}_x(\hat{\phi}_x + 1)\mathrm{d}S_3 \end{aligned} \tag{6.32}$$

We can simplify this expression by acknowledging that in supersonic flow the pressure and velocity at S_1 must remain unperturbed by the body (i.e. $p = p_\infty$ and $n\hat{\phi}_x = 0$). Similarly, we assume that at S_3 is sufficiently far behind the body such that the flow has become essentially two-dimensional in the y–z plane ("Trefftz plane"). Therefore, $\hat{\phi}_x = 0$ such that the last integral in (6.32) vanishes. In addition, we employ Bernoulli (6.9) to relate the pressure to the velocity disturbance velocity potential in cylindrical coordinates:

$$p - p_\infty = -\frac{1}{2}\rho V_\infty^2 \left(\hat{\phi}_r^2 + 2\hat{\phi}_x + \hat{\phi}_x^2\right) \tag{6.33}$$

We can use this relation to write $p - p_\infty$ only in terms of $\hat{\phi}_r$ since $\hat{\phi}_x = 0$ at S_3. Finally, we note that $\hat{\phi}_r^2 = \hat{\phi}_y^2 + \hat{\phi}_z^2$. Combining all of the information above we can now rewrite (6.32) according to:

$$D = -\rho V_\infty^2 \iint_{S_2} \hat{\phi}_x \hat{\phi}_r \mathrm{d}S_2 + \frac{\rho V_\infty^2}{2} \iint_{S_3} (\hat{\phi}_y^2 + \hat{\phi}_z^2)\mathrm{d}S_3 \tag{6.34}$$

This equation expresses the total pressure drag experienced by the body. In supersonic flow, the pressure drag stems from two sources: the wave drag and the vortex drag. The second integral in (6.34) gives the vortex drag, which is identical to the induced drag for subsonic flow. The first integral represents the wave drag:

$$D_{\text{wave}} = -\rho V_\infty^2 \iint_{S_2} \hat{\phi}_x \hat{\phi}_r \mathrm{d}S_2 \tag{6.35}$$

This is a remarkably simple expression for the wave drag in terms of the derivatives of the perturbation velocity potential. We must note that the present result is only valid for bodies that are pointed in the rear.

6.3.2 *Supersonic Wave Drag of a Slender Axis-Symmetric Body*

It can be shown that flow around a body can be constructed by adding elementary source solutions. Examples of this technique can be found in text books on the fundamentals of aerodynamics such as Ref. [3]. In spherical coordinates a point source should satisfy Laplace's equation for incompressible conditions: $\nabla^2 \Phi = 0$. In spherical coordinates it can be shown that a source of strength Q located at $r = 0$ has the potential function: $\Phi = -Q/4\pi r$ [see also (3.88)]. Since the disturbance velocity potential can be expressed as a function of the velocity potential [$\Phi = V_\infty(x + \hat{\phi})$] we write for the disturbance velocity potential in spherical coordinates:

$$\hat{\phi} = -\frac{Q}{4\pi r V_\infty} \tag{6.36}$$

where r is the distance measured at any point to the origin of the source.

Since we know that the superposition of elementary sources can represent the shape of any axis-symmetric body we would like to know what the wave drag would be of a line of sources. Therefore, we introduce a so-called lineal source distribution: a straight line of sources of strength $Q = V_\infty f(x)$. Here, $f(x)$ represents the variable source strength along the line. Without derivation we show that the associated perturbation velocity potential in supersonic flow is [4]:

$$\hat{\phi} = -\frac{1}{2\pi} \int_0^{x-\beta r} \frac{f(x_1)\mathrm{d}x_1}{\sqrt{(x - x_1)^2 - \beta^2 r^2}} \tag{6.37}$$

where $\beta = \sqrt{M^2 - 1}$ and r is the distance from any point in space to the origin of the y–z plane. We assume that f is continuous and that $f(0) = f(l) = 0$. We can substitute (6.37) in (6.35) to find a closed-form expression of the wave drag. The derivation involves complex algebraic operations that are beyond the scope of this

book. Reference [4] can be consulted for details on the exact derivation. We merely present the reader with the result:

$$D_{\text{wave}} = -\frac{\rho_\infty V_\infty^2}{4\pi} \int_0^l \int_0^l f'(x_1) f'(x_2) \ln|x_2 - x_1| \, \mathrm{d}x_1 \mathrm{d}x_2 \tag{6.38}$$

For $f(l) = 0$ we can rewrite (6.38) according to:

$$D_{\text{wave}} = -\frac{\rho_\infty V_\infty^2}{2\pi} \int_0^l f'(x) \mathrm{d}x \int_0^x f'(x_1) \ln(x - x_1) \mathrm{d}x_1 \tag{6.39}$$

If we compare (6.37) with (6.39) we notice that the drag coefficient has become independent of β provided that the body ends in a point (as in Fig. 6.15) or ends in a cylindrical portion. Finally, the tangentiality condition at the surface of the bodies relates the source strength to the first derivative of the cross-sectional area, S:

$$f(x) = S'(x) \tag{6.40}$$

Example 6.2 We consider a body of revolution with the following radius distribution:

$$R(x) = \frac{1}{4} - \left(x - \frac{1}{2}\right)^2 \quad \text{for} \quad 0 \le x \le 1$$

(a) In one figure, plot the distribution of R, S, and S' as function of x
(b) Calculate the drag coefficient of this body with respect to the unit square as reference area.

Solution:

(a) We first calculate the cross-sectional area distribution that corresponds to this radius distribution:

$$S(x) = \pi R^2(x) = \pi \left[\frac{1}{4} - \left(x - \frac{1}{2}\right)^2\right]^2$$

Subsequently, we determine the derivative of the cross-sectional area distribution with respect to x:

$$S'(x) = -4\pi \left[\frac{1}{4} - \left(x - \frac{1}{2}\right)^2\right]\left(x - \frac{1}{2}\right)$$

The results are plotted in Fig. 6.16.

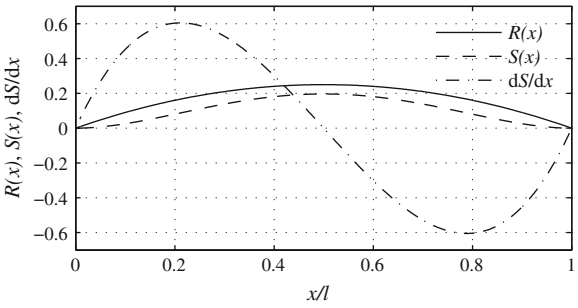

Fig. 6.16 Distribution of radius, cross-sectional area, and cross-sectional area derivative

(b) To calculate the wave drag coefficient with respect to the frontal area ($\pi/16$) we rewrite (6.39) accordingly:

$$C_{D_{\text{wave}}} = -\frac{16}{\pi^2}\int_0^l f'(x)\mathrm{d}x \int_0^x f'(x_1)\ln(x-x_1)\mathrm{d}x_1$$

For $f'(x)$ we write:

$$f'(x) = S''(x) = \pi\left[12\left(x-\frac{1}{2}\right)^2 - 1\right]$$

When examining (6.39) we notice that for $x = x_1$ the integrand of the second integral tends to negative infinity. This means that we cannot evaluate this integral using standard quadrature methods. We therefore replace the integral by a double series:

$$C_{D_{\text{wave}}} \approx -\tfrac{16}{\pi^2}\sum_{i=2}^{I}\left(f(x_i)\Delta x \sum_{j=1}^{i-1} f(x_j)\ln(x_i - x_j)\Delta x\right)$$
$$\text{where } x_i = x_j = [0, \Delta x, 2\Delta x, \ldots, 1]$$

We evaluate this double summation in Matlab and find for $\Delta x = 0.001$ and $I = 1{,}000$:

$$C_{D_{\text{wave}}} \approx 2.63$$

Note that this drag coefficient is calculated with respect to the frontal area of the body.

6.3.3 Optimum Shape of a Slender Body of Revolution

For a slender body of revolution, we are interested in the cross-sectional area distribution that yields the least amount of wave drag. We start from the the expression for

the wave drag (6.38). We first perform a coordinate transformation by introducing the Glauert variable, θ that relates to x according to:

$$x = \frac{l}{2}(1 + \cos\theta) \tag{6.41}$$

With this transformation the nose of the body is located at $\theta = \pi$, while the base is situated at $\theta = 0$. We can now express f as a Fourier series (see Sect. 2.2.2 for an introduction on Fourier series or consult Ref. [30]) in θ according to:

$$f(\theta) = l\sum_{n=1}^{\infty} A_n \sin(n\theta) \tag{6.42}$$

Likewise, we can express the Fourier coefficients, A_n, as a function of $f(\theta)$. We do this by multiplying either side by $\sin m\theta$ and integrating between 0 and π:

$$\frac{2}{\pi l}\int_0^{\pi} f(\theta)\sin n\theta \mathrm{d}\theta = A_n \tag{6.43}$$

Notice that we use the orthogonality of the Fourier terms such that:

$$\int_0^{\pi} \sin n\theta \sin m\theta \mathrm{d}\theta = \begin{cases} 0 & \text{for} \quad n \neq m \\ \pi/2 & \text{for} \quad n = m \end{cases} \tag{6.44}$$

To obtain the area distribution as a function of θ we use (6.40). We integrate (6.42) between θ and π, noting that $\mathrm{d}x = -\frac{l}{2}\sin\theta \mathrm{d}\theta$:

$$\begin{aligned} S(\theta) &= -\frac{l^2}{2}\int_{\theta}^{\pi}\sum_{n=1}^{\infty} A_n \sin(n\theta_1)\sin\theta_1 \mathrm{d}\theta_1 \\ &= \frac{l^2}{4}\left\{A_1\left(\pi - \theta + \frac{\sin(2\theta)}{2}\right) + \sum_{n=2}^{\infty} A_n\left[\frac{\sin(n+1)\theta}{n+1} - \frac{\sin(n-1)\theta}{n-1}\right]\right\} \end{aligned} \tag{6.45}$$

If we integrate the area distribution between 0 and π we obtain an expression for the volume of the body in terms of the first two Fourier coefficients:

$$\mathscr{V} = \frac{l}{2}\int_0^{\pi} S(\theta)\sin\theta \mathrm{d}\theta = \frac{\pi l^3}{8}\left(A_1 - \frac{1}{2}A_2\right) \tag{6.46}$$

Finally, we can obtain an expression for the wave drag in terms of the Fourier coefficients by substituting (6.42) in (6.38):

$$D_w = -\frac{\rho_\infty V_\infty^2 l^2}{16\pi}\int_{\pi}^{0}\int_{\pi}^{0}\sum_{n=1}^{\infty} A_n n\cos(n\theta_1)\sum_{m=1}^{\infty} A_m m\cos(m\theta_2)$$

$$\times \ln \left| \frac{l}{2}(\cos\theta - \cos\theta_1) \right| \sin\theta_1 \sin\theta_2 \mathrm{d}\theta_1 \mathrm{d}\theta_2$$

$$= \frac{\pi \rho_\infty V_\infty^2 l^2}{8} \sum_{n=1}^{\infty} n A_n^2 \tag{6.47}$$

where we use the properties of trigonometric functions as in (6.44).

Let us reflect on what we have done here. We have defined three properties of the body in terms of Fourier coefficients: the volume of the body, the cross-sectional area distribution, and the wave drag. For a body of a specified cross-sectional area distribution and length, we can find the wave drag of this body by employing (6.43) and (6.47). To calculate the associated volume of the body we can employ (6.46).

6.3.3.1 Sears-Haack Body

We consider a body which is pointed at both ends and has a given volume, $\mathscr{V}$. This implies that the cross-sectional area is zero at $\theta = 0$ and $\theta = \pi$. Via (6.45) and $S(0) = S(\pi) = 0$ we obtain that $A_1 = 0$. For a given volume and length we employ (6.46) to obtain a value for A_2:

$$A_2 = -\frac{16\mathscr{V}}{\pi l^3} \tag{6.48}$$

If we scrutinize (6.47) we can immediately see that in order to minimize D_{wave} we would have to ensure that as many Fourier coefficients as possible are equal to zero. In practice this means that the drag is smallest when only A_2 is non-zero while all the others are zero. Substituting (6.48) into the equation for the wave drag, (6.47), results in the equation for wave drag for this body:

$$D_{\text{wave}} = \frac{64\mathscr{V}^2}{\pi l^4} \rho_\infty V_\infty^2 \tag{6.49}$$

In order to find the ideal area distribution for this body one can substitute $A_1 = 0$, $A_2 = -16\mathscr{V}/\pi l^3$ into (6.45) and let all remaining $A_n = 0$. We then obtain the following equation:

$$S(\theta) = \frac{4\mathscr{V}}{\pi l} \left(\sin\theta - \frac{1}{3} \sin 3\theta \right) \tag{6.50}$$

This is is the cross-sectional area distribution that yields the lowest wave drag. The axis-symmetric body that it represents is termed the Sears-Haack body after the English scientist William Sears and the German scientist Wolfgang Haack, who independently derived (6.50). In Fig. 6.17 one can see a Sears-Haack body for a fineness ratio of approximately 6.8.

To minimize the zero-lift wave drag on any body in transonic flow, the cross-sectional area distribution should be as close as possible to the Sears-Haack body.

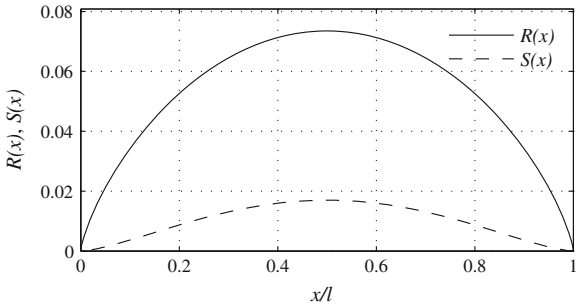

Fig. 6.17 Shape of an axisymmetric Sears-Haack body for $\mathscr{V} = 0.01$ and $l = 1$

The actual shape of the aircraft is fairly independent of its wave drag according to the theory of Büsemann and Whitcomb. It is therefore important that large volumetric additions to the body (e.g. wings, vertical and horizontal tail planes) are positioned such that a cross-sectional area distribution results that matches as closely as possible to the Sears-Haack body. Small deviations from the ideal Sears-Haack area distribution do not lead to excessive amounts of wave drag. However, discontinuities in area distribution can cause a large increase in wave drag and should therefore be avoided.

6.3.3.2 Von Kármán Ogive

The Sears-Haack body gives minimum drag for a body with a pointed nose and rear. A second shape of interest is the optimum nose cone shape for a straight body of revolution (e.g. a rocket, or bullet). If one applies different boundary conditions to (6.45) one can find the area distribution for which the nose cone produces minimum drag. For a nose cone with a given base area, $S(l)$, at $x = l$ we have $\theta = 0$. Substituting $\theta = 0$ in (6.45) we obtain:

$$A_1 = \frac{4S(l)}{\pi l^2} \tag{6.51}$$

Since A_1 is nonzero, the wave drag is minimized when $A_n = 0$ for $n \geq 2$. Substituting (6.51) into (6.47) one obtains the expression for the minimum wave drag of the nose cone:

$$D_w = \frac{2\rho_\infty V_\infty^2}{\pi} \frac{S(l)^2}{l^2} \tag{6.52}$$

If we substitute the expression for A_1 into (6.45) we obtain the area distribution for the minimum-drag nose cone:

$$S = \frac{S(l)}{\pi} \left(\pi - \theta + \frac{1}{2} \sin 2\theta \right) \tag{6.53}$$

This resulting body is called the Von Kármán ogive and gives the minimum drag for a given base area and length. Figure 6.18 shows an example of a Von Kármán ogive.

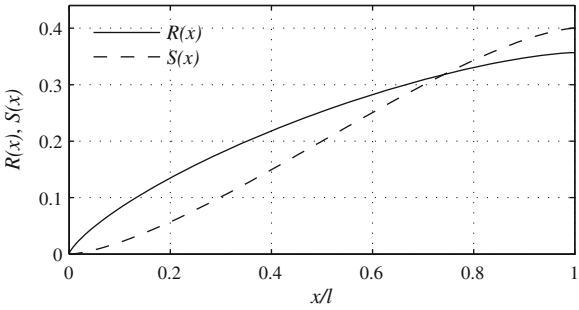

Fig. 6.18 Shape of an axis-symmetric Von Kármán ogive for $S(l) = 0.1$ and $l = 1$

6.3.4 Examples of Transonic Area Ruling

Application of the transonic area rule had the same objective as the supercritical airfoil and the swept wing concept: reduce wave drag in the transonic regime. Fighter aircraft at the time (e.g. Convair F-102) could not penetrate the sound barrier because of the exponential drag increase that they experienced near Mach 1. Their jet engines could not produce enough thrust to overcome the exponential increase in drag. The cross-sectional area distribution of the original YF-102a prototype (Fig. 1.12a) had such a high wave drag penalty near $M = 1$ that the available thrust could not overcome the drag. Flight tests showed that this aircraft could not exceed M = 0.98. This is shown in Fig. 6.19a where the thrust and the drag of the prototype aircraft are plotted at an altitude of 35,000 ft. Because the US Air Force was not satisfied with the maximum speed of this interceptor airplane a redesign was commissioned that had to result in a top speed of $M = 1.2$. This redesign included a narrower canopy, revised intakes, and a "pinched" fuselage (Fig. 1.12b). This dramatically altered the cross-sectional area distribution of the airplane resulting in a smaller increase in drag coefficient around $M = 1$ (see Fig. 6.19a) and a top speed of $M = 1.22$ as can be seen in Fig. 6.19b.

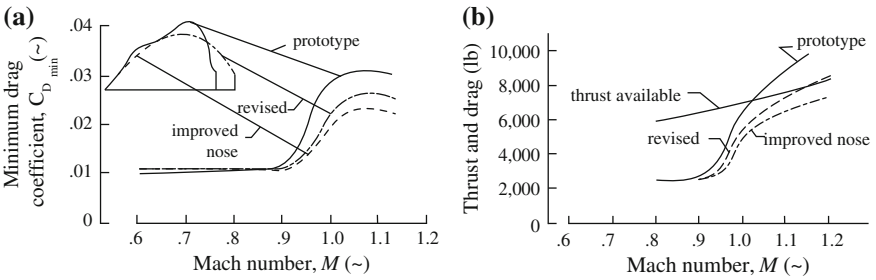

Fig. 6.19 Effect of cross-sectional area distribution on performance of the F-102 prototype at 35,000 ft (after Ref. [17]). **a** Drag coefficient and area distribution. **b** Drag an thrust versus Mach number

In the late 1960s when commercial transports started to emerge, it became evident that aircraft needed to be designed with the area rule and Sears-Haack body in mind. This resulted in some particular features of commercial transports that are still very obvious this day. An example of how the cross-sectional area distribution was altered on the Boeing 747 is shown in Fig. 6.20. It can be seen that by extending the upper deck the area distribution became more smooth, which resulted in a higher drag-divergence Mach number.

Another famous example of transonic area ruling is found in the anti-shock bodies that were developed by Whitcomb and Küchemann. The anti-shock bodies were positioned near the trailing edge of the wing to smoothen the cross-sectional area distribution of the airplane. The effect of these bodies was a reduction in shock strength over the upper surface of the wing, resulting in a lower wave drag. This was demonstrated by experiments at NASA, which are shown in Fig. 6.21. Notice the more aft position of the shock wave due to the application of the anti-shock bodies. Even though these bodies increased the wetted area of the airplane (i.e. more friction drag), their benefit in terms of wave drag reduction outweighed this penalty. The socalled *Küchemann carrots* found their way onto several aircraft such as the Convair 990 (fastest high-subsonic transport airplane to date) and the Handley Page Victor. Yet another aircraft that benefited from the research of Whitcomb and Küchemann was the Soviet Union's revolutionary Tu-95 bomber. The Tu-95 demonstrated the ability to cruise at jet-like speeds of Mach 0.85 while using propeller-driven engines. One of the reasons for this aircraft's exceptional performance was the use of large engine fairings aft of the inboard engines. These pods brought the external shape of the Tu-95 closer to the Sears-Haack body to reduce drag and increase maximum speed.

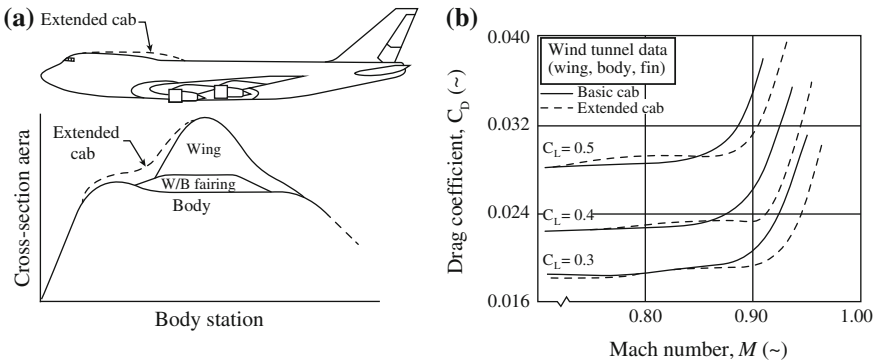

Fig. 6.20 Example of transonic area ruling on the Boeing 747 [24]. **a** Extended cab resulted in a smoother area distribution. **b** Drag-divergence Mach number increased substantially

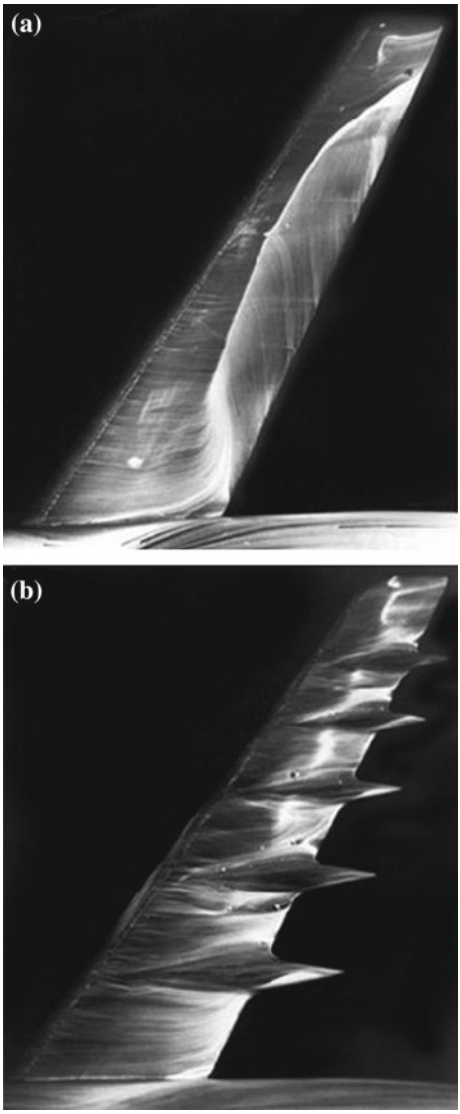

Fig. 6.21 Reduction of shock strength through the application of Küchemann bodies (*Photos* NASA). **a** Clean wing. **b** With Küchemann bodies

6.4 Fundamentals of Boundary-Layer Flow

Friction between a body and the surrounding fluid is one of the main causes of aircraft drag. On typical high-subsonic transports the friction drag is responsible for 40–60 % of the total drag of the airplane [57]. Every component (lifting or nonlifting) of the aircraft that is wetted by the flow contributes to the friction drag of the airplane. An obvious way to reduce friction drag is therefore to reduce the total *wetted area*.

Alternatively, the *friction coefficient* can be reduced. To understand the causes of friction we need to take a detailed look into the physics of the boundary layer, the thin viscous layer in between the virtually inviscid flow and the body.

When the boundary layer separates from the body, it creates a wake between the body and the continuous streamlines. A large momentum deficiency exists in the wake, which can contribute to a significant amount of drag. In addition, the pressure distribution over the body is significantly altered when separation occurs. In normal operating conditions, separation of the boundary layer is therefore to be prevented on any part of the airplane, whether intended to generate lift or not. The most noticeable limitation that boundary-layer separation poses is on the stall speed of an aircraft. At stall, the lift over the wing reduces significantly while the drag rises rapidly. Via the aviation regulations it has been established that the minimum approach speed of the aircraft (which relates to the required landing length of the aircraft) should be $\approx$23 % higher than the stall speed measured at 1-g conditions according to FAR/CS-25 regulations. This means that in practice, an airplane flies only at 2/3rd of its maximum lift coefficient. The latter is, in turn, governed by the separation of the boundary layer on the wing and is therefore an important constraint during the aerodynamic design of an aircraft.

Even though low-speed stall is arguably the most renown result of boundary-layer separation, it plays an important role in determining the maximum cruise altitude of high-subsonic aircraft. Boundary layers are prone to separate when a relatively large adverse pressure gradient is present and the boundary layer has thickened considerably. Such conditions occur for example on the upper wing surface when a shock wave is present. This instantaneous jump in local pressure can cause boundary layer separation at the foot of the shock wave. However, not only on the wing do we find areas that require the attention of the aerodynamic designer. Also on non-lifting bodies such as the rear of the fuselage that often has a considerable amount of upsweep (read: curvature) to allow for airplane rotation during take-off. Other areas where sharp adverse pressure gradients occur are also suspect: edges of cockpit windows, intersections between wing, nacelle and pylon, and the engine intake.

In the subsequent sections we discuss both qualitative and quantitative aspects of the boundary layer and their effect on friction drag. We follow the classical presentation of Abernathy [1] on the fundamentals of boundary layers.

6.4.1 Laminar Boundary Layer

In steady potential flow the inertia forces of the fluid are balanced by pressure forces. Viscosity does not play any role. If we consider the potential flow about a thin plate attached to a cylinder, Fig. 6.22a, we see that near the body the streamlines follow the contours of the body perfectly. Two stagnation points are present, one on the leading edge of the plate and one on the opposite end of the cylinder. In high-Reynolds-number flow, however, the effect of viscosity dominates the flow around

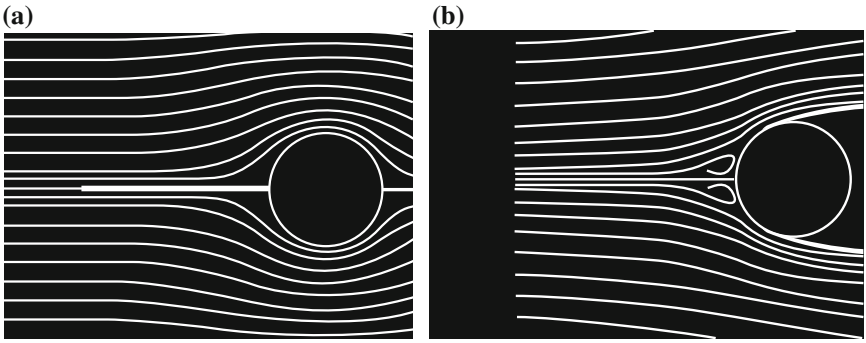

Fig. 6.22 Flow visualization of flow around a thin plate attached to a cylinder (after Ref. [1]). **a** Potential flow streamlines. **b** Streamlines of water flowing past the object

the boundaries of the body Fig. 6.22b. We see that the streamlines do not follow the curvature of the body anymore but separate from the surface near the top and bottom of the cylinder.

If we consider the flow past a simple symmetric airfoil and we assume that the Reynolds number is relatively large and the airfoil is aligned with the direction of the freestream, then the effect of viscosity is confined to a very narrow region close to the body. The streamlines about the the airfoil resemble very much the potential flow streamlines (see Fig. 6.23a). Now, when we place this same airfoil at a significant incidence angle with respect to the freestream flow direction, the viscous effects become very pronounced and the flow field about the airfoil is completely changed (Fig. 6.23b). The airfoil is said to be in a *stalled* condition. The boundary layer has separated from the surface and a large wake is present between the streamlines and the body. Separation is caused by a large adverse pressure gradient on the body surface which causes separation of the boundary layer.

We first look at the development of a boundary layer in the absence of any pressure gradient. In Fig. 6.24 the velocity profile of the flow about a flat plat is represented by white areas. We clearly see that there is a no-slip condition at the wall: the fluid is at

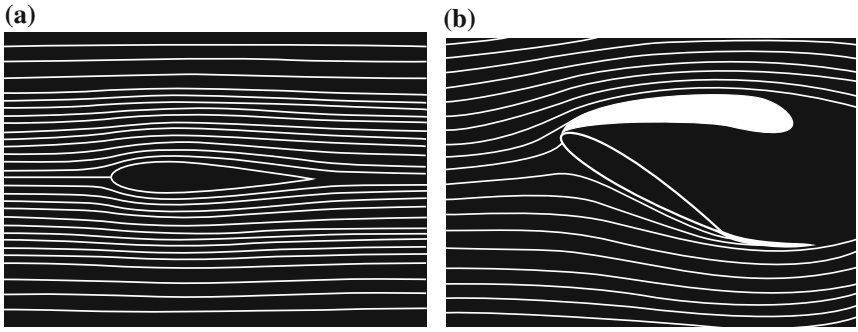

Fig. 6.23 Flow visualization of flow past an airfoil (after Ref. [1]). **a** At small angle of attack. **b** At high angle of attack

Fig. 6.24 Flow visualization of velocity profiles within the boundary layer about a flat plate (after Ref. [1])

a standstill there. With increasing distance from the wall, y, the velocity, u, increases progressively until a point where it matches the freestream value, U. We typically define the thickness of the boundary layer, δ, as the y coordinate where the velocity vector reaches 99 % of the freestream value. If we look progressively downstream we see that the thickness of the boundary layer increases, while the velocity gradient, $\mathrm{d}u/\mathrm{d}y$, decreases. The velocity gradient at the wall is directly related to the shear stress, τ_w, the fluid is exerting on the wall:

$$\tau_w = \mu \frac{\mathrm{d}u}{\mathrm{d}y} \tag{6.54}$$

where μ is the *dynamic viscosity* of the fluid. This relation was originally proposed by Isaac Newton and confirmed by experiments carried out by Poiseuille in 1849 using liquid flow in tubes. The local friction coefficient is the wall-stress non-dimensionalized by the freestream dynamic pressure according to:

$$c_f = \frac{\tau_w}{\frac{1}{2}\rho_\infty V_\infty^2} \tag{6.55}$$

Based on our observations of the velocity profiles in Fig. 6.24 and Eqs. (6.54) and (6.55), we can deduce that the local friction coefficient is highest near the leading edge and that it reduces further downstream.

To understand why the boundary layer is growing in thickness downstream we look at the time history of vorticity within the boundary layer. We know that for a given control surface, the vorticity vector ($\boldsymbol{\nabla} \times \boldsymbol{V}$) is related to the velocity around the contour of the control surface:

$$\iint_S (\boldsymbol{\nabla} \times \boldsymbol{V}) \cdot \mathbf{d}\boldsymbol{S} = \oint_C \boldsymbol{V} \cdot \mathbf{d}\boldsymbol{S} \tag{2.71}$$

The vorticity enclosed within the contour of the control surface is called the circulation, Γ:

$$\Gamma = \oint_C \boldsymbol{V} \cdot \mathbf{d}\boldsymbol{S} \tag{6.56}$$

Let us try to estimate the circulation in the boundary layer. In Fig. 6.25 we show a contour drawn about the velocity profile in the boundary layer. Due to the no-slip

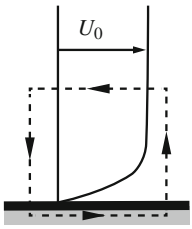

Fig. 6.25 Circulation per unit length about a contour at the upstream station

condition, the velocity at the wall is zero. Furthermore, we assume that locally the flow is aligned with the wall and that the perpendicular velocity component is therefore zero. Evaluating the circulation per unit length about this contour therefore results in:

$$\Gamma = \oint_C \boldsymbol{V} \cdot \mathbf{d}\boldsymbol{S} = 0 + 0 - U_0 + 0 = -U_0$$

We can conclude that at any station, the circulation per unit length equals $-U_0$. The vorticity is constant at any streamwise station along the plate: $-U_0$ times a unit length. The total amount of vorticity within each contour remains the same. Because the flow upstream of the plate has no vorticity, we can conclude that the vorticity is introduced at the leading edge of the plate due to the no-slip boundary condition.

Even though the circulation per unit length is constant at any streamwise station on the plate, the distribution of vorticity normal to the plate does change. Due to the viscosity of the fluid the vorticity is spread transversely as it travels downstream. In a laminar boundary layer, this goes according to the principle of molecular diffusion. The local boundary layer thickness represents the distance the vorticity has diffused away from the plate. This growing process is a function of time, t, and the diffusivity of momentum. The latter quantity is more commonly known as the *kinematic viscosity*:

$$\nu = \frac{\mu}{\rho} \tag{6.57}$$

The transverse diffusion length, δ, can be shown to correlate with $\sqrt{\nu t}$ (a derivation of this quantity is beyond the scope of this text[2]). At any distance from the leading edge, x, the time that has passed can be calculated according to $t \approx x/U_0$. Therefore, the *relative* boundary layer thickness can be expressed as:

$$\frac{\delta}{x} \propto \sqrt{\frac{\mu}{\rho U_0 x}} = \frac{1}{\sqrt{\mathrm{Re}_x}} \tag{6.58}$$

This relationship is only valid at high Reynolds numbers where $\delta/x \ll 1$ and for laminar boundary layers. We can note from (6.58) that with higher freestream velocity the boundary layer becomes thinner at any station along the plate. This is simply because the boundary layer has had less time to grow. Bodies exposed to high-

[2] The interested reader is referred to Fick's laws of diffusion [21].

Reynolds number flows therefore have a thinner boundary layer with respect to their length.

6.4.1.1 Boundary Layer Characteristics

To characterize the boundary layer, we frequently use the terms *displacement thickness*, *momentum thickness*, and *shape factor*. In the subsequent paragraphs we show how these parameters relate to the velocity distribution in the boundary layer. These properties are applicable to both laminar and turbulent boundary layers.

The displacement thickness, δ^*, is a measure of the missing mass flow due to the presence of the boundary layer.

$$\delta^* = \int_0^\delta \left(1 - \frac{\rho u}{\rho_e u_e}\right) \mathrm{d}y \tag{6.59}$$

If we assume that the flow in the boundary layer is incompressible its displacement thickness can be reduced to:

$$\delta_i^* = \int_0^\delta \left(1 - \frac{u}{u_e}\right) \mathrm{d}y \tag{6.60}$$

The incompressibility assumption is often used in practice, since it has shown to give good correlation to experimental results.

Similar to the displacement thickness we can also define a thickness that accounts for the missing momentum in the boundary layer. This thickness is termed the momentum thickness, θ, and can be found from:

$$\theta = \int_0^\delta \frac{\rho u}{\rho_e u_e}\left(1 - \frac{\rho u}{\rho u_e}\right) \mathrm{d}y \tag{6.61}$$

Again, if we assume that in the boundary layer the flow is incompressible we have:

$$\theta_i = \int_0^\delta \frac{u}{u_e}\left(1 - \frac{u}{u_e}\right) \mathrm{d}y \tag{6.62}$$

Finally, we introduce a shape factor, H, that relates the displacement thickness to the momentum thickness according to:

$$H = \frac{\delta^*}{\theta} \tag{6.63}$$

The shape factor is a function of the shape of the velocity distribution within the boundary layer, hence its name. Notional velocity profiles for both high and low shape factor are shown in Fig. 6.26. Notice that for a small H the velocity gradient at the wall is higher compared to a high H. The shape factor will prove its importance in predicting, for example, transition and separation (Sect. 6.4).

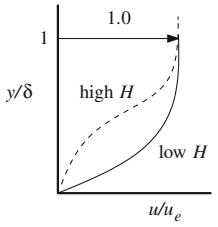

Fig. 6.26 Typical velocity profiles within the boundary layer at high and low values of H

6.4.1.2 Effect of Reynolds Number and Mach Number

Let us expand on the effect of the Reynolds number on the friction coefficient. As is evident from (6.58), the Reynolds number is responsible for the relative thickness of the boundary layer. Using Blasius' equation (which is presented in Sect. 6.5.2) we can deduce a velocity profile inside the *incompressible* laminar boundary layer. We can relate the velocity gradient at the wall to the kinematic viscosity and the freestream velocity according to:

$$\left(\frac{\partial u}{\partial y}\right)_{y=0} = 0.332\, U_0 \sqrt{\frac{U_0}{\nu x}} \tag{6.64}$$

Using this result and (6.55) we have a very straightforward quantification of the friction drag:

$$c_f = \frac{0.664\mu}{\rho U_0^2}\, U_0 \sqrt{\frac{U_0}{\nu x}} = \frac{0.664}{\sqrt{\mathrm{Re}_x}} \tag{6.65}$$

This shows us that the friction coefficient indeed decreases with increasing Reynolds number. The average friction coefficient of a complete plate can be found by integrating the local friction coefficient over the complete length of the plate:

$$C_f = \frac{1}{l} \int_0^l c_f \mathrm{d}x \tag{6.66}$$

Substituting (6.65) we find that:

$$C_f = \frac{1.328}{\sqrt{\mathrm{Re}_l}} \tag{6.67}$$

This equation demonstrates once more that an increase in the Reynolds number decreases the friction drag coefficient of a surface wetted by an airflow. If we relate that to airplanes, we can conclude from this simple derivation that both an increase in size as well as an increase in cruise velocity decreases the average friction coefficient of the aircraft. However, we must note that the effect of surface roughness has not yet been taken into account and that we solely speak of laminar boundary layers. It should also be noted that absolute *drag* does increase with velocity and size.

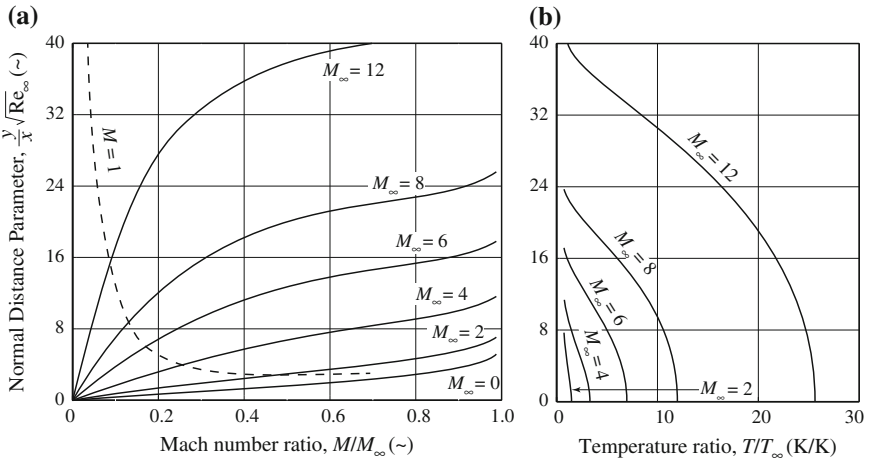

Fig. 6.27 Mach number and temperature distribution across a laminar boundary layer on an insulated flat plate for various Mach numbers. Calculations carried out by Van Driest [59] assuming $\mathrm{Pr} = 0.75$ and $S/T_w = 0.505$. **a** Mach number distribution. **b** Temperature distribution

For *compressible* flows the density is not constant and the assumption of a constant viscosity and heat transfer coefficient through the boundary-layer thickness are no longer valid. The friction between the flow and the wall generates a temperature difference between the wall and the free-stream. The resulting temperature distribution in the boundary layer has an effect on the velocity distribution and therefore on the velocity gradient at the wall. At the same time, the temperature has an effect on the viscosity through Sutherland's formula (2.81). Both effects contribute to a change in friction coefficient.

For a laminar boundary layer and adiabatic wall conditions, Van Driest [59] calculated the change in velocity profile with free-stream Mach number using *Crocco's method*.[3] Assuming adiabatic wall conditions and a constant heat transfer coefficient, the temperature and Mach number profiles within the boundary layer could be determined for various free-stream Mach numbers. The Mach number and temperature distribution is shown in Fig. 6.27.

If we examine Fig. 6.27a, we can observe that an increase in Mach number has several effects. First of all, it increases the boundary layer thickness. Secondly, the Mach number gradient at the wall decreases with Mach number. It can be shown that also the velocity profile follows this trend [59]. This results in a lower shear stress at the wall, which causes a reduction in friction coefficient with Mach number. The sonic line is also shown in Fig. 6.27a. With increasing Mach number, the sonic line moves away from the wall. However, if we compare the location of the sonic line to the thickness of the boundary layer, we conclude that the position of the sonic line only changes slightly. For example, for $M_\infty = 2$ the sonic line lies at approximately

[3] Details on Crocco's method can be found in Ref. [59].

0.40δ, where δ has been defined as the distance where $u/V_\infty = 0.995$. For $M_\infty = 8$ the sonic line is located at approximately 0.35δ.

The temperature distribution in Fig. 6.27b shows the effect of friction on the wall temperature. Note that at $M = 2$ the wall temperature is 40 % higher than the free-stream temperature. At $M = 4$ there is more than a factor of 3 between the wall temperature and the free-stream temperature. We can therefore deduce that for adiabatic conditions, the temperature increase over at high supersonic Mach numbers results in temperatures that are higher than conventional aluminum can sustain without degrading material properties. Therefore, supersonic aircraft that fly faster than $M \approx 2.5$ have to rely on more heat resistant materials, such as titanium. In the hypersonic realm ($M_\infty > 5$) the wall temperatures become extremely high, which requires aerospace vehicles that operate in this regime to have an ablative heat shield or a thermal-soak heat shield. In the transonic domain, aerodynamic heating is comparatively small and has little effect on the velocity gradient and friction coefficient. Therefore, the incompressible boundary-layer equations can often be successfully used to predict the boundary layer properties in the transonic flow domain.

Using the method of Van Driest, the compressible friction coefficient can be correlated to the incompressible friction coefficient. An approximation of the relation between compressible and incompressible friction coefficient was derived by Johnson and Rubesin [27]:

$$\frac{C_f}{C_{f_i}} = \frac{1}{\left(1 + 0.1305M^2\right)^{0.12}} \tag{6.68}$$

Both the approximation of Johnson and Rubesin as well as the calculation of Van Driest is shown in Fig. 6.28. We see a gradual decay of the friction coefficient with increasing Mach number. We also note that in the transonic flow domain the decrease in friction coefficient is relatively small. Using (6.68), a reduction of 1.5 % at $M = 1$ can be computed. The change in turbulent friction coefficient is also presented in Fig. 6.28 and is discussed in more detail in Sect. 6.4.2.

6.4.1.3 Flow Reversal in Laminar Boundary Layers

In the preceding paragraphs we have investigated the development of boundary layers over flat plates with negligible pressure gradients (i.e. $\partial p/\partial x = 0$). We now investigate how the pressure gradient affects the velocity profile in the boundary layer, the friction drag, the transition point, and the separation point.

We start our discussion with the presence of a *favorable* pressure gradient. In practice this means that the further downstream one travels, the lower is the pressure (i.e. $\partial p/\partial x < 0$). In this case, the flow outside the boundary layer accelerates continuously while the favorable pressure gradient is present. This effect is illustrated in Fig. 6.29 where we see the velocity profile of a fluid in a converging channel (two-to-one contraction ratio). The flow accelerates in the converging part of the channel such that it reaches twice its velocity in the narrower part of the channel.

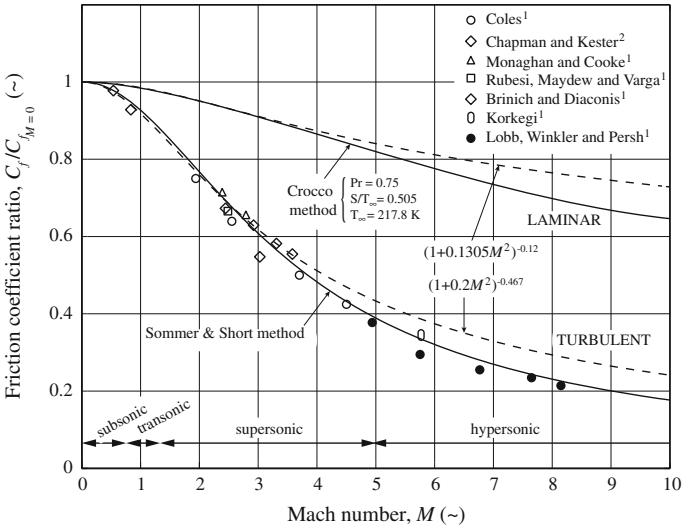

Fig. 6.28 Variation of skin friction coefficient with Mach number. Data from Refs. [25, 27, 37, 39, 46, 53, 58, 59]. 1: Mean skin friction values. 2: Local skin friction values, for Reynolds number $\mathrm{Re}_\theta = 8{,}000$ based on momentum thickness

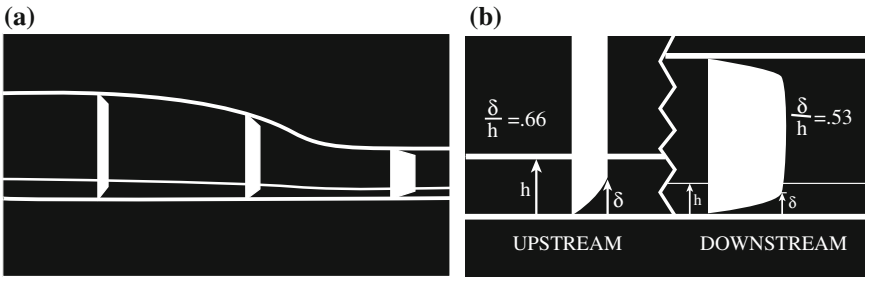

Fig. 6.29 Flow visualization of velocity profiles in a converging channel (after Ref. [1]). **a** Velocity profile in a converging channel. **b** Comparison between upstream and downstream velocity profiles

When looking at the velocity profile in the boundary layer we see that the boundary layer thickness reduces considerably. Most of this reduction can be explained by the two-to-one decrease in flow area. However, using the distance to the nearby streamline, h, as a reference dimension, we can see that also the relative thickness δ/h has decreased. If we consider the vorticity within the layer up to h we can deduce that the vorticity increases linearly with the increase in freestream velocity. This new vorticity is added to the vorticity already present in the boundary layer at the wall. It is as if a new boundary layer is being formed at every increment in the converging duct. The combined profile at the exit of the contraction is relatively thinner because the vorticity has had little time to diffuse. In the narrow part of the duct we now have a boundary layer with a larger percentage of vorticity close to the wall. This results in a higher velocity gradient, shear stress, and friction coefficient.

In a divergent channel, the opposite effect occurs. When the diffuser angle is relatively low, the flow velocity in the channel will decelerate and an *unfavorable* (or *adverse*) pressure distribution is present: $\partial p/\partial x > 0$. The pressure downstream is higher than the pressure upstream. The result is a thickening of the boundary layer both in the absolute and in the relative sense. In other words, $\partial \frac{\delta}{h}/\partial x > 0$. The reduced velocity slope at the wall reduces the shear stress and the friction coefficient. The velocity profile becomes less *full*: less vorticity is concentrated near the wall and more is concentrated near the edge of the boundary layer. This can be seen by comparing the velocity profiles at the first two stations of Fig. 6.30b.

If the deceleration of the flow continues to take place the velocity gradient ($\partial u/\partial y$) near the wall becomes smaller and smaller. Eventually the shear stress goes to zero, followed by a reversal of the flow direction near the wall. This is visualized in the 3rd station of Fig. 6.30b. We see that the flow at the second station is still directed to the right. While the flow at the third station is directed to the left. Somewhere in between those two stations the flow at the wall has come to a complete stand still. The corresponding shear stress at this point is zero. We call this point the separation point. Beyond this point, the fluid, which was in contact with the wall in the upstream boundary layer, has separated from the wall by a region of reversed (or recirculating) flow. This is visualized in Fig. 6.31.

We have now established that the development of the boundary is influenced by the pressure gradient. Given the fact that any body in a flow field generates a pressure distribution, we can deduce that the boundary layer development is influenced by the shape of the pressure distribution. In addition, the separation point (if there is any) is affected by the pressure distribution. The shape of the velocity profile at any point in the boundary layer is also dependent on the conditions of the boundary layer downstream. For the simple case of a flat plate we know that the boundary layer transitions from laminar to turbulent and subsequently grows in thickness the further we move downstream. A thicker boundary layer has a lower velocity gradient at the wall and is therefore more prone to separate whenever an adverse pressure gradient is present. If we recall the lessons we learned from Sect. 6.2 we can state that in order to prevent separation we need to modify the outer shape of the body such that the we obtain relatively small pressure (adverse) gradients in regions where the boundary layer is relatively thick.

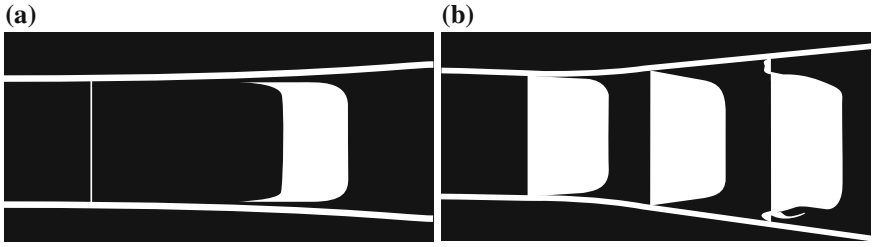

Fig. 6.30 Flow visualization of velocity profiles in a diverging channels of different diffuser angle (after Ref. [1]). **a** Diverging channel with small diffuser angle. **b** Diverging channel with larger diffuser angle

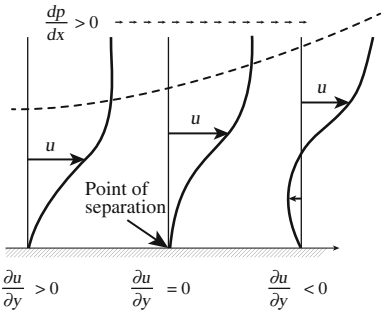

Fig. 6.31 Effect of adverse pressure gradient $\mathrm{d}p/\mathrm{d}x$ on velocity profile, $u(y)$

6.4.2 Turbulent Boundary Layer

As was demonstrated by Osbourne Reynolds in the late 19th century, fluid flow in a pipe transitions from laminar to turbulent beyond a certain *critical* Reynolds number (Fig. 6.32).[4] The same happens in boundary layers. The steps in the transition from laminar to turbulent are complicated and interdependent. First there is the growth of the nearly two-dimensional Tollmien-Schlichting waves. These waves are the first (infinitesimal) indicators of laminar-flow instabilities. Whether these instabilities grow depends on the amplification factor of the instability at a particular position in the boundary layer.

Experiments of boundary layer flow over a flat plate show that the unstable Tollmien-Schlichting waves grow downstream and become three-dimensional. At regions of high localized shear stress, several types of unstable vortices occur. These vortices are longitudinally stretched and begin a cascading breakdown into smaller units. In this fluctuating state, intense local changes occur at random locations and at random times in the shear layer near the wall. Turbulence occurs in these *spots* which further coalesce downstream into fully turbulent flow. This three-dimensional transition process is shown in Fig. 6.33 after Kegelman and Mueller [28]. Note that the turbulent spots mark wedges of turbulent flow. This results in the typical zig-zag pattern of the transition line.

Since it is generally known that laminar boundary layers have a lower friction drag than turbulent boundary layers, it is of interest to know where transition originates. As we will see more explicitly in Sect. 6.5.4, amplification or damping of Tollmien-Schlichting waves largely depends on the local pressure gradient. A negative pressure gradient reduces the amplification of disturbances, while a positive (adverse) pressure gradient increases the amplification rates. An adverse pressure gradient therefore hastens the onset of transition compared to boundary layer flow in the absence of a pressure gradient.

If the critical Reynolds number is defined as the Reynolds number for which a disturbance with a particular wave length causes an unstable growth of that particular disturbance, the minimum critical Reynolds number is the Reynolds number

[4] In this context, the word *critical* is unrelated to the flow properties at sonic conditions.

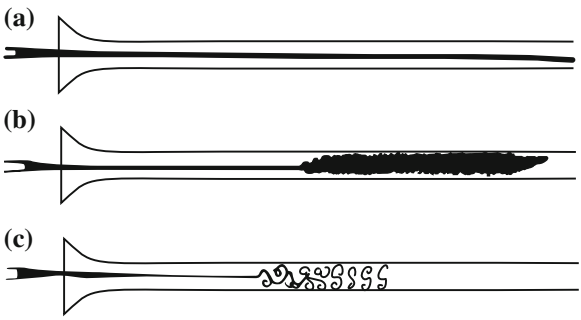

Fig. 6.32 The classical dye experiment in pipe flow as described by Reynolds in 1883 (after Ref. [45]). **a** Low speed: laminar flow, **b** high speed: turbulent flow, **c** spark photograph of condition (**b**)

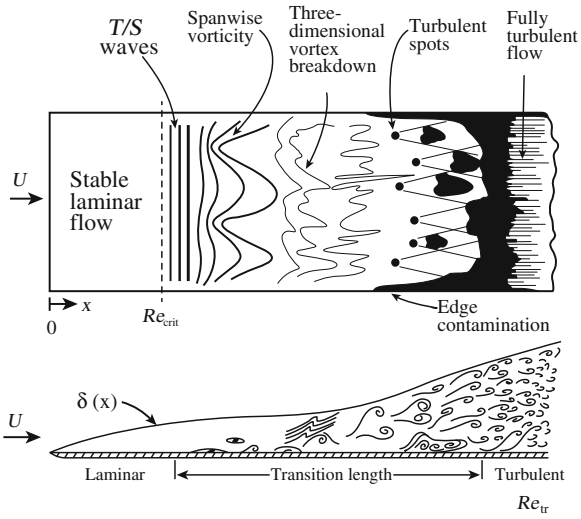

Fig. 6.33 Idealized boundary layer transition over a flat plat (after Ref. [28])

for which any disturbance of arbitrary wave length causes the boundary layer to become unstable. Based on a theoretical investigation of compressible boundary layer stability over a flat plate, Lees [35] concludes that for subsonic conditions any laminar boundary-layer flow is unstable at sufficiently high Reynolds numbers. The minimum critical Reynolds number is largely determined by the product of mean density and the mean vorticity across the boundary layer. The addition of heat to the fluid through the solid surface reduces the minimum critical Reynolds number and therefore hastens the onset of transition. Cooling the wall has the opposite effect.

For adiabatic conditions, Laufer and Vrebalovich [34] concluded that the Mach number has no effect on the stability of the laminar boundary layer but is solely dependent on the displacement-thickness Reynolds number, Re_δ. In addition, the amplification factor is also shown to be independent of the Mach number. However, it is shown that the disturbances propagate faster with increasing Mach number. Consequently, a disturbance propagating to a certain x-position will not be amplified as much in a higher Mach number flow because its time available to grow is less, even

though its amplification coefficient is the same. Therefore, the adiabatic compressible boundary layer is shown to be more stable with respect to small disturbances than the incompressible one.

Once the boundary layer has transitioned from laminar to turbulent, its velocity profile changes significantly. Whereas the laminar boundary layer showed a smoothly changing velocity profile, the large amount of vorticity in the turbulent boundary layer creates a more rugged velocity profile. In Fig. 6.34 the instantaneous velocity of a laminar and turbulent boundary layer are shown on opposite sides of a flat plate. The ruggedness of the velocity profile in the turbulent boundary layer is evident. When we superimpose a large number of these instantaneous velocity profiles over time, we can distinguish a mean velocity profile for both the turbulent and the laminar boundary layer. It can be seen from Fig. 6.34 that the deviation from the mean velocity profile is much larger in the turbulent boundary layer than it is in the laminar boundary layer, due to the randomness of the vortices that are created in the turbulent boundary layer.

In Fig. 6.35 the two velocity profiles are compared. When superimposing them we see that the turbulent boundary layer shows a larger velocity gradient at the wall. The turbulent boundary layer therefore generates more shear stress as per (6.54).The *incompressible* friction coefficient at a particular station x on a flat plate can be approximated by the "power law" [66]:

$$c_f = \frac{0.027}{\mathrm{Re}_x^{1/7}} \tag{6.69}$$

Note that this relation only holds for low subsonic conditions. For turbulent boundary layers the incompressible friction coefficient therefore decays much slower with Reynolds number: $c_f \propto \mathrm{Re}_x^{-1/7}$ while $c_f \propto \mathrm{Re}_x^{-1/2}$ for laminar boundary layers. In Fig. 6.36 the local friction coefficient is plotted for both a turbulent and a laminar boundary layer. In addition, a typical transition line is shown which shows the rapid increase in local friction coefficient when the boundary layer transitions from laminar to turbulent.

The circulation is the same in both the laminar and turbulent boundary layers. However, the distribution of circulation is different. For the turbulent boundary layer

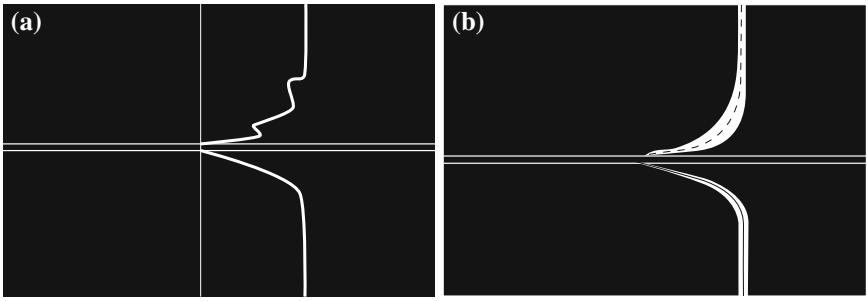

Fig. 6.34 Boundary layer around a flat plat: flow is turbulent on *upper surface* and laminar on *lower surface* (after Ref. [1]). **a** Instantaneous velocity profiles. **b** Superposition of many instantaneous velocity profiles

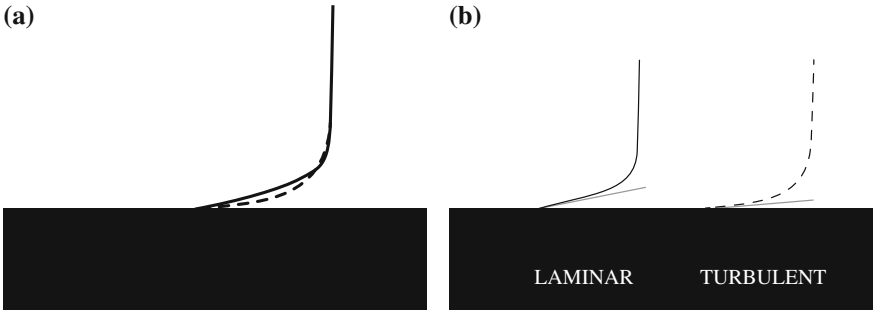

Fig. 6.35 Comparison between velocity profiles in laminar and turbulent boundary layers (after Ref. [1]). **a** Comparison of mean laminar (*solid*) and turbulent (*dashed*) velocity profiles. **b** Comparison of velocity gradients at the wall for laminar and turbulent boundary layers

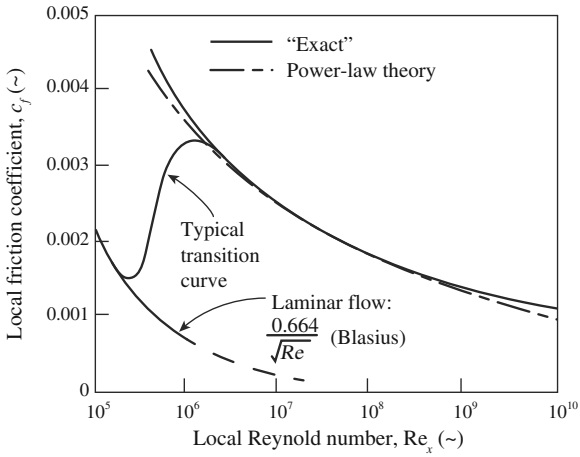

Fig. 6.36 Local coefficient, c_f, for turbulent and laminar boundary layers as a function of the local Reynolds number, Re_x

more vorticity is concentrated near the plate even though some vorticity has also spread farther from the plate. The thickness of the turbulent boundary layer on a flat plate at point x can be approximated according to [66]:

$$\frac{\delta}{x} \approx \frac{0.16}{\mathrm{Re}_x^{1/7}} \tag{6.70}$$

Comparing this to the laminar boundary layer we see that the laminar boundary layer grows according to $\delta \propto x^{1/2}$, while the turbulent boundary layer grows much faster according to $\delta \propto x^{6/7}$.

The distribution of momentum is also different between the two boundary layers. The unsteady random rotary motions associated with vorticity that is aligned with the flow transports high-momentum fluid towards the plate while low-momentum fluid is transported away from the plate. This extra momentum close to the wall enables the turbulent boundary layer to withstand much larger adverse pressure gradients

Fig. 6.37 Gloster Javelin FAW.9 with three rows of vortex generators on the wing to delay the onset of boundary layer separation. *Photo* Adrian Pingstone

before separating from the wall. This is the reason why vortex generators are often seen on airplane wings. They generate additional vorticity in the direction of the flow that transports momentum towards the wing surface and hence delays the onset of separation. Rows of vortex generators can be seen on various modern transonic airplanes. A historic example is the Gloster Javelin having three rows of vortex generators on its outer wing (Fig. 6.37).

6.4.2.1 Effect of Reynolds Number and Mach Number on Friction Drag

We have already noted that the effect of the Reynolds number on the friction coefficient is less strong in turbulent boundary layers than in laminar boundary layers. There exist many empirically derived relations that correlate the turbulent friction coefficient, C_f, of a hydraulically smooth plate to the freestream Reynolds number. Schlichting [48] proposed the following interpolation formula:

$$C_f = \frac{0.472}{(\log_{10} \mathrm{Re})^{2.58}} \tag{6.71}$$

Note that the two coefficients in (6.71) are empirically determined. Von Kármán and Schoenherr used the following equation to fit the empirical data:

$$\frac{0.242}{\sqrt{C_f \mathrm{Re}}} = \log_{10} C_f \tag{6.72}$$

Equation (6.72) needs to be solved iteratively to find a solution for C_f. Note that the Von Kármán-Schoenherr relation relies on a single empirical coefficient. In Fig. 6.38 the two relations are shown together with various experimental results. Some of the experiments date back to Froude in the late 19th century. There exists quite some scatter between the various experimental data. According to Ref. [40] the experimental data from Smith and Walker (1959) is most reliable due to the accurate measurement techniques. It can be seen from Fig. 6.38 that both theoretical lines fol-

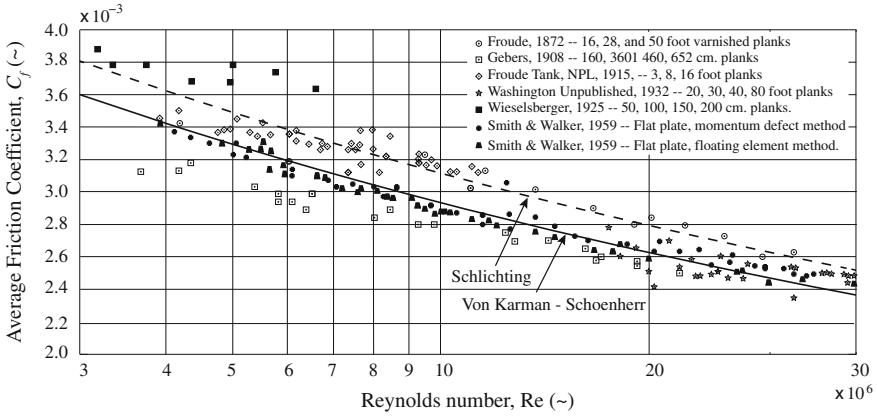

Fig. 6.38 Variation of turbulent skin friction coefficient with Reynolds number. Data selected from [40]

low approximately the same trend. It depends on the experimental data set to judge which theoretical line gives a better prediction.

It is of practical interest to investigate the effect of the Mach number on the friction coefficient of a turbulent boundary layer. We would like to know if the friction coefficient in transonic domain is influenced by the Mach number. Figure 6.28 on p. 309 shows experimental results for the compressible, turbulent friction coefficient up to a Mach number of 10. In addition, two theoretical lines are plotted, which are shortly discussed hereafter. It can be observed that the friction coefficient of the turbulent boundary layer has a much stronger dependency on the Mach number than the friction coefficient of a laminar boundary layer.

Rubesin et al. [46] base their prediction of the compressible, turbulent friction coefficient on the interpolation curve of Schlichting (6.71):

$$C_f = \frac{0.472}{(\log_{10} \mathrm{Re})^{2.58} \left(1 + \frac{\gamma-1}{2} M_\infty^2\right)^{0.467}} \tag{6.73}$$

If we compare the denominator of (6.73) to the isentropic Mach-temperature relation (2.147), we recognize the effect of the static temperature on the friction coefficient. In Fig. 6.28 this simple model is shown with a dashed line. It can be seen that up to a Mach number of about $M = 3.5$ this method gives quite a good approximation of the decrease in friction coefficient with Mach number.

Sommer and Short [53] detail a somewhat more elaborate method, referred here as the T' method. The prime superscript refers to conditions at which incompressible flow relations must be evaluated in order to represent compressible flow. The skin friction drag of a smooth flat plate and turbulent boundary layer in combination with an adiabatic boundary condition is assumed. The T' method is based on the calculation of a compressible friction coefficient, C_f, from a reference skin friction coefficient, C_f', for a selected Mach number, M_∞, Reynolds number, Re_∞ and adiabatic wall

temperature, T_w. The adiabatic wall temperature is a function of the Mach number:

$$\frac{T_w}{T_\infty} = 1 + 0.178 M_\infty^2 \tag{6.74}$$

Sommer and Short [53] obtained the following equation for T':

$$\frac{T'}{T_\infty} = 1 + 0.035 M_\infty^2 + 0.45 \left(\frac{T_w}{T_\infty} - 1 \right) \tag{6.75}$$

The Reynolds, Re', number then becomes:

$$\frac{\mathrm{Re}'}{\mathrm{Re}_\infty} = \frac{1}{\left(\frac{T'}{T_\infty}\right)\left(\frac{\mu'}{\mu_\infty}\right)} \tag{6.76}$$

where the viscosity ratio is given by the Sutherland equation (2.81). The relationship between C_f' and Re' is given by the Von Kármán-Schoenherr relation (6.72):

$$\frac{0.242}{\sqrt{C_f' \mathrm{Re}'}} = \log_{10} C_f' \tag{6.77}$$

Finally, the compressible skin friction coefficient is obtained from C_f' according to:

$$C_f = C_f' \left(\frac{T_\infty}{T'} \right) \tag{6.78}$$

If we compare the two theoretical lines we can conclude that the method of Sommer and Short is most consistent with experimental results up to $M = 10$. However, in the transonic regime equation (6.73) gives an approximation that is sufficiently accurate given the scatter in experimental results. For $M = 1$, the compressible friction coefficient is about 8 % less than its incompressible counterpart. If we compare that to the laminar boundary layer (−1.5 % at $M = 1$), we can conclude that the turbulent boundary layer is more sensitive to changes in Mach number and that the change in friction coefficient due to compressibility effects is significant in the transonic regime.

6.4.3 Shock-Wave Boundary-Layer Interaction in Transonic Flow

In a mixed subsonic and supersonic domain often normal shock waves form. On the wing surface of many high-subsonic aircraft a weak normal shock (recompression shock) terminating a supersonic region is present in the design condition. The associated pressure distribution allows for a high cruise lift coefficient and a relatively high lift-to-drag ratio. On non-lifting bodies the presence of a shock should be avoided. It produces wave drag and it can also cause separation of the boundary layer at the foot of the shock wave. Shock waves on nonlifting bodies often occur when two

components intersect (see Sect. 6.6.2). Minimizing supervelocities on these components to prevent the onset of supersonic flow and associated shock waves can be a design goal to prevent such a drag penalty.

Figure 6.39a–d show shock-boundary layer interaction in transonic speeds (from Ref. [36]). The first three flow visualizations show the effect of successively increasing flow Mach number while the boundary layer is laminar. The last figure shows shock boundary layer interaction for a turbulent boundary layer in transonic speeds. Note that the weaker shocks that are formed in lower flow Mach numbers of 0.795 and 0.843 interact with the boundary layer, but do not cause significant separation (see

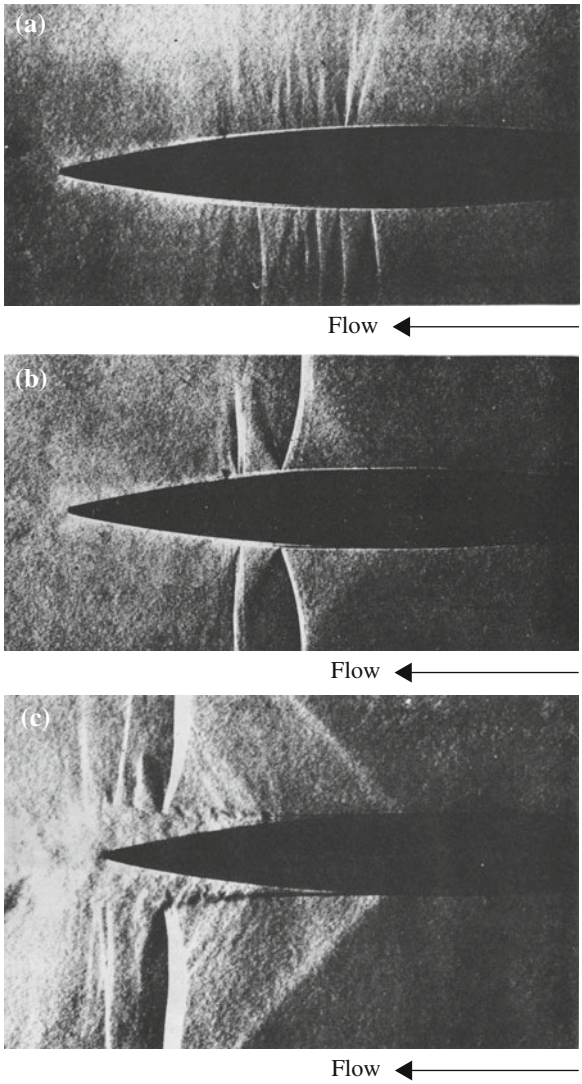

Fig. 6.39 Shock boundary-layer interaction at transonic speed for knife-edge airfoil normal to flow direction (from Ref. [36]); Reprinted with permission of the American Institute of Aeronautics and Astronautics, Inc. **a** Flow at Mach 0.795, $Re_c = 8.33 \times 10^5$ (laminar). **b** Flow at Mach 0.843, $Re_c = 8.45 \times 10^5$ (laminar). **c** Flow at Mach 0.895, $Re_c = 8.77 \times 10^5$ (laminar). **d** Flow at Mach 0.895, $Re_c = 1.75 \times 10^6$ (turbulent)

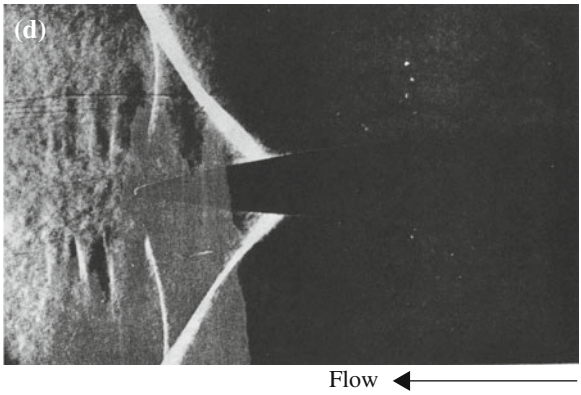

Fig. 6.39 (continued)

Fig. 6.39a, b). This is referred to as *weak interaction* of the shock with the boundary layer. For a slightly higher Mach number, namely 0.895, the shocks are strong enough to cause boundary layer separation (see Fig. 6.39c). We call this *strong interaction*. The turbulent eddies are visible at the interface of the separated shear layer and the subsequent pressure waves that emanate from the wake. The effect of boundary layer type, i.e., laminar versus turbulent, on shock-boundary layer interaction is qualitatively shown in Fig. 6.39c, d. Note that the flow Mach number is maintained between the two cases (both are at 0.895) but the Reynolds number is doubled. The laminar boundary layer shows earlier separation on the airfoil than the turbulent boundary layer case, as expected. Consequently, the wake downstream of the airfoil in the laminar boundary layer case is thicker than in the turbulent boundary layer case. We also note the lambda shock formation at the trailing edge of the airfoil in Fig. 6.39d.

6.4.3.1 Weak Interaction

Consider Fig. 6.40, which gives a general sketch of the flow field within the turbulent boundary layer and the interaction with a normal shock wave. In front of the shock wave the outer flow is supersonic. This implies that the edge velocity at the boundary layer edge is also larger than the speed of sound. Descending into the boundary layer the velocity progressively decreases up to the point where $u = a$ (i.e. $M = 1$). If we connect the points in the streamwise direction where this condition holds we form the sonic line. The location of the sonic line is determined by the boundary layer velocity profile and the edge Mach number, M_e. The velocity profile, in turn, is a function of the pressure gradient under which the boundary layer developed before encountering the interaction. Below the sonic line information can travel upstream. The pressure rise that results from the presence of the shock is spread ahead of the shock location resulting in the boundary layer thickening.

The flow field shown in Fig. 6.40 forms a complex equilibrium of flow parameters. We see that at the interaction the boundary layer becomes thicker. This implies that

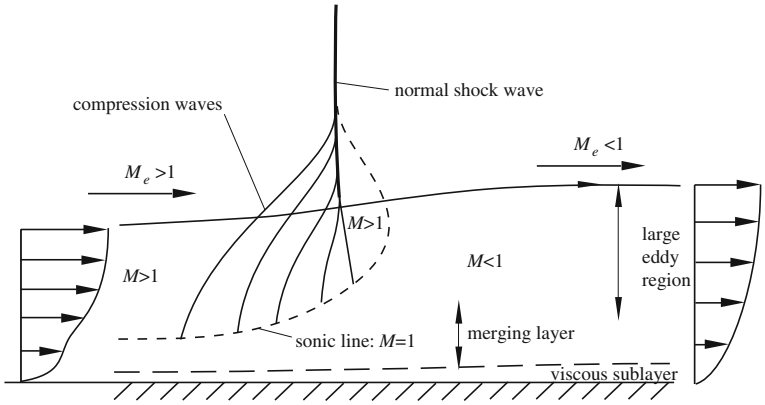

Fig. 6.40 Detail of weak shock-wave boundary-layer interaction for a turbulent boundary layer (after Ref. [41])

the streamlines move away from the wall. The resulting curvature in the streamlines causes the formation of (isentropic) compression waves. These compression waves start at the sonic line and allow the supersonic flow to change the flow direction (remember that in supersonic conditions the direction of the flow can only be altered through the formation of waves as we explained in Chap. 4). The fan of compression waves merge into a shock wave outside of the boundary layer. Close to the boundary layer edge the shock wave is still slightly oblique which reduces the flow velocity behind the shock to low supersonic. Within the boundary layer this is also the case: the flow behind the compressions waves can still be (slightly) supersonic. This gives rise to a pocket of supersonic flow behind the shock wave that is termed the *supersonic tongue*. Within the supersonic tongue the flow decelerates isentropically to subsonic speeds. The size of the supersonic tongue is case-dependent and is merely notional in Fig. 6.40.

The profile of the velocity distribution in the boundary layer is altered in the short interaction region. The outer velocity decreases substantially and the boundary layer itself thickens. This results in a higher value for the shape factor (H) and a lower velocity gradient at the wall.

The outer flow through the shock wave experiences an almost instantaneous rise in static pressure. In other words: $\mathrm{d}C_p/\mathrm{d}x \rightarrow \infty$. Based on our previous discussion on the effect of the pressure distribution on boundary layer separation we might therefore wrongfully conclude that the boundary layer would invariably separate from the surface. However, a closer look into the shock-wave boundary-layer interaction reveals that the pressure increase is smeared out over a larger streamwise region. This smearing property is due to the formation of the compression waves within the boundary layer. The effective pressure gradient within the boundary layer is therefore much smaller and merely results in an increase in shape factor and boundary layer thickness.

Finally, we note that even in the case of a weak interaction the boundary layer properties are adversely affected. Beyond the shock wave the boundary layer can

tolerate a smaller adverse pressure gradient before separating. When a convexly curved body is considered the weak shock interaction could still contribute to an early onset of trailing edge separation.

6.4.3.2 Strong Interaction

When the shock wave strength increases, the interaction between shock wave and boundary layer becomes stronger. The sonic line descends deeper into the boundary layer and a different equilibrium results. Let us try to explain this equilibrium by considering Fig. 6.41. Here we have a pocket of reversed flow (separation bubble). A separation line is present between the reversed flow and the remaining boundary layer flow. The streamlines outside of the separation bubble need to bend away from the wall. In the supersonic domain (above the sonic line) this strong curvature can only be supported by the formation of compression waves. Outside the boundary layer these compression waves merge into an oblique shock. The bending of the streamlines above the sonic line cause the boundary layer to rapidly grow in thickness. To align the streamlines with the wall a second oblique shock is present. The two oblique shocks meet at the *triple point* above the boundary layer to form a normal shock wave. This is the typical lambda shock pattern that is often seen on the upper surface of transonic wings.

Flow outside the boundary layer that goes through the two oblique shocks experiences a different deceleration than flow going through the single normal shock. A velocity difference is therefore present resulting in two velocity domains which are separated by a shear layer (known as slip line). Further downstream the velocity differences over the slip line are reduced to zero. The flow that goes through the two oblique shocks experiences less total pressure loss than the flow going through the normal shock wave. Typically the region between the triple point and the boundary layer edge is relatively small. To reduce the loss in total pressure (and the corresponding wave drag) it is therefore beneficial to smear the separation region over a

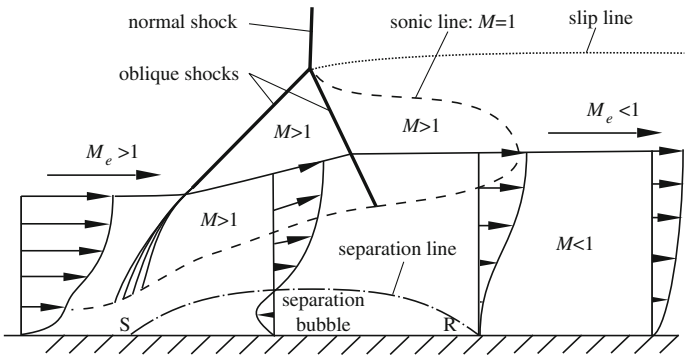

Fig. 6.41 Detail of strong shock-wave boundary-layer interaction for a turbulent boundary layer (after: [16])

larger distance such that the triple point is moved upwards and the integrated total pressure loss over the shock system decreases.

The velocity profile of the boundary layer changes substantially over this interaction. Initially, the profile shows a high pressure gradient near the wall. However, due to the large adverse pressure gradient under the oblique shock, the velocity at the wall quickly reduces to zero at point S. The flow separates and a bubble of recirculating flow forms. The boundary layer shows a negative velocity gradient at the wall. The reverse flow aids significantly in the upstream transmission of the post-shock pressure rise that causes the separation of the boundary layer in the first place. Beyond the second oblique shock the deceleration of the subsonic flow in the boundary layer causes the streamtube to expand. This aids in the reattachment of the boundary layer. At the reattachment point (R) the velocity gradient at the wall is again zero. Over the distance of the separation bubble the sonic line gradually moves away from the wall towards the boundary layer edge. Further downstream of the bubble the velocity profile has significantly thinned compared to the initial velocity distribution due to the lower edge velocity and thicker boundary layer.

The onset of separation at the foot of the shock is dependent on the development of the boundary layer in front of the shock and the surface curvature at the shock. However, for general purposes we can assume that on a flat plate separation starts at shock Mach numbers (M_e) in the range of 1.3–1.35 [5]. In many practical cases the flow behind the shock wave is further decelerated towards the trailing edge of the body. Under influence of such an adverse pressure gradient the flow might separate close to the trailing edge (trailing edge separation). Increasing the shock Mach number pushes the shock further aft. In addition, the separation bubble grows, which also moves the re-attachment point further aft. Finally, the reattached boundary layer is now more likely to separate under the adverse pressure gradient. This moves the trailing-edge separation point more forward. At some Mach number the reattachment point gets close enough to the point of trailing edge separation such that the flow does not reattach anymore. This generates a large wake that originates at the foot of the shock. This shock-induced separation is an important contributor to the exponential increase in drag (drag divergence) that occurs at the drag divergence flight Mach number.

For more information on the interaction between the normal shock and the boundary layer the reader is referred to Refs. [5, 16].

6.5 Boundary-Layer Computations

Now that we have familiarized ourselves with the qualitative aspects of boundary-layer flow, we turn to the mathematical models that describe it. In this section we present the boundary layer equations and show how they can be reduced to model the flow in laminar and turbulent boundary layers. In addition, we also present the e^N method to predict where the boundary layer transitions from laminar to turbulent.

6.5.1 Boundary Layer Equations for Steady Incompressible Flow

For a body in a high Reynolds number flow, viscous forces are dominant in essentially three domains: the boundary layer, the wake of the body, and the shock wave (if present). If the boundary layers stays attached to the airfoil, inviscid models that permit the existence of strong shocks and rotational flow (e.g. Euler equations, see Sect. 2.7.1) can be used in the region outside of the boundary layer. Prandtl's equations can be used in the laminar boundary-layer region [33]. The governing continuity, momentum and energy equations for a general unsteady, compressible, viscous flow are a set of coupled nonlinear partial differential equations, which have been presented in Sect. 2.5. If we neglect the normal stress ($\tau_{xx} = \tau_{yy} = 0$), and assume steady, incompressible, two-dimensional flow, these equations can be simplified for two-dimensional flow as follows:

continuity equation

$$\frac{\partial u}{\partial x} + \frac{\partial v}{\partial y} = 0 \tag{6.79}$$

x-momentum equation

$$\rho u \frac{\partial u}{\partial x} + \rho v \frac{\partial u}{\partial y} = -\frac{\partial p}{\partial x} + \frac{\partial}{\partial y}\left[\mu\left(\frac{\partial v}{\partial x} + \frac{\partial u}{\partial y}\right)\right] \tag{6.80a}$$

y-momentum equation

$$\rho u \frac{\partial v}{\partial x} + \rho v \frac{\partial v}{\partial y} = -\frac{\partial p}{\partial y} + \frac{\partial}{\partial x}\left[\mu\left(\frac{\partial v}{\partial x} + \frac{\partial u}{\partial y}\right)\right] \tag{6.80b}$$

energy equation

$$\rho \boldsymbol{V} \cdot \nabla\left(e + \frac{V^2}{2}\right) = k\frac{\partial^2 T}{\partial x^2} + k\frac{\partial^2 T}{\partial y^2} - \nabla \cdot p\boldsymbol{V} + \frac{\partial(u\tau_{xy})}{\partial y} + \frac{\partial(v\tau_{xy})}{\partial x} \tag{6.81}$$

We consider an incompressible boundary layer over a flat plate of length c. We make the assumption that the flow over this flat plate produces a boundary layer of thickness δ, which is much smaller than c, i.e. $\delta \ll c$. Furthermore, it is assumed that the Reynolds number of the flow is large, i.e. $1/\mathrm{Re}_\infty = O(\delta^2)$. Based on these assumptions and an order of magnitude analysis of the components in the equations above (see for example [3, 55]), the boundary layer equations can be greatly simplified:

continuity equation

$$\frac{\partial u}{\partial x} + \frac{\partial v}{\partial y} = 0 \tag{6.82}$$

x-momentum equation

$$\rho u \frac{\partial u}{\partial x} + \rho v \frac{\partial u}{\partial y} = -\frac{dp_e}{dx} + \frac{\partial}{\partial y}\left(\mu \frac{\partial u}{\partial y}\right) \tag{6.83a}$$

y-momentum equation

$$\frac{\partial p}{\partial y} = 0 \tag{6.83b}$$

energy equation

$$\rho u \frac{\partial h}{\partial x} + \rho v \frac{\partial h}{\partial y} = k \frac{\partial^2 T}{\partial y^2} + u \frac{\mathrm{d}p_e}{\mathrm{d}x} = \mu \left(\frac{\partial u}{\partial y}\right)^2 \tag{6.84}$$

Note that subscript "e" represents the conditions at the boundary-layer edge. Also note that the y-momentum equation basically states that the pressure stays constant throughout the boundary layer. The pressure is therefore solely dependent on x. Hence, from now on we replace its partial derivative operator (∂) with a total derivative operator (d).

By defining the boundary values at a solid surface, this set of equations can be seen as a boundary value problem (BVP). To assess this BVP, consider a coordinate system which is bound to a solid object, with the y-axis perpendicular to its surface and the x-axis aligned with the flow. The wall boundary values usually imply the no-slip condition:

$$u(x, 0) = 0, \quad v(x, 0) = v_0 \tag{6.85}$$

Here, v_0 is the velocity perpendicular to the wall. In most conditions $v_0 = 0$. However, in case boundary-layer suction is applied $v_0 < 0$. In addition, the temperature at the wall is defined as follows:

$$T(x, 0) = T_\mathrm{w}(x) \tag{6.86}$$

In the general case, T_w is a function of time, i.e. $T_\mathrm{w} = T_\mathrm{w}(x, t)$. In the case of adiabatic wall conditions the heat flow to the wall, q_w is zero and the following boundary condition results:

$$\left(\frac{\partial T}{\partial y}\right)_{y=0} = 0 \tag{6.87}$$

If adiabatic wall conditions exist, the adiabatic wall temperature ($T_\mathrm{w} = T_\mathrm{aw}$) is a part of the solution rather than a set boundary condition. The steady-state adiabatic wall temperature can, however, be computed by using (6.74). At the outer edge (subscript e) of the boundary layer, the following boundary conditions exist:

$$\lim_{y\to\infty} u(x, y) = u_e(x), \quad \lim_{y\to\infty} T(x, y) = T_e(x) \tag{6.88}$$

An estimate of the values of $u_e(x)$ and $T_e(x)$ can be obtained by calculating the flow around an object using for example the Euler equations. The five boundary conditions together with the coupled equations of motion [(6.82)–(6.84)] form the basis for the analysis of laminar boundary layer flow. A significant simplification with respect to the original equations of motion can be observed. It is stressed that the above equations are derived for laminar boundary layers, assuming incompressible flow and a thin boundary layer. A more complex order-of-magnitude analysis can be carried out for boundary layers which exhibit a significant thickness [48, 55]. However, this is beyond the scope of the present text.

When we integrate the boundary-layer momentum Eq. (6.83a) from $y = 0$ to $y = \delta$ and also employ (6.82) we obtain the Von Kármán momentum integral relation, (also known as the momentum integral equation):

$$\frac{\mathrm{d}\theta}{\mathrm{d}x} + (2 + H)\frac{\theta}{u_e}\frac{\mathrm{d}u_e}{\mathrm{d}x} = \frac{\tau_w}{\rho u_e^2} = \frac{c_f}{2} \tag{6.89}$$

The shock-wave-boundary-layer interactions that have been presented in Sect. 6.4.3 cannot be captured by solving the Von Kármán equation. This method only determines the effect of a velocity change on the development of the momentum thickness. However, this approach is still used in numerical codes for transonic flow about bodies. To be able to successfully apply the method described above the pressure rise over the normal shock should be smeared over a certain streamwise distance. In this manner the shock is treated as a finite adverse pressure gradient. The separation and subsequent reattachment of the boundary layer cannot be predicted with this method, which essentially limits its application to local Mach numbers below $M = 1.3$. To capture the interaction between the flow and the boundary layer we need to employ more computationally expensive tools based on (for example) the Reynolds-averaged Navier-Stokes equations (see Chap. 2).

6.5.2 Laminar Boundary Layer

The Blasius equation can be derived from the boundary layer equations. It reduces the system of equations [(6.82)–(6.84)] to a single ordinary differential equation (see Ref. [3] for complete derivation):

$$f''' + \frac{1}{2}ff'' = 0 \tag{6.90a}$$

subject to

$$f = f' = 0 \quad \text{on} \quad \eta = 0 \tag{6.90b}$$

$$f' \to 1 \quad \text{as} \quad \eta \to \infty \tag{6.90c}$$

where

$$\eta = y\sqrt{\frac{V_\infty}{\nu x}} \tag{6.90d}$$

$$f'(\eta) = \frac{u}{V_\infty} \tag{6.90e}$$

The resulting velocity gradient at the wall has been quoted in (6.64). The displacement thickness of a typical Blasius velocity profile (incompressible conditions) can be shown to be a function of the Reynolds number according to:

$$\delta^* = \frac{1.72x}{\sqrt{\mathrm{Re}_x}} \tag{6.91}$$

The momentum thickness for such a velocity profile can be shown to be

$$\theta = \frac{0.664x}{\sqrt{\mathrm{Re}_x}} \tag{6.92}$$

We note that both the momentum thickness and the displacement thickness increase proportional to $\sqrt{x}$. At the trailing edge of the plate we substitute $x = c$. If we compare the result to (6.67) we see that the momentum thickness at the trailing edge is directly related to the friction drag over the plate:

$$C_f = \frac{2\theta_{x=c}}{c} \tag{6.93}$$

This is an important result because it is not limited to laminar boundary layers or the Blasius velocity profile. It is a universal observation that holds for both turbulent and laminar boundary layers: the reduced momentum in the boundary layer at the trailing edge is a direct measure for the amount of friction drag of the profile. More general, any loss of momentum can directly be correlated to the drag of a body (see also Fig. 6.2). In this case, the momentum deficiency is caused by the friction of the body.

The Blasius solution only holds for a flat plate where the external velocity distribution is constant. To predict the boundary-layer properties in the presence of a pressure distribution, an engineering approach can be used. For example, the method of Thwaites [56] predicts these properties regardless of the exact shape of the velocity profile inside the (laminar) boundary layer. We will derive this method and show some of its properties.

Thwaites' method starts from the Von Kármán integral relation. We first multiply the momentum integral equation (6.89) by $\theta u_e/\nu$:

$$\frac{\tau_w \theta}{\mu u_e} = \frac{u_e \theta}{\nu}\frac{\mathrm{d}\theta}{\mathrm{d}x} + (2+H)\frac{\theta^2}{\nu}\frac{\mathrm{d}u_e}{\mathrm{d}x} \tag{6.94}$$

We define the pressure gradient parameter, λ, as follows:

$$\lambda = \frac{\theta^2}{\nu}\frac{\mathrm{d}u_e}{\mathrm{d}x} \tag{6.95}$$

Subsequently, we correlate the shear stress parameter $[(S(\lambda)]$ and the shape factor $[H(\lambda)]$ to λ using Thwaites empirical relations [66]:

$$S(\lambda) = \frac{\tau_w \theta}{\mu u_e} \approx (\lambda + 0.09)^{0.62} \tag{6.96}$$

$$H(\lambda) \approx 2.0 + 4.14z - 83.5z^2 + 854z^3 - 3337z^4 + 4576z^5 \tag{6.97}$$

with $z = (0.25 - \lambda)$. Note that when $S \to 0$ the shear stress goes to zero. In other words, the boundary layer separates when $\lambda < -0.09$. Substituting (6.95) and (6.96) in (6.94) reduces it to:

$$u_e \frac{\mathrm{d}}{\mathrm{d}x}\left(\lambda \frac{\mathrm{d}x}{\mathrm{d}u_e}\right) = 2\left[S - (2 + H)\lambda\right] = F(\lambda) \tag{6.98}$$

Thwaites shows that $F(\lambda) = 0.45 - 6\lambda$. We can therefore rewrite (6.98) to the following differential equation [employing (6.95)]:

$$u_e \frac{\mathrm{d}}{\mathrm{d}x}\left(\frac{\theta^2}{\nu}\right) + 6\left(\frac{\theta^2}{\nu}\right)\frac{\mathrm{d}u_e}{\mathrm{d}x} = 0.45 \tag{6.99}$$

Both terms on the LHS can be grouped in a single differential term:

$$\frac{1}{u_e^5}\frac{\mathrm{d}}{\mathrm{d}x}\left(\frac{\theta^2}{\nu}u_e^6\right) = 0.45 \tag{6.100}$$

Integrating this differential equation and assuming that the integration constant is zero results in the following relation between boundary-layer edge velocity and momentum thickness:

$$\theta = \sqrt{\frac{0.45\nu}{u_e^6}\int_0^x u_e^5 \mathrm{d}x} \tag{6.101}$$

Now, let us put this engineering method of Thwaites in practical perspective. We start the calculation process with a velocity distribution, $u_e(x)$ about a surface. If we consider the flow about a body we obtain such a velocity distribution from solving the Euler equations or potential flow equations. Subsequently we employ (6.101) to calculate the momentum thickness at any point on the body. In addition, we use (6.95) to obtain a value for the correlation parameter λ. Using (6.96) and (6.97) we can calculate the shear stress parameter and shape factor, respectively. These can be

used to obtain estimates of the displacement thickness and shear stress at any point on the body. By doing a number of iterations of inviscid and displacement-thickness calculations, a converged value of the displacement thickness results. It can be shown that the displacement thickness is about 1/3 of the boundary layer thickness [48]. The following example illustrates this process.

Example 6.3 Consider a plate with chord length of $c = 1\,\text{m}$, which is exposed to a flow with $V_\infty = 100\,\text{m/s}$ at 0 m ISA conditions. Consider the following velocity distribution at the edge of a boundary layer:

$$u_e = V_\infty \left(1 - \frac{x}{c}\right) \tag{6.102}$$

Calculate:

(a) The chordwise position of separation, $x_{\text{separation}}$.
(b) The friction coefficient, c_f between $x = 0$ and $x_{\text{separation}}$.

Solution:

(a) The analytic nature of the velocity distribution allows us to compute θ from (6.101):

$$\theta = \sqrt{\frac{0.45\nu}{V_\infty^6 \left(1 - \frac{x}{c}\right)^6} \int_0^x V_\infty^5 \left(1 - \frac{x}{c}\right)^5 \mathrm{d}x} = \sqrt{0.075 \frac{\nu c}{V_\infty} \left[\left(1 - \frac{x}{c}\right)^{-6} - 1\right]}$$

Knowing that $\mathrm{d}u_e/\mathrm{d}x = -V_\infty/c$, we can calculate λ using (6.95):

$$\lambda = -0.075 \left[\left(1 - \frac{x}{c}\right)^{-6} - 1\right]$$

We know that separation occurs when $\lambda = -0.09$, we can therefore calculate that:

$$\left(\frac{x}{c}\right)_{\text{separation}} = 0.123$$

(b) First, we calculate θ at discrete x positions using (6.101). Subsequently, we employ (6.95) to calculate λ at each position. The kinematic viscosity at 0 m ISA is $\nu = \mu/\rho = 18.27 \times 10^{-6}\,[\text{Ns/m}^2]/1.225\,[\text{kg/m}^3] = 14.91 \times 10^{-6}\,[\text{m}^2/\text{s}]$ and the velocity gradient is $-100\,[1/\text{s}]$. Then, we use (6.96) to compute the stress parameter (S) at each position and deduce the shear stress, τ_w. Finally we use the relation between shear stress and friction coefficient (6.55) to compute the friction coefficient at each x-position. The results are tabulated in Table 6.1 with intervals of 10 mm up to the separation point.

In the preceding example, we have demonstrated how Thwaites' method can be employed to calculate the friction coefficient distribution under a predefined velocity distribution. Thwaites' method can only be applied to the properties of a laminar boundary layer prior to separation. Because the momentum thickness at $x = 0$ is zero, the local friction coefficient tends to infinity if (6.96) is used to compute τ_w. Even though this is not physically accurate, Thwaites' method provides a fairly good estimate of the laminar boundary-layer development between $0 < x < x_{\text{separation}}$. It is very well possible that in reality the boundary layer transitions from turbulent to laminar before $x_{\text{separation}}$. This is not predicted by Thwaites' method. If the transition point is known, the boundary-layer properties should be calculated up to the transition point.

6.5.3 Turbulent Boundary Layer

The turbulent boundary layer differs substantially from the laminar boundary layer. Let us first examine which layers we can distinguish within the turbulent boundary layer. Four layers can be identified: a viscous sublayer that touches the wall (denoted with subscript w), a merging layer, a large-eddy region, and a viscous superlayer. To represent the velocity distribution in each of these layers we need to introduce a new variable: u_τ, the wall friction velocity (see Problem 6.19):

$$u_\tau = \sqrt{\frac{\tau_w}{\rho}} \tag{6.103}$$

We nondimensionalize the velocity in the boundary layer and the boundary layer thickness by introducing two additional new variables:

$$u^+ = \frac{u}{u_\tau} \tag{6.104}$$

$$y^+ = y\frac{\sqrt{|\tau_w|/\rho_w}}{\nu_w} = \frac{yu_\tau}{\nu} \tag{6.105}$$

where ν is the kinematic viscosity of the fluid ($\nu = \mu/\rho$).

The viscous sublayer (also called *laminar sublayer*) is a thin laminar layer between the wall and the turbulent flow in the boundary layer. In this layer the turbulence is damped out and the boundary layer is dominated by viscous shear flow. This layer allows for the no-slip condition of the turbulent boundary layer. The thickness of this layer can be as small as $\delta_v = 1/500$th of the boundary layer thickness, depending on the velocity profile in the boundary layer, the viscosity of the flow, and the density [66]. The velocity profile in this part of the boundary layer has been shown to match closely to the following relation:

Table 6.1 Table belonging to Example 6.3

x	mm	0	10	20	30	40	50	60	70	80	90	100	110	120
θ	mm	0	0.026	0.038	0.047	0.056	0.064	0.071	0.078	0.085	0.092	0.099	0.106	0.114
λ	(~)	−0.0000	−0.0047	−0.0097	−0.0151	−0.0209	−0.0271	−0.0338	−0.0410	−0.0488	−0.0571	−0.0662	−0.0760	−0.0866
S	(~)	0.22	0.22	0.21	0.20	0.19	0.18	0.17	0.15	0.14	0.12	0.10	0.07	0.03
τ_w	N/m^2	∞	14.84	9.85	7.49	6.00	4.92	4.06	3.35	2.73	2.17	1.63	1.08	0.42
$c_f \times 10^3$	(~)	∞	2.42	1.61	1.22	0.98	0.80	0.66	0.55	0.45	0.35	0.27	0.18	0.07

$$u^+ = y^+ \quad y^+ < 5 \tag{6.106}$$

The velocity in the merging layer (sometimes called "overlap" layer or "blending" layer) between the laminar sublayer and the large-eddy region can be predicted using a formula provided by Spalding [54]:

$$y^+ = u^+ + e^{-\kappa B}\left[e^{\kappa u^+} - 1 - \kappa u^+ - \frac{(\kappa u^+)^2}{2} - \frac{(\kappa u^+)^3}{6}\right] \quad y^+ < 100 \tag{6.107}$$

From experiments, the Von Kármán constant is found to be $\kappa = 0.41$ and $B = 5.0$ for a smooth wall. This equation is termed the *law of the wall*.

In the large-eddy region the velocity changes logarithmically with distance from the wall. The following approximation by Coles and Hirst [12] is often used:

$$u^+ = \frac{1}{\kappa}\ln y^+ + B \quad \text{with} \quad \kappa = 0.41 \quad \text{and} \quad B = 5.0 \quad y^+ > 30 \tag{6.108}$$

The logarithmic region in the boundary layer extends to 10–20 % of the total boundary layer thickness, depending on the value of Re_δ. In the "wake" component of the boundary layer, the local pressure distribution has a significant effect on the velocity distribution. Therefore, Coles [11] proposed to add an additional quantity, Π, to account for the local pressure distribution. The resulting *law of the wake* is written as follows:

$$u^+ \approx \frac{1}{\kappa}\ln y^+ + B + \frac{2\Pi}{\kappa} f\left(\frac{y}{\delta}\right) \qquad y^+ > 30 \tag{6.109}$$

It was shown that Coles' wake parameter, Π, could be related to the displacement thickness of the boundary layer by integrating (6.109) over the boundary layer thickness:

$$\frac{\delta^*}{\delta} \approx \frac{1+\Pi}{\kappa\lambda} \quad \text{with} \quad \lambda = \sqrt{\frac{2}{c_f}} \tag{6.110}$$

The value of λ is a measure for the local skin friction coefficient and is useful in the analyses which follow. Note that this λ is not the same as the λ we used in the analysis of the laminar boundary layer with Thwaites method (Sect. 6.5.2). Finally, the wake function $f(y/\delta)$ is of the form [11]:

$$f\left(\frac{y}{\delta}\right) = \sin^2\frac{\pi y}{2\delta} \tag{6.111}$$

This implies that the wake function is zero at the wall and unity at the edge of the boundary layer. This function allows for the S-shape we expect to see in the velocity profile in the wake of the boundary layer whenever there is a pressure gradient present (see Sect. 6.4). At the edge of the boundary layer, we can now relate the edge velocity

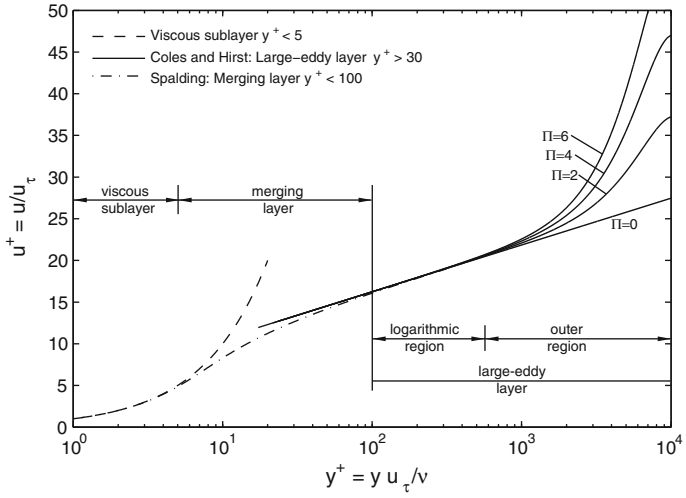

Fig. 6.42 Velocity distribution in a turbulent boundary layer for various values of Π, assuming $\delta^+ = 10{,}000$

to the velocity profile according to:

$$u^+(y=\delta) = \frac{u_e}{u_\tau} = \frac{1}{\kappa}\ln\frac{\mathrm{Re}_\delta}{\lambda} + B + \frac{2\Pi}{\kappa} \tag{6.112}$$

The velocity distributions as presented in this section are summarized in Fig. 6.42 for various values of Π. If we connect the prediction of Spalding to that of Coles and Hirst, we observe the typical S-shape in the velocity profile of the boundary layer flow.

6.5.3.1 Turbulent Boundary Layer Development

The effect of the pressure distribution on the development of the turbulent boundary layer has been demonstrated qualitatively in Fig. 6.42. We see that for various values of Π the velocity profile in the outer region can change significantly. We would like to know how the value of Π is related to the pressure distribution outside of the boundary layer. Therefore we return to the momentum integral equation as derived by Von Kármán [62]:

$$\frac{\mathrm{d}\theta}{\mathrm{d}x} + (2+H)\frac{\theta}{u_e}\frac{\mathrm{d}u_e}{\mathrm{d}x} = \frac{\tau_w}{\rho u_e^2} = \frac{c_f}{2} \tag{6.89}$$

In order to use this equation we assume that an outer velocity distribution is known and that we need to obtain values for c_f, θ, and H. In order to do so we require at least two additional equations. One is given by Coles' wall-wake law: (6.112). Based

on this relation the following algebraic equation due to Felsch et al. [19] describes the relation between H, Re_θ and c_f:

$$c_f = 0.058\mathrm{Re}_\theta^{-0.268}(0.93 - 1.95\log_{10} H)^{1.705} \tag{6.113}$$

The third relation stems from a large body of experimental research where Π is correlated to *Clauser's equilibrium parameter* β which is defined as follows [10]:

$$\beta = \frac{\delta^*}{\tau_w}\frac{\mathrm{d}p_e}{\mathrm{d}x} = -\lambda^2 H\frac{\theta}{u_e}\frac{\mathrm{d}u_e}{\mathrm{d}x} \tag{6.114}$$

where $\mathrm{d}p_e/\mathrm{d}x$ is the pressure gradient at the edge of the boundary layer and λ is as in (6.110). Clauser's equilibrium parameter is directly related to the pressure gradient. Whenever $\beta < 0$ we have a favorable pressure gradient ($\mathrm{d}p_e/\mathrm{d}x < 0$). Vice versa, when $\beta > 0$ we have an adverse pressure distribution ($\mathrm{d}p_e/\mathrm{d}x > 0$). The proposed correlation between Π and β stems from Ref. [15]:

$$\beta = -0.4 + 0.76\Pi + 0.42\Pi^2 \tag{6.115}$$

The additional variables (Π, and β) need to be correlated to H, c_f, and θ. We need two additional equations to do so. One is the definition of β, (6.114). The final equation can be obtained from Coles' wall-wake equation (6.112). The derivation of this relation is beyond the scope of this text but can be found in Ref. [66]. We merely present the reader with the result:

$$\lambda = \frac{H}{H-1}\frac{2 + 3.2\Pi + 1.5\Pi^2}{\kappa(1+\Pi)} \tag{6.116}$$

Let us review this method and put this in a practical perspective. We would like to calculate the properties of the boundary layer at various stations along a plate under the presence of a pressure distribution. To that extent we intend to solve the ordinary differential equation (6.89) with known boundary conditions. These boundary conditions could for example stem from an assumed value of the momentum thickness or Reynolds number at $x = 0$. Subsequently, we use the algebraic equations (6.113)–(6.116) to close the problem.

Example 6.4 Assume we have a pressure distribution over a curved plate of unit length that can be represented by the following polynomial:

$$C_p = bx(ax - 1)$$

where a and b are coefficients. Let us further assume that the boundary layer over the curved plate is made fully turbulent at $x = 0$ and that the initial Reynolds number based on momentum thickness, $\mathrm{Re}_\theta = 100$. Furthermore, the freestream velocity is $V_\infty = 50\,\mathrm{m/s}$ and 0 m ISA conditions apply. Consider the following cases:

1. $a = \frac{1}{2}$ and $b = 1$
2. $a = 1$ and $b = \frac{1}{2}$
3. $a = 2$ and $b = 2$

For these three cases perform the following tasks:

(a) Plot the pressure distribution, velocity distribution and distribution of the velocity gradient for each of the aforementioned cases.
(b) Plot the distribution of the following boundary layer parameters for the three aforementioned cases: H, β, Π, c_f, θ, and δ^*.
(c) Briefly reflect on the results that have been plotted.

Solution:

(a) First we employ (6.11) to rewrite the equation of C_p for u_e:

$$u_e = V_\infty \sqrt{1 + bx(1 - ax)}$$

Subsequently we take the derivative of u_e with respect to x to find $\mathrm{d}u_e/\mathrm{d}x$:

$$\frac{\mathrm{d}u_e}{\mathrm{d}x} = \frac{V_\infty}{2} \frac{b(1 - 2ax)}{\sqrt{1 + bx(1 - ax)}}$$

We substitute each combination of a and b in the above equations and plot the results in Fig. 6.43. A quick evaluation of these three graphs shows us that for case 1 we have a completely favorable velocity gradient. For cases 2 and 3 we have a velocity gradient that is favorable until $x = 0.5$. Beyond this point the pressure gradient is negative, which implies that the outer flow is decelerated. This effect is four times larger for case 3 than four case 2.

(b) To answer the second part of the question we must solve the first order differential equation (6.89). We rewrite (6.89) according to:

$$F = \frac{\mathrm{d}\theta}{\mathrm{d}x} = \frac{c_f}{2} - (2 + H)\frac{\theta}{u_e}\frac{\mathrm{d}u_e}{\mathrm{d}x} = \frac{c_f}{2} - (2 + H)\frac{\theta b}{2}\frac{1 - 2ax}{1 + bx(1 - ax)} \quad (6.117)$$

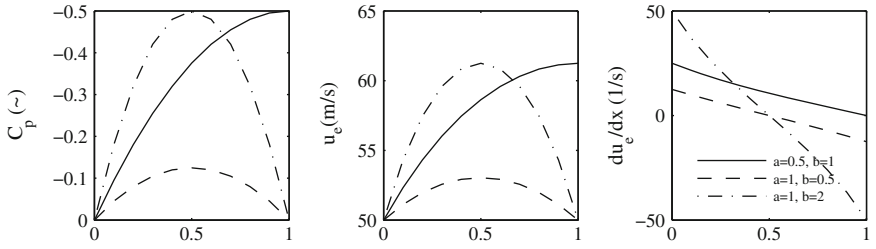

Fig. 6.43 Distribution of pressure coefficient, velocity and velocity gradient

We employ the Runge-Kutta[5] method to solve for θ. The Runge-Kutta method is a multi-step method where we first calculate intermediate constants k_1 through k_4:

$$k_1 = F(x_n,\ \theta_n)\Delta x$$

$$k_2 = F(x_n + \frac{1}{2}\Delta x,\ \theta_n + \frac{k_1}{2})\Delta x$$

$$k_3 = F(x_n + \frac{1}{2}\Delta x,\ \theta_n + \frac{k_2}{2})\Delta x$$

$$k_4 = F(x_n + \Delta x,\ \theta_n + k_3)\Delta x$$

$$\theta_{n+1} = \theta_n + \frac{1}{6}(k_1 + 2k_2 + 2k_3 + k_4)$$

In this method we march from position x_n to position x_{n+1} with steps of Δx. At each position we calculate the value of θ. To start this iteration we need a starting value for θ. We compute this through the value of Re_θ in combination with the 0 m ISA properties and the value of u_e at $x = 0$. For all three cases $u_e = V_\infty$ at $x = 0$. We have:

$$\theta_1 = \frac{\mathrm{Re}_\theta \mu}{\rho V_\infty} = 29\,\mu\mathrm{m}$$

In order to do determine the values of H at each position we need to solve the four algebraic equations (6.113)–(6.116) simultaneously. If we substitute (6.114) in (6.115) we are left with three equations that are written in the following functional format:

$$G(1) = 0.058\left(\frac{u_e\theta}{\nu}\right)^{-0.268}(0.93 - 1.95\log_{10} H)^{1.705} - c_f = 0$$

$$G(2) = -0.4 + 0.76\Pi + 0.42\Pi^2 + \frac{2}{c_f}H\frac{\theta}{u_e}\frac{\mathrm{d}u_e}{\mathrm{d}x} = 0$$

$$G(3) = \frac{H}{H-1}\frac{2 + 3.179\Pi + 1.5\Pi^2}{\kappa(1+\Pi)} - \sqrt{\frac{2}{c_f}} = 0$$

Notice that we have three equations with three unknowns: H, c_f, and Π. The Matlab routine "fsolve" is used to compute the roots of this system of equations. Having computed H and c_f we can now evaluate the RHS of (6.117) and compute θ_{n+1}. Finally, we use this new value of θ in combination with H to compute

[5] For details on the Runge-Kutta method the reader is directed to an introductory text on numerical methods for differential equations, which is also covered in Ref. [30].

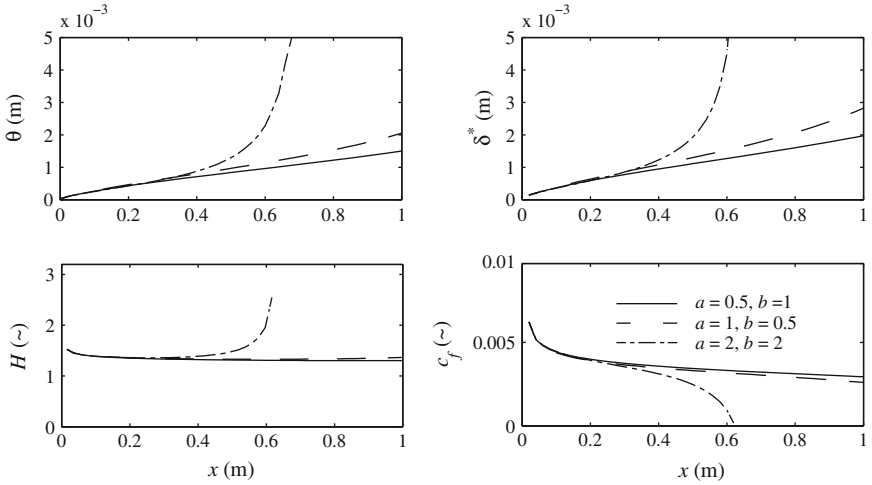

Fig. 6.44 Distribution of boundary layer parameters according to three different pressure distributions

δ^* via (6.63). We repeat this procedure at every x_n until $x_n = 1$. In Fig. 6.44 the results are plotted for the three cases.

(c) If we look at case 1, a favorable pressure gradient is present. This favorable pressure gradient results in an almost constant value of the shape factor. If we compare this to the second case we see the effect of the adverse pressure gradient on the momentum thickness and displacement thickness. We also see that the friction coefficient becomes smaller due to a slightly higher value of the shape factor. Remember that this corresponds to a lower velocity gradient at the wall (see also Fig. 6.26). Finally, we have case 3 where the shape factor rises much quicker due to the larger adverse pressure gradient. If we examine the friction coefficient we see that it tends towards zero around $x = 0.62$. We know that this is the condition of separation. In this example the flow separates from the surface. We see an exponential increase in θ and δ^* and we notice that H goes to a value close to 3.0. Beyond $x = 0.62$ the calculation of the roots of the functions G gives a complex solution and is therefore neglected in the generation of these plots.

6.5.3.2 Effect of Roughness

If we consider real airplanes, we know that the surface of the airplane is covered with various imperfections ranging from small rivet heads to larger antennas. To represent these imperfections, for every airplane an equivalent sand grain roughness can be defined. To predict the total friction drag of the airplane, the skin is assumed to be covered with this uniform sand grain roughness instead of the real excrescences. The

parameter that determines the significance of the roughness is the ratio between the sand grain height (k) and the boundary-layer thickness. We distinguish two cases:

1. Hydraulically smooth surface. If k is smaller than the height of the viscous sublayer, i.e. $k < \delta_v$, k does not affect the boundary layer significantly. In other words: the friction coefficient is unaffected by the presence of roughness. We can imagine each sand grain to be a bluff body that is immersed in a very low Reynolds-number flow. In such flow (see Fig. 6.22a) the streamlines are attached over the complete body. The drag that results in this flow (*Stokes flow*) is due to friction and therefore has the same dependency on Reynolds number as a perfectly smooth surface.
2. Hydraulically rough surface. If k is larger than the height of the viscous sublayer, i.e. $k > \delta_v$, the sand grains create small wakes behind them due to flow 'separation.' The pressure drag that is generated at each sand grain results in the *approximate* friction drag. Because the pressure drag is less dependent on the Reynolds number than the friction drag, the friction coefficient over a rough surface also has much lower dependency on the Reynolds number. The value of the friction coefficient is dominated by the relative size of the sand grains with respect to the boundary layer thickness: k/δ.

If we assume the sand grains to have an average height of $y = k$, we can introduce a nondimensional sand grain height according to (6.105):

$$k^+ = \frac{k u_\tau}{\nu} \tag{6.118}$$

From experiments (e.g. Clauser [10]) it is known that the layer where velocity changes logarithmically with wall distance still exists when roughness is present. However, the intercept of the logarithmic curve moves downward with progressively larger values of k^+. This alters (6.108) as follows:

$$u^+ = \frac{1}{\kappa} \ln y^+ + B - \Delta B(k^+) \tag{6.119}$$

For sand grains ΔB changes logarithmically with k^+ according to the classical Prandtl-Schlichting relation for $k^+ > 60$:

$$\Delta B_{\text{sand grains}} \approx \frac{1}{\kappa} \ln(1 + 0.3k^+) \quad \text{for} \quad k^+ > 60 \tag{6.120}$$

The result is the following expression for the nondimensional velocity profile in a boundary layer that is disturbed by roughness:

$$u^+ = \frac{1}{\kappa} \ln y^+ + B - \frac{1}{\kappa} \ln(1 + 0.3k^+) \tag{6.121}$$

From the experiments it is know that for values below $k^+ < 4$ roughness has no effect on the velocity profile in the boundary layer. Between $4 < k^+ < 60$ there is a transitional roughness regime. Finally, above $k^+ > 60$ the flow has become hydraulically rough. Based on (6.121) it can be shown that as the sand grains become larger, the effect of viscosity becomes negligible and the friction coefficient therefore becomes independent of the Reynolds number (see Problem 6.23):

$$u^+ = \frac{1}{\kappa} \ln\left(\frac{y}{k}\right) + 7.9 \tag{6.122}$$

We can insert (6.121) into (6.83a) under the assumption of an absent pressure gradient. Integrating the result over the thickness of the boundary layer and the length, x, results in a relation between the friction coefficient, c_f, the Reynolds number, Re_x and the grain size, k [66]:

$$\mathrm{Re}_x = 1.73(1 + 0.3k^+)e^Z \left[Z^2 - 4Z + 6 - \frac{0.3k^+}{1 + 0.3k^+}(Z - 1) \right] \tag{6.123}$$

where $Z = \kappa\lambda$. This relation, even though it is implicit, is valid for uniform sand-grain roughness over the complete range of hydraulically smooth, transitional, and fully rough walls in turbulent flat plate flow. If we write $k^+ = ku_\tau\nu = \frac{\mathrm{Re}_x(k/x)}{\lambda}$, we can plot the local friction coefficient as a function of the local Reynolds number for various values of x/k. This is shown in Fig. 6.45. The effect of the roughness is evident from this figure. The larger the grains compared to the length x the higher the friction coefficient. In addition, we see that the friction coefficient of a smooth plate decays with Reynolds number (as expected). However, we also see that the decaying effect of the Reynolds number diminishes for roughened plates above a certain Reynolds number. The smaller the sand grains compared to the size of the distance x, the larger the Reynolds number at which the Reynolds number ceases to decrease the friction coefficient. This Reynolds number is called the *cut-off* Reynolds number. This is in

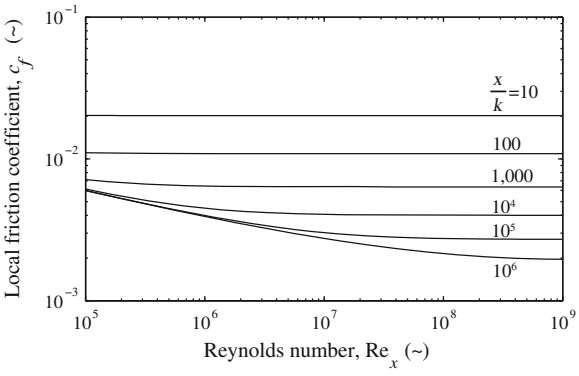

Fig. 6.45 Local skin friction on a flat plate from (6.123) for constant values of x/k

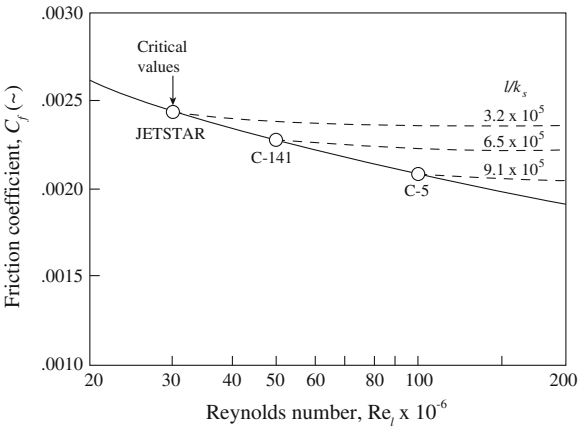

Fig. 6.46 Effect of cut-off Reynolds number on friction drag of three airplanes of the same generation and manufacturer but different size (after Ref. [38])

good agreement with classical experiments carried out by Nikuradse on pipe flow with roughened walls [42].

The results plotted in Fig. 6.45 can be directly translated to the friction drag coefficient of full scale aircraft and wind tunnel models. In Fig. 6.46 the variation in friction coefficient with Reynolds number is shown for three airplanes of the same generation and built by the same company (Lockheed). It could be assumed that the manufacturing techniques for all three airplanes was of the same level leading to identical values for the equivalent sand grain roughness of the skin of the airplane. What is shown is the relative sand grain height, scaled with respect to a characteristic length, l, of the airplane. Similar to the theoretical curves in Fig. 6.45, the largest airplane (C-5) demonstrates to have the largest cut-off Reynolds number ($\approx$100 million). This advocates the statement that large aircraft benefit from their size when it comes to the friction drag coefficient.

Example 6.5 Assume we have a flat plate with an equivalent sand grain roughness of 0.010 mm. Calculate using (6.123) the friction coefficient (c_f) at $x = 2.5$ m. Assume that we have 0 m ISA conditions and a freestream velocity of 100 m/s. Also calculate the wall stress, τ_w and the velocity gradient at the wall, $(\partial u/\partial y)_w$.

Solution:

We first calculate the Reynolds number at $x = 2.5$ m:

$$\mathrm{Re}_{x=2.5} = \frac{\rho V x}{\mu} = \frac{1.225 \cdot 100 \cdot 2.5}{17.89 \cdot 10^{-6}} = 17.1 \times 10^6.$$

Secondly, we calculate the relative grain size:

$$\frac{k}{x} = \frac{0.010 \times 10^{-3}}{2.5} = 2.5 \times 10^5$$

Because (6.123) cannot be solved directly, we use a "for" loop in Matlab according to the following routine. We first establish a set of possible values for λ. Subsequently, for each value of λ we calculate the value for k^+, Z, and Re_x:

```
for
```
$\lambda = [1, 1.001, 1.002, \ldots, 50]$
```
do
```
$$k^+ = \frac{\mathrm{Re}_x(k/x)}{\lambda}$$

$$Z = \kappa\lambda$$

$$\mathrm{Re}_x = 1.73(1 + 0.3k^+)e^Z \left[Z^2 - 4Z + 6 - \frac{0.3k^+}{1 + 0.3k^+}(Z - 1) \right]$$

```
end
```

Finally, we compare the outcome of Re_x to the value that we computed above:

$$\Delta\mathrm{Re}_x = |\mathrm{Re}_{x=2.5} - \mathrm{Re}_x|$$

We subsequently find one value of λ for which $\Delta\mathrm{Re}_x$ is closest to zero. This results in $\lambda = 26.3$. Substituting this in (6.110) results in:

$$c_f = \frac{2}{\lambda^2} = 0.00290$$

From the friction coefficient we can calculate the local shear stress according to (6.55):

$$\tau_w = c_f \frac{1}{2}\rho U_0^2 = 0.00290 \cdot \frac{1}{2} \cdot 1.225 \cdot 100^2 = 17.7\,\mathrm{N/m^2}$$

The local velocity gradient can be found by employing (6.54):

$$\left(\frac{\partial u}{\partial y}\right)_w = \frac{\tau_w}{\mu} = 0.994 \frac{\mathrm{m/s}}{\mu\mathrm{m}}$$

Example 6.6 Considering the same roughened plate as in Example 6.5, calculate the value of the total friction coefficient over the entire plate. Assume the plate has a length of $l = 3\,\mathrm{m}$ and that the boundary becomes turbulent at $x = 0.10\,\mathrm{m}$. Ignore the contribution of the laminar boundary layer over the first 10 cm to the friction coefficient.

Solution:

The friction coefficient of the plate is given by (6.66) with the upper bound $x = 3$ and the lower bound $x = 0.10$. We evaluate this integral numerically by dividing the plate

into 29 sections of $\Delta x = 0.1$ m. On each section we evaluate the friction coefficient at the beginning of the interval and at the end of the interval by employing the method of Example 6.5. We approximate the integral over each section by employing the trapezoid rule:

$$C_{f_j} = \int_x^{x+\Delta x} c_f(x)\mathrm{d}x = \left[c_f(x) + c_f(x+\Delta x)\right]\frac{\Delta x}{2}$$

The total friction drag over the plate is the sum of the incremental contributions:

$$C_f = \frac{1}{l}\sum_{j=1}^{29} C_{f_j} = 0.0030$$

6.5.4 Boundary Layer Transition

From an operational perspective, there has been a long desire to minimize the drag of an airplane to a minimum. In the context of boundary-layer theory, this desire has translated to the objective of having as much laminar flow over a surface as possible. In a two-dimensional boundary layer, transition is governed by the formation of Tollmien-Schlichting waves. As stated before, the amplification of these waves depends on many factors. Experience has shown that a "fuller" boundary layer usually results in lower disturbance growth [47]. Let us rewrite (6.83a) for $y \approx 0$ and add the body force term that we have left out before:

$$\mu\frac{\partial^2 u}{\partial y^2} = \rho v_0\frac{\partial u}{\partial y} + \frac{\mathrm{d}p}{\mathrm{d}x} - \frac{\mathrm{d}\mu}{\mathrm{d}T}\frac{\partial T}{\partial y}\frac{\partial u}{\partial y} - f_x \tag{6.124}$$

Note that we have split the partial derivative $\partial/\partial y(\mu\partial u/\partial y)$ and have used $\partial\mu/\partial y = (\partial\mu/\partial T)\cdot(\partial T/\partial y)$. The left-hand side of (6.124) is a measure for the curvature of the boundary layer profile near the wall. Generally speaking, a "fuller" boundary layer corresponds to a convex velocity profile, i.e. a more negative value of $\partial^2 u/\partial y^2$. A negative pressure gradient ($\mathrm{d}p/\mathrm{d}x < 0$) therefore results in lower disturbance growth, while an adverse pressure gradient ($\mathrm{d}p/\mathrm{d}x > 0$) increases disturbance growth. One can also heat or cool the wall. Wall cooling in air ($\partial T/\partial y > 0$, $\partial\mu/\partial T > 0$) stabilizes the boundary layer, while heating it ($\partial T/\partial y < 0$, $\partial\mu/\partial T > 0$) destabilizes the boundary layer. Alternatively, one can apply suction perpendicular to the boundary layer ($v_0 < 0$) in order to reduce the growth of disturbances. This has been successfully demonstrated to postpone transition in the wind tunnel and in flight [7, 44]. Finally, one can apply a body force to the flow in the direction of the velocity vector. This can be done by locally ionizing the air using an electric field. By employing an asymmetric electrode arrangement, a body force can be exerted on the resulting plasma [13]. It has been shown that a periodic body force is effective in attenuating the Tollmien-Schlichting waves [29]. Both suction and plasma control are examples of active laminar flow control (LFC).

In the early 20th century William Orr and Arnold Sommerfield independently derived the linear homogeneous ODE describing the infinitesimal laminar flow instability based on the steady continuity equation (2.113) and the unsteady linear momentum equation (2.126). In contrast to our earlier assumption, Orr and Sommerfield allowed infinitesimal velocity perturbations perpendicular to the flow direction within the boundary layer. They assumed that these perturbations changed harmonically with time and could grow exponentially in time and space depending on the frequency of the wave, the wave propagation speed, the kinematic viscosity, and the shape of the velocity profile. For negligible viscosity, the solution of the Orr-Sommerfield equation showed that only velocity profiles with an inflection point in the velocity profile would amplify the instabilities. Additionally, the second derivative of the velocity with respect to y (distance perpendicular to the surface) needed to be smaller than zero. This led to the mistaken assumption that a favorable pressure gradient could stabilize the boundary layer up to an infinite Reynolds number. Prandtl demonstrated, however, that viscosity can indeed be destabilizing for certain wave numbers at a finite Reynolds number.

A more elaborate discussion of the the stability of laminar boundary layers can be found in the text of White [66]. A selection of the results for boundary layers over smooth flat plates is listed below:

1. The minimum or *critical* Reynolds number for initial instability is $\mathrm{Re}_{x\ \mathrm{crit}} \approx 91{,}000$.
2. The smallest unstable wavelength is $\lambda_{\min} \approx 6\delta$. Thus, unstable Tollmien-Schlichting waves are long compared to boundary layer thickness.
3. Compared to $\mathrm{Re}_{x\ \mathrm{crit}} \approx 91{,}000$, the point of final transition to turbulence is at about $\mathrm{Re}_{x\ \mathrm{tr}} \approx 3 \times 10^6$, or about 30 times further downstream.

In practice, the transition process is influenced by many factors: surface roughness, freestream disturbances, pressure gradients, vibration, sound, etc. Therefore, the exact Reynolds number (or position, for a given fluid and speed) can vary with time in a random way. Placing objects in the boundary layer results in a swift amplification of the instabilities in the boundary layer and hastens the onset of transition. Such trip strips are often used in wind tunnel experiments to fix the point of transition at a fixed percentage of the wing chord. Other sources of instabilities stem from the attachment line of the boundary layer on the leading edge of objects that are placed oblique to the flow (such as the leading edge of a swept wing). In addition, instabilities arising from three-dimensional cross flow (also found on swept wings) hasten the onset of laminar to turbulent transition. This will be further discussed in Chap. 8 when we treat the aerodynamics of swept wings.

In the derivation of the critical Reynolds number a Blasius[6] profile was assumed for the velocity distribution, $u(y)$, in the boundary layer. However, it was shown that the critical Reynolds number can be 90 times higher than this value when the velocity

[6] The Blasius velocity profile satisfies the nonlinear ordinary differential equation that can be derived from the boundary layer equations under specific assumptions, see (6.90a).

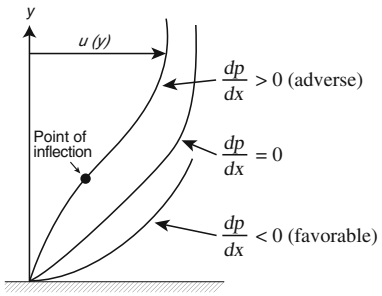

Fig. 6.47 Effect of pressure gradients $\mathrm{d}p/\mathrm{d}x$ on velocity profile, $u(y)$

profile in the boundary layer satisfies the condition: $\partial^2 u/\partial y^2 < 0$. Such velocity profiles are very stable and postpone transition to a much higher Reynolds number. Such a stable velocity profile can be formed when a favorable pressure gradient is present as is shown in Fig. 6.47. The boundary layer profile that is subjected to an adverse pressure gradient shows an inflection point, which means that $\partial^2 u/\partial y^2$ changes sign in this point. In this case the critical Reynolds number (and the transition Reynolds number) is decreased.

The critical Reynolds number can be shown to correlate to the shape factor of the boundary layer at the point where instabilities start to occur. The shape factor can, in turn, be calculated by the velocity distribution in the x-direction outside of the boundary layer (as was shown through Thwaites method on pp. 305–306). In Fig. 6.48 this correlation is experimentally demonstrated through a range of experiments. Both the critical Reynolds number as well as the transition Reynolds number are shown.

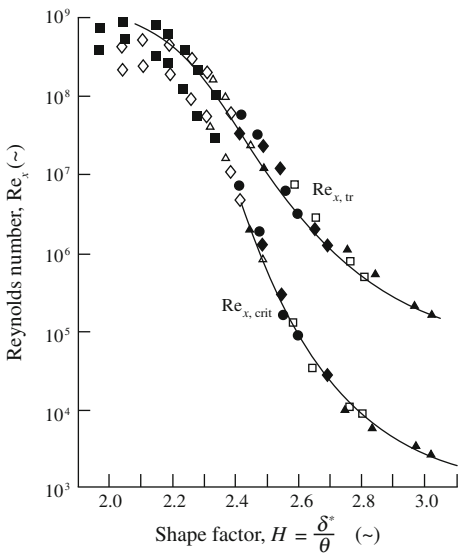

Fig. 6.48 Correlation between shape factor and transition Reynolds number (after Ref. [64])

The curve that is fitted through transition data points corresponds to the following curve-fitted equation [64]:

$$\log_{10}(\mathrm{Re}_{x,\,\mathrm{tr}}) \approx -40.4557 + 64.8066H - 26.7538H^2 + 3.3819H^3 \qquad (6.125)$$

By using Thwaites method for the calculation of the local shape factor and combining that with (6.125), a swift prediction of the transition Reynolds number can be obtained.

Example 6.7 Consider the flow problem of Example 6.3. Use the criterion of (6.125) to calculate where transition is expected to occur.

Solution:

We need to calculate the local Reynolds number at each x-position, Re_x. Subsequently, we need to evaluate whether the following inequality holds:

$$\mathrm{Re}_x < \mathrm{Re}_{x,\,\mathrm{tr}}$$

We employ (6.125) to compute the transition Reynolds number, $\mathrm{Re}_{x,\,\mathrm{tr}}$. We have tabulated these values up to the position where separation is predicted (Table 6.2). We can observe that the inequality holds until $x = 70$ mm. This means that transition takes place between 60 and 70 mm. Note that the boundary layer calculations beyond this point should therefore consider a turbulent boundary layer.

Another popular method to predict boundary layer transition is based on linear stability theory (LST). The e^9 method as pioneered by van Ingen [60] and Smith and Gamberoni [52] assumes that transition occurs when the most unstable Tollmien-Schlichting waves are amplified by a certain factor. Here, $e \approx 2.71828$ is the base of the natural logarithm. The transition amplification factor is usually taken as $e^9 \approx 8{,}100$, although a different value than 9 can be assigned to the exponential depending on the disturbances in the freestream flow [61]. Therefore, the method is currently referred to as the e^N method, where N depends on the turbulence intensity in the free stream. van Ingen [61] uses the following relating between the value of N and the turbulence intensity, Tu:

$$N = 2.13 - 6.18\log_{10}(\mathrm{Tu}) \quad \text{for} \quad 0.1\,\% < \mathrm{Tu} < 2\,\% \qquad (6.126)$$

Note that Tu should be inserted in this equation as a percentage. This equation is based on a variety of experimental data and presents the critical reduced amplification

Table 6.2 Table belonging to Example 6.7

x	mm	0	10	20	30	40	50	60	70	80	90	100	110	120
$\mathrm{Re}_x \times 10^{-6}$	(~)	0.00	0.07	0.13	0.20	0.26	0.32	0.38	0.44	0.49	0.55	0.60	0.66	0.71
$\mathrm{Re}_{x,\,\mathrm{tr}} \times 10^{-6}$	(~)	4.59	3.72	2.91	2.19	1.55	1.02	0.61	0.32	0.14	0.05	0.02	0.01	0.00

factor at the beginning of transition. For turbulence levels below Tu $< 0.1\,\%$ the experimental data shows too much scatter to warrant a simple relation as (6.126). The turbulence intensity (in percentages) is defined as follows:

$$\mathrm{Tu} = 100 \cdot \frac{\mathrm{RMS}(u')}{\bar{u}} \tag{6.127}$$

where $\mathrm{RMS}(u')$ is the root-mean-square of the turbulent velocity perturbations and $\bar{u}$ is the mean velocity as defined in (2.154).

The amplification factor (or the logarithm thereof) can be correlated to integrated amplification rates. For example, Giles and Drela [18] rely on the following computation for the logarithm of the maximum amplification factor (N) [23]:

$$N = \frac{\mathrm{d}N}{\mathrm{dRe}_\theta}(H_k)\left[\mathrm{Re}_\theta - \mathrm{Re}_{\theta_0}(H_k)\right] \tag{6.128}$$

where Re_θ is the momentum-thickness Reynolds number that can be calculated as follows:

$$\mathrm{Re}_\theta = \frac{\rho_e u_e \theta}{\mu_e} \tag{6.129}$$

The following empirical formulas can be employed to calculate $\frac{\mathrm{d}N}{\mathrm{dRe}_\theta}$ and $\mathrm{Re}_{\theta_0}(H_k)$:

$$\frac{\mathrm{d}N}{\mathrm{dRe}_\theta} = 0.01\sqrt{[2.4H_k - 3.7 + 2.5\tanh(1.5H_k - 4.65)]^2 + 0.25} \tag{6.130}$$

$$\log_{10}\mathrm{Re}_{\theta_0} = \left(\frac{1.415}{H_k - 1} - 0.489\right)\tanh\left(\frac{20}{H_k - 1} - 12.9\right) + \frac{3.295}{H_k - 1} + 0.44 \tag{6.131}$$

In the above equations the parameter H_k is the kinematic shape factor, which is calculated using the following empirical relation assuming a constant density across the boundary layer [67]:

$$H_k = \frac{H - 0.290M_e^2}{1 + 0.113M_e^2} \tag{6.132}$$

with M_e being the Mach number at the boundary-layer edge and H being the shape factor from (6.63).

The method described above predicts the onset of transition. The laminar boundary-layer variables can be calculated using (6.59), (6.61), and (6.63). If the outcomes are combined with the properties at the boundary-layer edge (u_e, p_e, T_e), the above equations can be used to calculate the value of N. If N surpasses a predefined threshold (e.g. $N = 9$), the boundary layer transitions from laminar to turbulent.

Example 6.8 Assume we have curved plate of length $c = 1\mathrm{m}$, that supports a pressure distribution according to:

$$C_p = 8\left(\frac{x}{c}\right)\left[\left(\frac{x}{c}\right) - 1\right] + 1$$

The flow over this plate can be assumed incompressible and adiabatic. The freestream velocity of this flow is $V_\infty = 50\,\text{m/s}$ and the plate is at mean sea-level conditions of the international standard atmosphere (i.e. 0 m ISA). Carry out the following assignments:

(a) Use Thwaites' method to calculate the position of laminar separation and the momentum thickness distribution.
(b) For $\text{Tu} = 0.1\,\%$ and $\text{Tu} = 2\,\%$ compute the logarithm of the amplification factor, N, at which transition takes place.
(c) Use the method presented prior to this example to compute the distribution of the logarithm of the amplification factor, N.
(d) For each turbulence level, compute the position of transition point and mark these points in the plot of the reduced amplification factor.

Solution:

(a) We follow Example 6.3 to answer the first question. The most convenient way to do this is to implement all the relevant equations in a spreadsheet program or other computational software such as Matlab. We first convert the pressure distribution to a velocity distribution by employing (6.11):

$$u_e = V_\infty\sqrt{1 - C_p}$$

Subsequently, we take the derivative of u_e with respect to x and we employ (6.101) to compute the distribution of θ and λ up to $\lambda = -0.09$. The resulting separation point is $(x/c)_{\text{sep}} = 0.61$.
(b) We employ (6.126) to compute that for $\text{Tu} = 0.1\,\%$ we have $N \approx 8.3$ and for $\text{Tu} = 2\,\%$ we have $N \approx 0.3$.
(c) We need to solve (6.128). To that purpose, we implement (6.130)–(6.132) into our spreadsheet program. Furthermore, we need the momentum-thickness Reynolds number (6.129), the equation of state (2.72), and the equation for the speed of sound (2.106) to calculate Re_θ, $\frac{\text{d}N}{\text{d}\text{Re}_\theta}$, and Re_{θ_0}. The resulting values are subsequently substituted in (6.128) to compute the distribution of N with x as shown in Fig. 6.49.
(d) The transition points are indicated in the graph with dotted lines. They are $(x/c)_{\text{tr}} = 0.45$ and $(x/c)_{\text{tr}} = 0.54$, respectively.

Let us briefly reflect on the result of Example 6.8. First of all, note that the transition point is ahead of the calculated laminar separation point. The predicted onset of transition will therefore cause a turbulent boundary layer before the boundary layer can separate. The separation point therefore has lost its meaning in this example. Secondly, observe the arrows in Fig. 6.49 indicating the stabilizing region and the destabilizing region. When $N < 0$ the amplification factor is smaller than 1, meaning

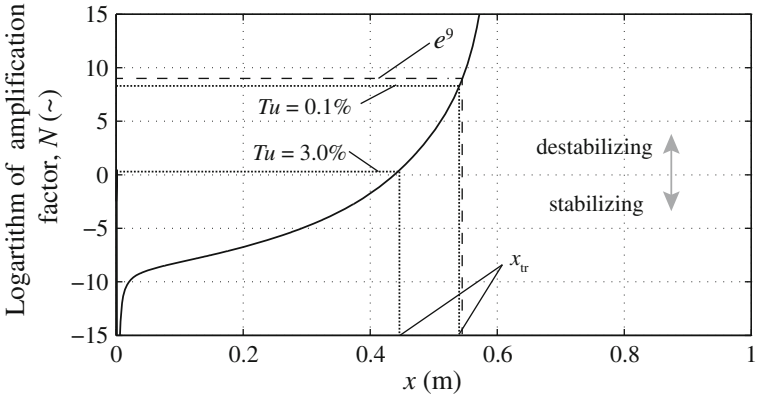

Fig. 6.49 Distribution of logarithm of amplification factor: $N = \ln\left(e^N\right)$ belonging to Example 6.8

that small disturbances in the boundary layer are damped. This corresponds to the pressure distribution, which features a favorable pressure gradient up to $x = 0.5$. We see that when the pressure gradient becomes less negative, the value of N starts to rise quickly. Moreover, when the pressure gradient is positive (beyond $x = 0.5$) a very rapid increase in N can be seen. This implies that initial disturbances in the boundary layer are rapidly amplified under an adverse pressure gradient and therefore cause a quick onset of transition. When we discuss natural-laminar flow airfoils in Sect. 7.3, we will see how an airfoil can be designed in order to sustain laminar flow over a large percentage of the chord.

6.6 Interference Drag

We have seen in the preceding sections that any body of a particular curvature causes the flow over the body to accelerate or to decelerate. In addition we have seen that the supervelocities directly (via friction) and indirectly (via shocks) affect the drag of a body in transonic conditions. If we have two bodies that each have their own drag (e.g. D_1 and D_2) and we would join these bodies together we mostly find that the cumulative drag of these two bodies is larger than the sum of the individual components. If the difference, $\Delta D = D_{1+2} - (D_1 + D_2) > 0$, we speak of *interference drag*. This effect is not only present when two bodies intersect each other but also when two bodies are in each others vicinity. At this point we would like to emphasize that the term 'interference drag' is merely a term that describes the effect on drag when two components intersect. The physical cause for drag can, in turn, be attributed to an increase in pressure drag or an increase in friction drag.

In the classic book of Hoerner [26] various types of interference drag are distinguished. In the context of the present chapter we focus on the interference drag caused by the intersection of two bodies. In practice, at least one of the two bodies is often a lifting body. For example, the intersection of the horizontal tail plane with

the vertical tail can cause interference drag. For the explanation of the concept of interference drag it is not important whether the interfering bodies are designed to generate lift or not.

6.6.1 Interference Drag in Subsonic Conditions

Interference between aircraft components is not limited to high-subsonic aircraft. In fact, there are several examples of low subsonic aircraft where interference is utilized as a benefit. The most notable example is the single slotted flap that is often seen on low-subsonic aircraft such as the propeller-powered Cessna 172 (most successful mass produced light aircraft to date). The small slot that occurs between the flap and the main wing causes a beneficial interference between these two components which allows the aircraft to fly at a lower speed without stalling. This same effect is used on many of the high-lift systems found on contemporary civil transport aircraft. The interference between the individual components of the high-lift system causes the maximum lift coefficient to increase substantially allowing high-subsonic aircraft to take-off and land at relatively short airfields with acceptable take-off and landing speeds.

Even though the interference on components that are generated to produce lift can produce a net benefit to the airplane, on components which are not intended to generate lift they often contribute to increased drag. An illustration of how two bodies in subsonic flow interfere with each other is shown in Fig. 6.50. In this figure we see that when the two streamlined bodies are at a relative large distance from each other, the total drag of the bodies converges to a fixed value. By decreasing the distance the bodies are forming a converging-diverging nozzle with increasing area ratio (the ratio between nozzle exit and nozzle throat area). The flow that flows through the two bodies decelerates beyond the "throat" such that the fluid can expand in the diverging part of the duct. With increasing area ratio the associated pressure gradient with this deceleration becomes larger and larger. At a certain part the adverse pressure gradient becomes so large that the boundary layers separate from the respective bodies, which results in a large increase in pressure drag.

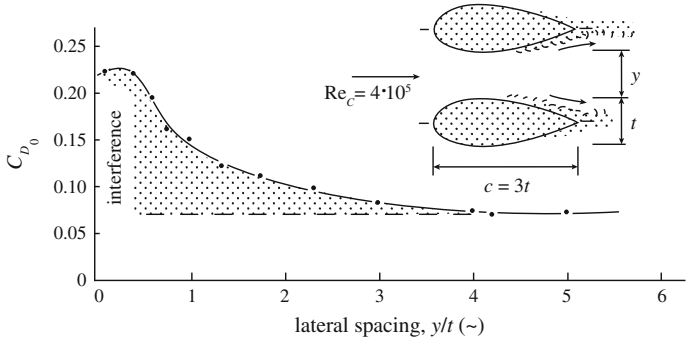

Fig. 6.50 Interference drag between two streamlined bodies (after Ref. [26])

The example above illustrates that two bodies do not need to intersect in order for their mutual interference to cause separation of the boundary layer. This type of interference is mainly based on the flow outside the boundary layer, which is essentially inviscid. However, the magnified acceleration and deceleration of the flow outside the boundary layer also has an effect on the development of the boundary layer, as we have seen in Sect. 6.4.2. Therefore, the local friction coefficient and shape factor of the boundary layer are directly affected by the interference of the two bodies. The increase in adverse pressure gradient for the bodies in Fig. 6.50 increased the shape factor of the boundary layer which made the boundary layer more prone to separation than without the interference of the two bodies.

The effect of interference on the boundary layer is even greater when two bodies intersect. A relevant example is shown in Fig. 6.51a where a streamlined strut intersects with a flat plate. Both the strut and the flat plat generate a boundary layer. The boundary layer on the plate is, generally speaking, a lot thicker than the one on the strut due to the longer distance it has traveled and therefore the time it has had to develop. This results in a relatively small $\mathrm{d}u/\mathrm{d}y|_{\mathrm{wall}}$. At the intersection of the two components the boundary layers join. At the leading edge (stagnation) and over

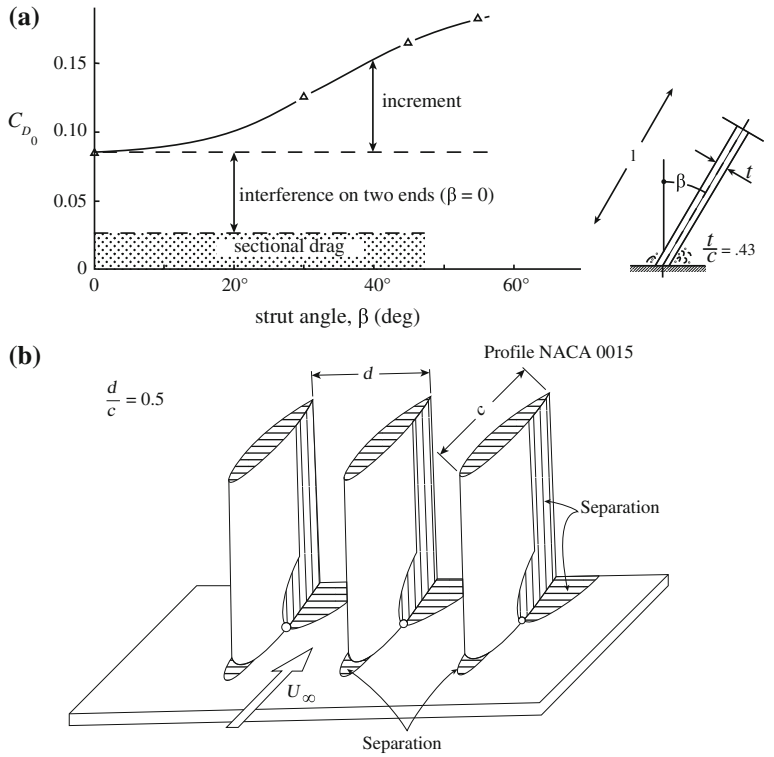

Fig. 6.51 Interference drag due to the intersection of a curved body with a flat wall. **a** Interference between strut and wall (after Ref. [26]). **b** Interference causing separation between cascades and wall (after Ref. [22])

the rear of the airfoil, the boundary layer is invariably retarded, which often leads to separation ($\mathrm{d}u/\mathrm{d}y|_{\text{wall}} < 0$). This is illustrated in Fig. 6.51b where the interference between airfoil cascades and the wall is shown. Near the wall the separated region on the cascades expand more upstream. In addition, a separated region starts to form near the leading edge of the cascades. The separated flow, in turn, causes a wake which results in additional pressure drag. As can be seen in Fig. 6.51a the angle between the strut and the wall is an important factor for the value of the interference drag coefficient. When the angle between the strut and the wall becomes smaller than 90° the interference drag also increases. This is due to increased separation in the narrower one of the two corners.

In order to minimize interference drag between components we need to make sure that the boundary layer remains attached at all times. The unfavorable addition of pressure distributions should be avoided. One way to achieve this is to apply fillets between the two surfaces. This fillet locally reduces the supervelocities at the intersection of the two bodies. Thereby it reduces the magnitude of the adverse pressure gradient, which shifts the point of separation further downstream or prevents the formation of separation all together.

6.6.2 Interference Drag in Transonic Conditions

In transonic flow the characteristics of interference are magnified. If we look back at Fig. 6.11 we can directly see that the region of influence of a body in transonic flow is much larger than in subsonic conditions, giving rise to a stronger interference between the individual components of the airplane. One can imagine two bodies of the aircraft (e.g. horizontal and vertical tail) that intersect at a particular point. Both bodies generate high supervelocities, possibly even supersonic. However, at the intersection there is less physical space for the flow to go and even higher supervelocities are generated resulting in much stronger local shock waves than would be expected if either one of the two bodies would be considered by itself. The stronger shock waves induce an increase in wave drag that is also a form of interference drag [43]. The strong pressure gradient that accompany strong shocks can also result in separation of the boundary layer, as has been discussed in Sect. 6.4.3. The onset of strong shocks and the accompanied wave drag can lead to a decrease in the drag-divergence Mach number, which generally limits the cruise Mach number of an airplane. Minimizing the interference is therefore an important goal in the aerodynamic design of the aircraft.

Interference drag plays a role throughout the entire aircraft where two bodies intersect or are positioned close to each other. Ideally, the velocity distributions on the intersecting bodies should complement each other to minimize the total supervelocity at the intersection. If one body locally displays a negative pressure coefficient, the intersecting body should have a positive pressure coefficient. Often, local area ruling is applied to achieve this. Particular geometric characteristics on aircraft often show how designers have attempted to reduce the transonic interference drag. We shortly present three such examples in this section.

Fig. 6.52 Leading-edge fairing at the wing root of an A340-300 (*photo* A Pingstone)

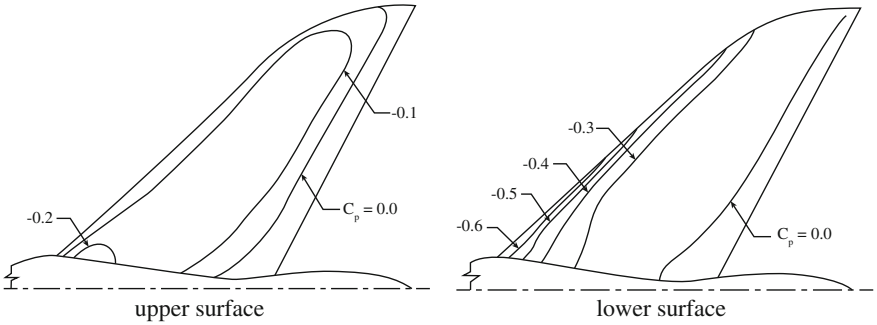

Fig. 6.53 Theoretical isobar patterns on area ruled empennage for $M = 0.80$ and $C_{L_h} = -0.117$

The first example is the wing-body fairing which smoothes the angle between the wing and the fuselage. Without the presence of such a fairing the boundary layer that has developed over the fuselage side is likely to separate. An example of such a fairing is presented in Fig. 6.52.

Another example is the junction between the horizontal and vertical tail plain in a T-tail (see Fig. 6.53). Often, an additional fairing (acorn) is positioned to reduce the added supervelocities that are caused by interference. Adding this body allows the designer to locally change the area distribution of the intersection such that interference is minimized.

The position of the nacelle with respect to the wing is a third example of how interference-drag considerations dominate this geometric feature. The positioning of the nacelle under the wing implies a strong interference between the pressure distribution over the nacelle, pylon, and lower wing surface. An interesting example in this respect is the development of the Convair 990. The specification for this airplane included a very high cruise Mach number ($M_{\text{cruise}} = 0.89$). During early experimentation it surfaced that supersonic flow accompanied by strong shock waves

were present on the inboard sides of the pylons. The *drag rise*[7] of the airplane coincided with the drag rise of the nacelles.

To remedy this problem and postpone the onset of drag divergence to a higher Mach number local area ruling was applied. A representative streamtube was chosen by including (part of) the cross-sectional area of nacelle, pylon and wing. This streamtube is shown in Fig. 6.54a. A target area distribution was defined that had

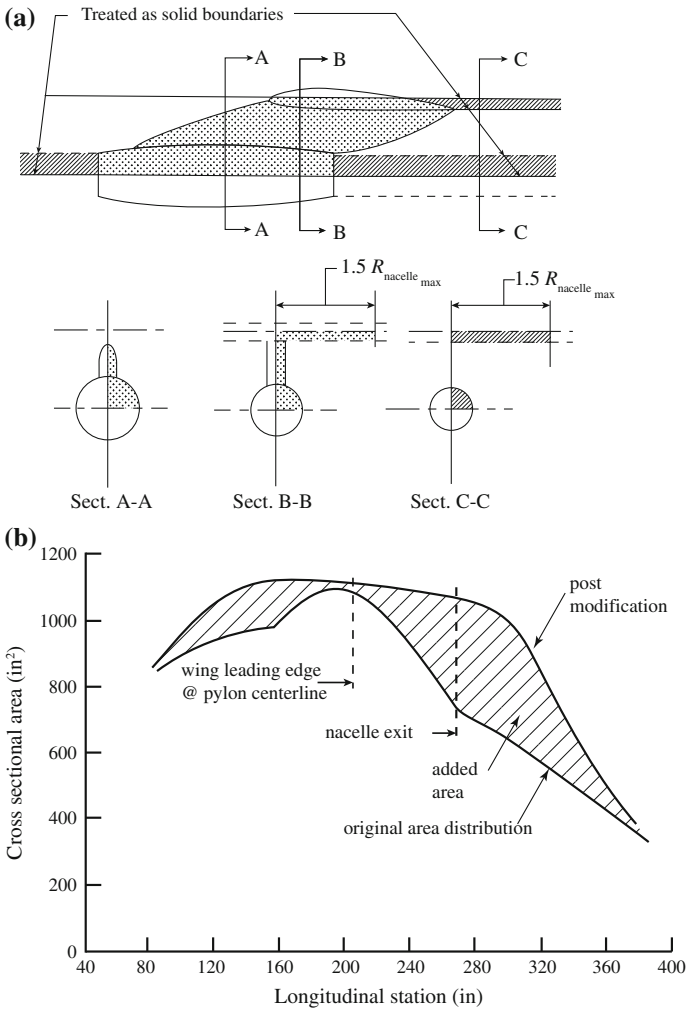

Fig. 6.54 Local area ruling between nacelle, pylon and wing of Convair 990 (after Ref. [31]). **a** Streamtube boundaries. **b** Area distribution prior and post modifications. **c** Drag curve prior and post modification. **d** Proposed modifications to nacelle and pylon

[7] "Drag rise" is a term that describes the exponential increase in drag coefficient with Mach number.

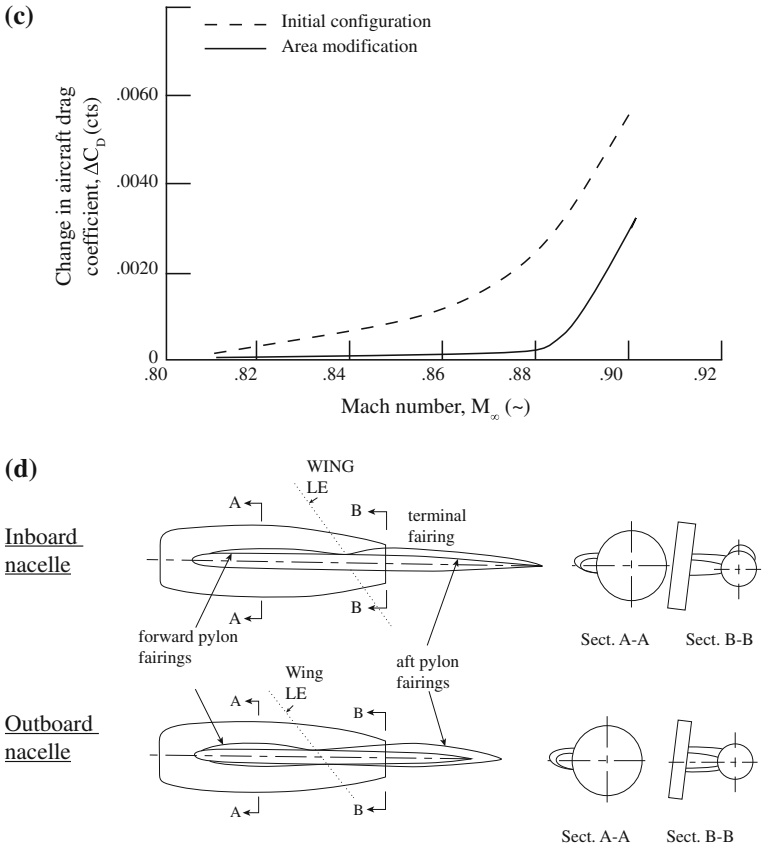

Fig. 6.54 (continued)

to reduce the local supervelocities. Modifications to the cross-sectional area distribution were made by thickening the pylon, modifying the nacelle aft body, and modifying the terminal fairing [32]. This combined effort on all four pylon-nacelle combinations significantly postponed the drag rise onset and resulted in a lower drag coefficient at the design Mach number (Fig. 6.54c). The resulting geometry of the pylons is shown in Fig. 6.54d. Notice the typical area-ruling characteristics of the pylon: close to where the leading edge of the wing intersects the cross-sectional area of the pylon reduces. It is as if the pylon gives the flow additional space to go around the wing.

The examples presented above illustrate the importance of considering the aerodynamic interference between the various components on the airplane. The present discussion is not limited to nonlifting components of the airplane. On the contrary, when integrating bodies that are designed to generate forces the supervelocities are generally larger and the formation of strong shock waves in combination with separation

is even more likely to occur. The integration of winglets to the tip of the wing is an example where the interference of two force-producing bodies is likely to produce interference drag. Creating a fillet with a large radius can prevent the onset of strong shocks in the corner of the two lifting surfaces. For more examples on interference drag created by lifting and non-lifting components the reader is referred to the text of Obert [43].

6.7 Summary

There are several parts of a high-subsonic airplane that do not contribute to the production of lift during the cruise phase of the mission (e.g. fuselage, fin, nacelle). These surfaces *do* provide a significant contribution to the total drag that is produced by the airplane. We have investigated three important sources of drag: friction drag, drag due to separation, and wave drag.

Wave drag that is associated with the formation of shock waves. A simple method has been presented to calculate the wave drag of an arbitrary nonlifting body. This method, which is based on linearized supersonic potential theory, uses an equivalent axis-symmetric body with the same cross-sectional area distribution as the body under investigation (transonic area rule). It has been shown how the cross-sectional area should be distributed along the length of the body in order to minimize the wave drag. Several examples of the application of area ruling have been presented for both civil and military aircraft.

Friction drag is associated with shear forces that are generated in the boundary layer between the outer flow and the airplane surface. It has been shown that the shape of the velocity distribution in the boundary layer has an effect on the local friction coefficient of both a turbulent and laminar boundary layer. In addition, it affects the streamwise position at which the laminar boundary layer transitions to a turbulent boundary layer. A turbulent boundary layer has a higher velocity gradient at the wall and produces more friction drag than a laminar boundary layer. In addition, the turbulent boundary layer is much thicker than the laminar boundary layer which affects the outer pressure distribution through the displacement effect. The shape of the velocity profile in the boundary layer, in turn, is affected by the outer pressure distribution. The shape of the body (which is responsible for the pressure distribution) is therefore of pivotal importance for the total amount of friction drag that is generated. While the turbulent boundary layer is less sensitive to changes in Reynolds number than the laminar boundary layer, it is much more sensitive to changes in Mach number. The presence of surface roughness has an effect on the transition point (shifts forward) as well as on the local value of the friction drag (becomes larger). Additionally, it is shown that the friction coefficient becomes smaller with increasing Reynolds and Mach number. However, for roughened surfaces there exists a cut-off Reynolds number above which the friction coefficient remains constant with Reynolds number.

When a boundary layer is highly loaded by an adverse pressure distribution it tends to separate from the surface. In the aerodynamic design of an aircraft separation of the boundary layer is to be prevented during normal operation. It has been shown that the boundary layer shape factor grows under the influence of an adverse pressure gradient. Furthermore, a simple method has been presented that shows that the onset of separation starts at a shape factor of around 3.0. In the context of nonlifting bodies, separation often occurs relatively far downstream due to a (weak) adverse pressure gradient in combination with a relatively high shape factor. Conversely, in areas where supersonic flow domains are terminated with a shock wave the shape factor can rise quickly and separation can occur at the foot of the shock. Flow visualization is capable of showing shock-boundary layer interaction in transonic speeds. The strength of the shock and the state of the boundary layer (i.e., laminar versus turbulent) dominate the behavior of boundary layer upon its interaction with shocks in transonic flow.

Intimately tied to the formation of shock waves and the separation of the boundary layer is the concept of interference drag. It has been shown that in high-subsonic flow the propagation of disturbances caused by the presence of a body is significantly higher than in low-subsonic conditions. This interference has a magnification effect on the supervelocities over the interfering bodies. This can result in separation of the boundary layer in stagnation areas or areas with large adverse pressure gradients. In addition, strong shocks might form that increase the wave drag and limit the cruise Mach number of the airplane. To reduce interference drag, local area ruling can be applied where the cross-sectional area distribution of the combined bodies is smoothened. In practice, this often means that additional fairings between the joining components are required to reduce the interference effect.

Problems

Introduction

6.1 Consider the flow about the body in the control volume of Fig. 6.1.

(a) Show that the continuity equation (2.109) can be rewritten according to: $\int_{\text{intake}} \rho_1 u_1 \mathrm{d}y = \int_{\text{exhaust}} \rho_2 u_2 \mathrm{d}y$.
(b) Show that (6.7) can be derived from (6.6) and the relation shown under (a).

6.2 Consider the flow about the body in the control volume of Fig. 6.1.

(a) If we assume that the velocity defect behind the wing $(u_1 - u_2)$ is small compared to the free stream velocity, V_∞, show that $D \approx \rho V_\infty \int_D^C (V_\infty - u_2)\,\mathrm{d}y$.
(b) Show that, under the same assumptions, the drag can also be derived from the total-pressure defect in the wake of the wing: $D \approx \int_D^C \left(p_{t_\infty} - p_{t_2}\right) \mathrm{d}y$.
(c) Based on the items above, how would you measure the drag of a body at section CD?

Pressure Distribution Over Nonlifting Bodies

6.3 Consider Euler's equation for conservation of momentum along a streamline, (6.8).

(a) Starting from (6.8) derive Bernoulli's equation.
(b) Derive (6.11) from (3.11).
(c) Derive (6.12) from (6.11) using the assumptions mentioned in the text.

6.4 Using the same approach as in Example 6.1, draw the notional pressure distributions about the following axis-symmetric bodies:

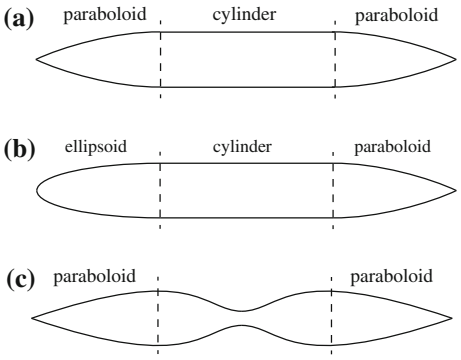

6.5 In the figure below you find a side-view of a British experimental aircraft for radar surveillance (Early Warning), the British Aerospace Nimrod AEW. Sketch the relation of the static pressure coefficient at the lower and upper crown line of the forward fuselage in the plane of symmetry.

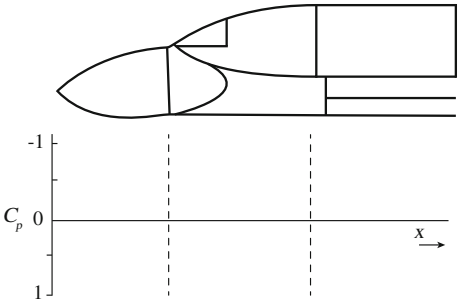

6.6 (a) Derive (6.17) based on the expression for the pressure coefficient and the isentropic relation between total pressure and static pressure.
(b) If $M_\infty = 0.8$ and $C_p = -2$, calculate the local Mach number.
(c) If $M_\infty = 0.8$ and $C_p = -3$, calculate the local Mach number.
(d) Calculate for what value of the C_p the theoretical local Mach number tends to infinity if $M_\infty = 0.8$.

6.7 For the free stream Mach numbers ranging from 0.1 to 0.8, graph the increase in Mach number, ΔM, as a function of pressure coefficient. Use a range of C_p between -2 and 0.

Wave Drag

6.8 Show that (6.22) can be derived from (6.19), (6.21), and (2.106).

6.9 Consider the perturbed momentum equation in integral form (6.26).

(a) Show that, by employing the continuity equation (6.27), this equation can be simplified according to:

$$\boldsymbol{F}_{\text{body}} = -\iint_S \left[p\boldsymbol{n} + \rho V_\infty^2 \boldsymbol{v}\,(\boldsymbol{v}\cdot\boldsymbol{n} + \boldsymbol{i}\cdot\boldsymbol{n}) \right] \mathrm{d}S.$$

(b) Argue that the expression above is identical to (6.28) because we integrate over an enclosed surface, S.

6.10 Consider (6.50) in terms of the Glauert variable θ.

(a) Rewrite (6.50) in terms of x.
(b) If $R(x)$ is the distribution of the radius of the Sears-Haack body, express $R(x)$ in terms of the maximum radius, $R_{\max}$, and x.

6.11 Consider the body described in Example 6.2.

(a) Calculate the volume, $\mathscr{V}$, and maximum radius, $R_{\max}$ corresponding to the aforementioned body.
(b) Calculate the wave drag of a Sears-Haack body with the same length and volume as the aforementioned body.
(c) Calculate the relative decrease in wave drag coefficient (in percentages) that can be attained when modifying this body to the Sears-Haack body with identical volume and length.

6.12 The aft fuselage of the Airbus A320 exhibits a tailored waist at the location of the horizontal tail. In addition, the vertical tail is moved forward relative to the horizontal tail. What are the explanations for their relative positioning?

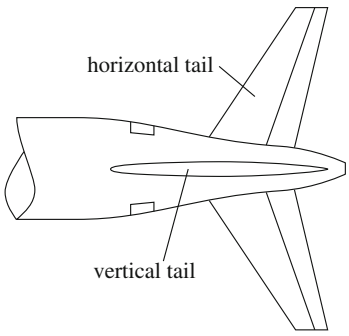

6.13 The figure below reveals the large wing-fuselage fairing of the Airbus A380. This fairing is so large that it received the nickname "the bathtub." Associated with it are a large wetted area and a weight penalty. Carefully explain the reason of existence of a wing-fuselage fairing in general, despite the drawbacks mentioned.

Photo Creative Commons - Simon-sees

6.14 The Convair 990 (see below) was designed to be a jet transport with a cruise Mach number of $M = 0.89$. In 1958 this was quite challenging due to the limited computational resources. Wind tunnel tests on the initial design demonstrated that the drag coefficient was too large to attain the desired cruise Mach number. A somewhat unconventional solution was proposed and eventually adopted in the final design. The solution was to position large bodies near the trailing edge of the wing on the top surface.

(a) Carefully explain how the addition of these bodies can result in a lower drag coefficient at the design Mach number.
(b) Name two disadvantages of these bodies.
(c) Why do modern transport aircraft lack these additional bodies?

Photo NASA

Fundamentals of Boundary-Layer Flow

6.15 Consider Fig. 6.24. If we assume that the freestream velocity value of this flow of water equals 1 m/s and that the streamtube in this figure measures 1 cm.

(a) Calculate the velocity gradients at the three different positions.
(b) Calculate the local value of the wall stress at these three positions.
(c) Calculate the local value of the friction coefficient at these three positions.

6.16 Assume we have a plate with a total friction coefficient of $C_f = 0.0030$ at $M \to 0$. Plot the relation between the friction coefficient and the Mach number for $0 < M \leq 1.4$.

Boundary-Layer Computations

6.17 Consider a plate with chord length of $c = 10\,\text{m}$, which is exposed to a flow with $V_\infty = 100\,\text{m/s}$ at 0 m ISA conditions. Consider the following velocity distribution over the plate at the edge of the boundary layer: $u_e = V_\infty \sqrt{1 + b\left(\frac{x}{c}\right)\left[1 - a\left(\frac{x}{c}\right)\right]}$. For $a = 1$ and $b = 2$, perform the following tasks:

(a) Plot the pressure coefficient, C_p, over the plate.
(b) Calculate the position of separation, $(x/c)_{\text{separation}}$.
(c) Plot the momentum thickness over the plate between $x/c = 0$ and $(x/c)_{\text{separation}}$.
(d) Plot the displacement thickness over the plate between $x/c = 0$ and $(x/c)_{\text{separation}}$.
(e) Plot the shear stress over the plate between $x/c = 0$ and $(x/c)_{\text{separation}}$.

6.18 Repeat Problem 6.17 for the following conditions:

(a) $V_\infty = 100\,\text{m/s}$, $c = 1\,\text{m}$, $a = 1$ and $b = 2$.
(b) $V_\infty = 10\,\text{m/s}$, $c = 10\,\text{m}$, $a = 1$ and $b = 2$.
(c) $V_\infty = 100\,\text{m/s}$, $c = 10\,\text{m}$, $a = 2$ and $b = 1$.

6.19 Derive (6.103) by using the definition of u^+ and the definition of τ_w in (6.54).

6.20 Plot the velocity profile according to the *law of the wall*. On the vertical axis show u^+, ranging between 0 and 25. On the horizontal axis, show y^+, ranging between 1 and 1,000.

6.21 To investigate the effect of the Coles wake paramter on the velocity profile, plot (6.109) for $\Pi = 0, 1, 2.5, 5, 10, 15$. On the vertical axis show u^+, ranging from 0 to 100. On the horizontal axis, show y/δ between 0 and 1.0.

6.22 Show that (6.112) can be derived from (6.109) by substituting $y = \delta$ in (6.109).

6.23 Show that when $k^+ \to \infty$ we can reduce (6.121) to (6.122).

6.24 Assume we have a flat plate with an equivalent sand grain roughness of 0.020 mm. Assume that we have 0 m ISA conditions and a freestream velocity of 100 m/s.

(a) Calculate using (6.123) the friction coefficient (c_f) at $x = 2$ m.
(b) Calculate the wall stress, τ_w.
(c) Calculate the velocity gradient at the wall, $(\partial u/\partial y)_w$.

6.25 Consider the plate and flow conditions of Problem 6.24 and the method of Example 6.6. Imagine we have 5 plates with lengths: 1, 3, 10, 20, and 50 m. Assume that on each plate the turbulent boundary layer starts at $x = 0.10$ m. Calculate

(a) The Reynolds number, Re_l, for each plate
(b) The friction coefficient, C_f, for each plate.
(c) Make a plot of the Reynolds number versus the friction coefficient.

6.26 Consider a flat plate of 10 m long. Assume that we have 0 m ISA conditions, a freestream velocity of 100 m/s, and that the turbulent boundary layer starts at $x = 0.10$ m. We would like to evaluate the effect of various sand grain sizes: $k = 0$, 0.025, 0.050, 0.075, 0.10 mm.

(a) Plot the value of the local friction coefficient, c_f as a function of the position x along the length of the plate for the five roughness heights.
(b) Plot the value of the total friction coefficient, C_f, as a function of the roughness height, k.

Interference Drag

6.27 In the figures below you see pictures of two versions of a British Navy-fighter, the Hawker, later Armstrong-Whitworth "Sea Hawk." The later version, powered by an engine with 5400 lb static thrust at sea level, has a fairing at the junction of the horizontal and vertical tailplane. The earlier version, with a 5000 lb static thrust, lacked this fairing. Explain the (aerodynamic) cause for the presence of the fairing on the later version.

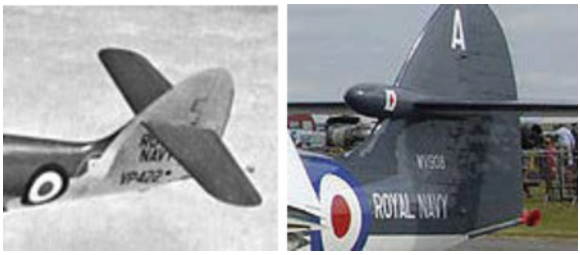

Photos by Hawker Siddley (left) and A. Pingstone (right)

6.28 The picture below shows the Tupolev, Tu-154 in landing configuration. Visible is the pointed cone at the intersection of the horizontal and vertical tailplane. Explain the aerodynamic function of that cone using sketches of pressure distributions.

Photo A. Pingstone

6.29 The Lockheed P-38 Lightning (below) was in many ways innovative. An undesirable characteristic of this aircraft was heavy horizontal tail buffeting at high speed. Initially it was expected that it was classical flutter of the horizontal tail itself and could be cured using mass balances. However, that did not solve the problem at all. Only after a fairing was added at the root of the wing's leading edge, where it meets the fuselage, did the buffet disappear. What can be concluded about the precise cause of this phenomenon?

Photo USAF

References

1. Abernathy, F.H.: Fundamentals of boundary layers. In: Illustrated Experiments in Fluid Mechanics. National Committee for Fluid Mechanics Films. Cambridge (1970)
2. Adams, R.A.: Calculus: A Complete Course, 4th edn. Addison Wesley Longman Ltd., Reading (1999)
3. Anderson, J.: Fundamentals of Aerodynamics, 5th edn. McGraw Hill, New York (2010)
4. Ashley, H., Landahl, M.: Aerodynamics of Wings and Bodies. Addison Wesley, Reading (1965)
5. Babinsky, H., Délery, J.: Transonic shock-wave-boundary-layer interactions. In: Shock-Wave Boundary-Layer Interactions, pp. 87–136. Cambridge University Press, Cambridge (2011)
6. Bauer, A.B., Smith, A.M., Hess, J.L.: Potential flow and boundary layer theory as design tools in aerodynamics. Can. Aeronaut. Space J. **16**(2), 53–69 (1970)
7. Braslow, A.: A History of Suction-Type Laminar-flow Control with Emphasis on Flight Research. NASA, Washington (1999)
8. Chan, Y.: An Experimental Study of the Transonic Equivalence Rule with Lift. Aeronautical report LR-609. National Aeronautical Establishment. National Research Council of Canada, Ottawa (1982)
9. Chan, Y.: An Experimental Study of the Transonic Equivalence Rule with Lift, Part II. Aeronautical report LR-614. National Aeronautical Establishment. National Research Council of Canada, Ottawa (1984)
10. Clauser, F.H.: The turbulent boundary layer. J. Aeronaut. Sci. **21**, 91–108 (1954)
11. Coles, D.E.: The law of the wake in the turbulent boundary layer. J. Fluid Mech. **1**, 191–226 (1956)
12. Coles, D.E., Hirst, E.A.: Computation of turbulent boundary layers. In: Proceedings of the AFOSR-IFP Stanford Conference, vol. 2. Stanford University, Stanford (1968)
13. Corke, T.C., Post, M.L., Orlov, D.M.: SDBD plasma enhanced aerodynamics: concepts, optimization and applications. Prog. Aerosp. Sci. **43**(7–8), 193–217 (2007). doi:10.1016/j.paerosci.2007.06.001
14. da Dosta, A.L.: Application of computational aerodynamics methods to the design and analysis of transport aircraft. In: Proceedings of ICAS, vol. 2, pp. 261–269 (1978)
15. Das, D.K.: A simple theory for calculating turbulent boundary layers under arbitrary pressure gradients. Int. J. Eng. Fluid Mech. **1**, 83–99 (1988)
16. Delery, J.: Shock-wave boundary-layer interactions. In: Babinsky, H., Harvey, J. (eds.) Physical Introduction, Chap. 2, pp. 5–86. Cambridge University Press, New York (2011)
17. Donlan, C.J.: An Assessment of the Airplane Drag Problem at Transonic and Supersonic Speeds. NACA-RM-L54F16, Washington (1954)
18. Drela, M., Giles, M.B.: Viscous-inviscid analysis of transonic and low Reynolds number airfoils. AIAA J. **25**(10), 1347–1355 (1987). doi:10.2514/3.9789
19. Felsch, K. O., Geropp, D., Waltz, A.: Method for turbulent boundary layer prediction. In: Proceedings of the Stanford Conference on the Computation of Turbdent Boundary Layers, pp. 170–176 (1968)
20. Ferri, A.: Elements of Aerodynamics of Supersonic Flows. Macmillan Company, New York (1949)
21. Fick, A.: Ueber diffusion. Annalen der Physik **170**(1), 59–86 (1855)
22. Gersten, K.: AGARD Report 299: Corner interference effects (1959)
23. Gleyzes, C.J., Cousteix, Bonnet, J.L.: Theoretical and experimental study of low Reynolds number transitional separation bubbles. In: Conference on Low Reynolds Number Airfoil Aerodynamics, pp. 137–152 (1985)
24. Goodmanson, L., Gratzer, L.: Recent advances in aerodynamics for transport aircraft. In: 9th Annual Meeting and Technical Display, Annual Meeting. American Institute of Aeronautics and Astronautics (1973). doi:10.2514/6.1973-9
25. Hicks, R.M., Hopkins, E.J.: Effects of Spanwise Variation of Leading-Edge Sweep on the Lift, Drag, and Pitching Moment of a Wing-Body Combination at Mach Numbers from 0.7 to 2.94, NASA TN D-2236, Moffett Field (1964)

26. Hoerner, S.F.: Fluid Dynamic Drag. Hoerner Fluid Dynamics (1965)
27. Johnson, H.A., Rubesin, M.W.: Aerodynamic heating and convective heat transfer—summary of literature survey. Trans. ASME **71**, 447–456 (1949)
28. Kegelman, J.T., Mueller, T.J.: Experimental studies of spontaneous and forced transition on an axisymmetric body. AIAA J. **24**(3), 397–403 (1986)
29. Kotsonis, M., Giepman, R., Hulshoff, S., Veldhuis, L.: Numerical study of the control of Tollmien-Schlichting waves using plasma actuators. AIAA J. **51**(10), 2353–2364 (2013). doi:10.2514/1.J051766
30. Kreyszig, E.: Advanced Engineering Mathematics. Wiley, New York (1988)
31. Kutney, J.T., Piszkin, S.P.: Reduction of drag rise on the Convair 990 airplane. J. Aircr. **1**(1), 8–12 (1964)
32. Kutney Sr, J.: The inside story of the Convair 990 the fastest subsonic airliner in the world. In: Proceedings of AIAA Joint Propulsion Conference and Exhibit, July, pp. 1–18. AIAA-2007-5338 (2007)
33. Kuz'min, A.G.: Boundary-Value Problems for Transonic Flow. Wiley, Chichester (2002)
34. Laufer, J., Vrebalovich, T.: Stability and transition of a supersonic laminar boundary layer on an insulated flat plate. J. Fluid Mech. **9**(2), 257–299 (1960). doi:10.1017/S0022112060001092
35. Lees, L.: The Stability of the Laminar Boundary Layer in a Compressible Fluid. NACA TN 1360. Langley Field, Virginia (1947)
36. Liepmann, H.W.: The interaction between boundary layer and shock waves in transonic flow. J. Aeronaut. Sci. **13**(12), 103–138 (1946)
37. Liepmann, H.W., Roshko, A.: Elements of Gas Dynamics. Wiley, New York (1957)
38. Little Jr., B.H.: Advantages and problems of large subsonic aircraft. In: AGARD-LS-37-High Reynolds Number Subsonic Aerodynamics. AGARD (1970)
39. Lobb, R.K., Winkler, E.M., Persh, J.: Experimental investigation of turbulent boundary layers in hypersonic flow. J. Aeronaut. Sci. **22**(1), 1–9 (1955)
40. MacWilkinson, D.G., Blackerby, W.T., Paterson, J.H.: February correlation of full-scale drag predictions with flight measurements of the C141A aircraft—phase II. Wind Tunnel Test, Analysis, and Prediction Techniques, NASA CR-2333, Marietta (1974)
41. Moulden, T.H.: Fundamentals of Transonic Flow. Wiley, New York (1984)
42. Nikuradse, J.: Stromungsgesetze in rauhen Rohren. Forsch. Arb. Ing.-Wes, p. 631 (1933)
43. Obert, E.: Aerodynamic Design of Transport Aircraft. IOS Press, Delft (2009)
44. Pfenniger, W.: Laminar flow control—laminarization. In: Special Course on Concepts for Drag Reduction, pp. 3.1–3.75. AGARD R-654 (1977)
45. Reynolds, O.: On the experimental investigation of the circumstances which determine whether the motion of water shall be direct or sinuous, and the law of resistance in parallel channels. Philos. Trans. R. Soc. Lond. Ser. A **174**, 935–982 (1883)
46. Rubesin, M.W., Maydew, R.C., Varga, S.A.: An Analytical and Experimental Investigation of the Skin Friction of the Turbulent Boundary Layer on a Flat Plate at Supersonic Speeds. NACA TN 2305. Moffett Field, California (1951)
47. Saric, W.S., Reed, H.L., White, E.B.: Stability and transition of three-dimensional boundary layers. Annu. Rev. Fluid Mech. **35**(1), 413–440 (2003). doi:10.1146/annurev.fluid.35.101101.161045
48. Schlichting, H., Gestern, K.: Boundary Layer Theory, 8th edn. Springer, Berlin (1999)
49. Schlichting, H., Truckenbrot, E.: Aerodynamik des Flugzeuges. Springer, Heidelberg (1960)
50. Shapiro, A.H.: The Dynamics and Thermodynamics of Compressible Fluid Flow. Ronald Press, New York (1953)
51. Shapiro, A.H.: Pressure fields and fluid acceleration. In: Illustrated Experiments in Fluid Mechanics. National Committee for Fluid Mechanics Films. Cambridge (1962)
52. Smith, A., Gamberoni, N.: Transition, Pressure Gradient, and Stability Theory. Douglas Aircraft Company, Rept. ES 26388 (1956)
53. Sommer, S.C., Short, B.J.: Free-Flight Measurements of Turbulent-Boundary-Layer Skin Friction in the Presence of Severe Aerodynamic Heating at Mach Numbers from 2.8 to 7.0. NACA TN 3391, Moffett Field (1955)

54. Spalding, D.B.: A single formula for the law of the wall. J. Appl. Mech. **28**, 455–457 (1961)
55. Tannehill, J.C., Anderson, D.A., Pletcher, R.H.: Computational Fluid Mechanics and Heat Transfer, 2nd edn. Taylor & Francis, Philadelphia (1997)
56. Thwaites, B.: Approximate calculation of the laminar boundary layer. Aeronaut. Q. **1**, 245–280 (1949)
57. Torenbeek, E., Wittenberg, H.: Generalized maximum specific range performance. J. Aircr. **20**(7), 617–622 (1983)
58. Van Driest, E.R.: Turbulent boundary layer in compressible fluids. J. Aeronaut. Sci. **18**(3), 145–160 (1951)
59. Van Driest, E.R.: Investigation of Laminar Boundary Layer in Compressible Fluids Using the Crocco Method. NACA TN 2597, Washington (1952)
60. van Ingen, J.L.: A Suggested Semi-Empirical Method for the Calculation of the Boundary-Layer Transition Region. TU Delft, Report VTH-74, Delft (1956)
61. van Ingen, J.L.: The eN method for transition prediction. Historical review of work at TU Delft. In: 38th Fluid Dynamics Conference and Exhibit, pp. 1–49. Seattle (2008)
62. von Kármán, T.: Uber laminare und turbulent Reibung. Zeitschrift fur Angewandte Mathematik und Mechanik **1**(4), 233–252 (1921)
63. Wallace, L.E.: The Whitcomb area rule: NACA aerodynamics research and innovation. In: Mack, P.E. (ed.) From Engineering Science to Big Science, Chap. 5. National Aeronautics and Space Administration, History Office, Washington (1998)
64. Wazzan, A.R., Gazley Jr. C., Smith, A.: H-Rx method for predicting transition. J. Aircr. **19**(6), 810–812 (1981)
65. Whitcomb, R.T.: A study of the zero-lift drag-rise characteristics of wing-body combinations near the speed of sound. NACA TR 1273 (1956)
66. White, F.M.: The stability of laminar flows. In: Viscous Fluid Flow, 2 edn. New York (1991)
67. Whitfield, D.: Integral Solution of Compressible Turbulent Boundary Layers Using Improved Velocity Profiles, Arnold Engineering Development Center AEDC-TR-78-42. Arnold Air Force Station, Tennessee (1978)
68. Whitford, R.: Chapter 3: fuselage design. In: Design for Air Combat, pp. 148–160. Jane's, London (1987)
69. Wickens, R.H.: Aerodynamic design of low-drag fuselages. Can. Aeronaut. Space J. **36**(4), 189–201 (1990)